Universität Hamburg

DER FORSCHUNG | DER LEHRE | DER BILDUNG

Calculation of optical and vibrational properties of semiconductor nanostructures

Dissertation

with the aim of achieving a doctoral degree

at the Faculty of Mathematics, Informatics and Natural Sciences

Department of Physics

University of Hamburg

Submitted by

Surender Kumar

August 2024

Gutachter/innen der Dissertation:	Prof. Dr. Gabriel Bester Prof. Dr. Carmen Herrmann
Zusammensetzung der Prüfungskommission:	Prof. Dr. Gabriel Bester Prof. Dr. Dorota Koziej Prof. Dr. Alf Mews Prof. Dr. Michael A. Rübhausen Dr. Marta Elena Prada Vazquez
Vorsitzende/r der Prüfungskommission:	Prof. Dr. Dorota Koziej
Datum der Disputation:	15.10.2024
Vorsitzender des Fach-Promotionsausschusses PHYSIK:	Prof. Dr. Markus Drescher
Leiter des Fachbereichs PHYSIK:	Prof. Dr. Wolfgang J. Parak
Dekan der Fakultät MIN:	Prof. Dr.-Ing. Norbert Ritter

Contents

List of Publications

1. P. García-Risueño, P. Han, **S. Kumar**, and G. Bester; "Anticrossing Situations and its Application to Zero-point Motion Effects in Diamondoid"; *Phys. Rev. B* 2023, 108, 125403, DOI: 10.1103/PhysRevB.108.125403

2. T. Steenbock, T. Dittmann, **S. Kumar**, and G. Bester; "Ligand-Induced Symmetry Breaking as the Origin of Multiexponential Photoluminescence Decay in CdSe Quantum Dots"; *J. Phys. Chem. Lett.* 2023, 14, 39, 8859–8866, DOI:10.1021/acs.jpclett.3c02056

3. **S. Kumar**, H. Bui, and G. Bester; "Empirical Band-Gap Correction for LDA-Derived Atomic Effective Pseudopotentials"; *Com. Cond. Mat.* 2024, 40, e00917, DOI:10.1016/j.cocom.2024.e00917

4. **S. Kumar**, T. Steenbock and G. Bester; "Origin of the High-frequency Shoulder in Raman Spectra of CdSe quantum dots"; *J. Phys. Chem. Lett.* 2024, 15, 10392–10398 (2024), DOI:10.1021/acs.jpclett.4c02335

5. L. Klemeyer, T. L. R. Gröne, C. de A. Zito, O. Vasylieva, M. G. Akcaalan, S. Y. Harouna-Mayer, F. Caddeo, T. Steenbock, S. A. Hussak, J. K. Kesavan, A. C. Dippel, X. Sun, A. Köppen, V. A. Saveleva, **S. Kumar**, G. Bester, P. Glatzel, and D. Koziej; "Combining high X-ray energy photon-in photon-out spectroscopies and X-ray scattering to experimentally assess the emergence of electronic- and atomic structure of ZnS nanorods"; ChemRxiv 2024. (Under Review), Preprint DOI: 10.26434/chemrxiv-2024-qflhf

List of Figures

List of Tables

Acronyms

AEP atomic effective pseudopotential.

CBM conduction band minimum.

CI configuration interaction.

DFT density-functional theory.

EPM empirical pseudopotential method.

FS fine structure.

HOMO highest occupied molecular orbital.

IPR inverse participation ratio.

LDA local density approximation.

LSDA local spin density approximation.

LUMO lowest unoccupied molecular orbital.

PL photoluminescence.

QD quantum dot.

QDs quantum dots.

QP quasiparticle.

SP single-particle.

VBM valence band maximum.

WZ wurtzite.

ZB zincblende.

Abstract

Semiconductor nanostructures have revolutionized semiconductor physics, driving fundamental discoveries and significant advancements in optoelectronic applications. In recent years, colloidal nanostructures have become a research hotspot due to the remarkable control and reproducibility achieved in their synthesis and manipulation. These fascinating structures can be engineered with sizes ranging from just a few atoms in the sub-2 nanometer (nm) regime to thousands of atoms extending across tens of nm. In this size domain, quantum confinement and dielectric confinement effects play a critical role. These effects cause significant deviations in the electronic, optical, and vibrational properties compared to the bulk materials. The highly tunable electronic and optical properties of these structures depend on several factors including size and shape, different compositions, and surface chemistry. This combination of tunable properties leads to exciting research and commercial applications in various fields, including bio-imaging, solar cells, LEDs, diode lasers, and transistors.

Understanding the electronic and vibrational properties of colloidal nanostructures is essential, yet achieving a theoretical framework that consistently aligns with experimental observations remains challenging. The choice of theoretical methods depends on the desired accuracy and computational constraints. Highly accurate *ab initio* methods are ideal for small structures containing up to a few hundred atoms but become computationally prohibitive for larger systems. Semi-empirical methods strike a balance between accuracy and efficiency, making them suitable for structures with several thousand atoms. Fully empirical methods, while less accurate, are computationally efficient and can handle very large structures with millions of atoms. In this work, we strategically utilize *ab initio*, semi-empirical, and empirical methods to calculate the electronic, optical, and vibrational properties of various nanostructured materials.

Chapter 1 lays the groundwork by providing a general overview of the physical properties of semiconductor nanostructures and the motivation of the work.

Chapter 2 lays the foundation for the calculations and methodologies employed

throughout this work. It establishes the fundamental theoretical principles that serve as the basis for the specific theories and results presented in subsequent chapters. This chapter discusses the complexities associated with many-body calculations and explores various underlying approximations used to model materials at the atomic level. A cornerstone of this theoretical framework is the elegant formulation of density functional theory (DFT). Chapter 2 provides a detailed explanation of DFT principles, followed by a discussion of the configuration interaction method.

Chapter 3 focuses on a topic of significant scientific debate: the origin of the high-frequency shoulder (HFS) observed above the longitudinal optical (LO) peak around 230 cm^{-1} in the Raman spectra of cadmium selenide (CdSe) quantum dots (QDs). We use state-of-the-art *ab initio* DFT applied to small CdSe QDs, considering variations in size, the presence of surface defects, different surface terminations, and core/shell structures. We demonstrate that an intense Raman signal appears around 230 cm^{-1} in Se-defective structures, corresponding to the stretching vibration of a twofold-coordinated defective Se atom. We interpret this signal as the origin of the HFS. As this signal is absent in fully passivated and defect-free (magic-size cluster) structures, it can serve as a fingerprint to distinguish between defective and non-defective structures.

Chapter 4 investigates the influence of alloying on the excitonic fine structure (FS) of the QDs and dot-in-rod nanostructures. We investigate how the excitonic FS evolves in different size $Zn_{1-x}Cd_xSe$ alloyed dots with varying concentration x and $Zn_{1-x}Cd_xSe$ dot in CdS rod. We use fully atomistic empirical pseudopotential method in combination with the configuration interaction approach. We find that lattice mismatch in alloyed QDs induces strain, leading to crystal field splitting among SP levels compared to pure QDs. These splittings translate into distinct excitonic fine structures in alloyed QDs, compared to pure ones, indicating inherently multi-exponential photoluminescence decay. The FS analysis of alloyed dot-in-rod structures further reveals that low-temperature PL decay will involve multiple excitonic levels, consistent with the multi-exponential PL decay observed experimentally.

Chapter 5 focuses on the description of the atomic effective pseudopotential (AEP) method, a DFT-based approach for performing electronic structure calculations on large systems with up to fifty thousand atoms. As the AEPs are directly obtained from DFT using the local density approximation (LDA) for exchange-correlation functional, the typical error from LDA, such as underestimated band gaps and effective masses, are inherited by the AEPs. Therefore, an empirical correction of the non-local parts of the

pseudopotential is introduced to achieve correct band gaps and effective masses within the AEPs framework. The effectiveness of this correction is rigorously validated by applying it to both bulk and QDs of varying diameters in various binary semiconductor materials. We compare optical band gaps, intraband splitting, Coulomb integrals, and excitonic FS of QDs with different diameters with the available experimental and theoretical results. Moreover, we provide an example with wurtzite ZnS QDs to show how this correction can be used to determine nanocrystal sizes with reasonable accuracy, given that electronic, quasiparticle, or optical gaps are experimentally measured.

Chapter 6 discusses an extension of the AEP method tailored to handle impurities and defects in semiconductor materials. This extension enables the calculation of the electronic structure of dopant impurities and defects embedded within the materials. To illustrate its practical utility, the electronic structure of Mn as an impurity in wide-gap ZnS is presented. Preliminary results emphasize a comparison between the derived defect AEPs and full *ab initio* calculations, affirming the accuracy of our AEP approach for defect systems. Moreover, we demonstrate the application of our correction scheme to get accurate Mn impurity energy levels in ZnS. By using these gap-corrected results, we lay the groundwork for future calculations involving the many-body multiplets of Mn in ZnS. This will include a combination of the screened CI method, adept at handling open-shell systems, with the derived impurity/defect AEPs.

Finally, in Chapter 7 the results are summarized, and an outlook for future work is presented.

Zusammenfassung

Halbleiter-Nanostrukturen haben die Halbleiterphysik revolutioniert und zu grundlegenden Entdeckungen und bedeutenden Fortschritten bei optoelektronischen Anwendungen geführt. In den letzten Jahren sind kolloidale Nanostrukturen aufgrund der bemerkenswerten Kontrolle und Reproduzierbarkeit, die bei ihrer Synthese und Manipulation erreicht werden, zu einem Hotspot der Forschung geworden. Diese faszinierenden Strukturen können in Größenordnungen von wenigen Atomen im Sub-2-Nanometerbereich (nm) bis hin zu Tausenden von Atomen mit einer Ausdehnung von mehreren zehn nm hergestellt werden. In diesem Größenbereich spielen die Effekte des Quanteneinschlusses und des dielektrischen Einschlusses eine entscheidende Rolle. Diese Effekte führen zu erheblichen Abweichungen bei den elektronischen, optischen und Schwingungseigenschaften im Vergleich zu Massenmaterialien. Die hochgradig abstimmbaren elektronischen und optischen Eigenschaften dieser Strukturen hängen von mehreren Faktoren ab, darunter Größe und Form, unterschiedliche Zusammensetzungen und Oberflächenchemie. Diese Kombination von abstimmbaren Eigenschaften führt zu spannenden Forschungs- und kommerziellen Anwendungen in verschiedenen Bereichen, darunter Bio-Imaging, Solarzellen, LEDs, Diodenlaser und Transistoren.

Das Verständnis der elektronischen und schwingungstechnischen Eigenschaften kolloidaler Nanostrukturen ist von entscheidender Bedeutung, doch ist es nach wie vor eine Herausforderung, einen theoretischen Rahmen zu schaffen, der mit experimentellen Beobachtungen übereinstimmt. Die Wahl der theoretischen Methoden hängt von der gewünschten Genauigkeit und den Berechnungsbeschränkungen ab. Hochpräzise *ab initio*-Methoden sind ideal für kleine Strukturen mit bis zu einigen hundert Atomen, werden aber für größere Systeme rechnerisch unerschwinglich. Semi-empirische Methoden schaffen ein Gleichgewicht zwischen Genauigkeit und Effizienz und eignen sich daher für Strukturen mit mehreren tausend Atomen. Vollständig empirische Methoden sind zwar weniger genau, dafür aber rechnerisch effizient und eignen sich für sehr große Strukturen mit Millionen von Atomen. In dieser Arbeit werden *ab initio*, semi-

empirische und empirische Methoden strategisch eingesetzt, um die elektronischen, optischen und Schwingungseigenschaften verschiedener nanostrukturierter Materialien zu berechnen.

Kapitel 1 verschafft einen allgemeinen Überblick über die physikalischen Eigenschaften von Halbleiter-Nanostrukturen sowie über die Motivation der Arbeit.

Kapitel 2 legt den Grundstein für die in dieser Arbeit verwendeten Berechnungen und Methoden. Es legt die grundlegenden theoretischen Prinzipien fest, die als Basis für die spezifischen Theorien und Ergebnisse dienen, die in den nachfolgenden Kapiteln vorgestellt werden. In diesem Kapitel werden die Komplexität von Vielkörperberechnungen erörtert und verschiedene zugrundeliegende Näherungen untersucht, die zur Modellierung von Materialien auf atomarer Ebene verwendet werden. Ein Eckpfeiler dieses theoretischen Rahmens ist die elegante Formulierung der Dichtefunktionaltheorie (DFT). Kapitel 2 bietet eine detaillierte Erklärung der DFT-Prinzipien, gefolgt von einer Diskussion der Configuration Interaction methode.

Kapitel 3 konzentriert sich auf ein Thema, das in der Wissenschaft viel diskutiert wird: den Ursprung der Hochfrequenzschulter (HFS), die oberhalb des longitudinalen optischen (LO) Peaks um 230 cm^{-1} in den Raman-Spektren von Cadmiumselenid (CdSe) Quantenpunkte (QDs) beobachtet wird. Wir verwenden die modernste DFT, die auf kleine CdSe-QDs angewandt wird, und berücksichtigen dabei Variationen in der Größe, das Vorhandensein von Oberflächendefekten, verschiedene Oberflächenabschlüsse und Kern-/Schalenstrukturen. Wir zeigen, dass ein intensives Raman-Signal um 230 cm^{-1} in Se-defekten Strukturen erscheint, das der Streckschwingung eines zweifach koordinierten defekten Se-Atoms entspricht. Wir interpretieren dieses Signal als den Ursprung der HFS. Da dieses Signal in vollständig passivierten und defektfreien (magic-size cluster) Strukturen nicht vorhanden ist, kann es als Fingerabdruck zur Unterscheidung zwischen defekten und nicht-defekten Strukturen dienen.

Kapitel 4 untersucht den Einfluss der Legierung auf die exzitonische Feinstruktur (FS) der QDs und Dot-in-rod Nanostrukturen. Wir untersuchen, wie sich die exzitonische FS in unterschiedlich großen $Zn_{1-x}Cd_xSe$-legierten dots mit variierender Konzentration x und $Zn_{1-x}Cd_xSe$-dots in CdS-rod entwickelt. Wir verwenden die vollständig atomistische empirische Pseudopotentialmethode in Kombination mit dem Configuration Interaction methode. Wir stellen fest, dass die Gitterfehlanpassung in legiertem QDs eine Dehnung induziert, die im Vergleich zu reinem QDs zu einer Aufspaltung des Kristallfelds zwischen den SP-Niveaus führt. Diese Aufspaltungen führen zu unter-

schiedlichen exzitonischen Feinstrukturen in legierte QDs im Vergleich zu reine QDs, was auf einen inhärent multi-exponentiellen Photolumineszenzabfall hindeutet. Die FS-Analyse von legierten Dot in-rod Strukturen zeigt außerdem, dass der PL-Zerfall bei niedrigen Temperaturen mehrere Exzitonenniveaus umfasst, was mit dem experimentell beobachteten mehrexponentiellen PL-Zerfall übereinstimmt.

Kapitel 5 konzentriert sich auf die Beschreibung der AEP-Methode, einem DFT-basierten Ansatz zur Durchführung von Berechnungen der elektronischen Struktur großer Systeme mit bis zu fünfzigtausend Atomen. Da die AEPs direkt aus der DFT-Methode unter Verwendung die Lokale Dichtenäherung (LDA) Austausch-Korrelations-funktionals gewonnen werden, werden die typischen Fehler der LDA-Methode, wie z. B. unterschätzte Bandlücken und effektive Massen, auf die AEPs übertragen. Daher wird eine empirische Korrektur der nichtlokalen Teile des Pseudopotentials eingeführt, um korrekte Bandlücken und effektive Massen im Rahmen der AEPs zu erhalten. Die Wirksamkeit dieser Korrektur wird rigoros validiert, indem sie sowohl auf Bulk- als auch auf QDs mit unterschiedlichen Durchmessern in verschiedenen binären Halbleitermaterialien angewendet wird. Wir vergleichen optische Bandlücken, Intraband-Aufspaltung, Coulomb-Integrale und exzitonische FS von QDs mit verschiedenen Durchmessern mit den verfügbaren experimentellen und theoretischen Ergebnissen. Darüber hinaus zeigen wir anhand eines Beispiels mit wurtzitischem ZnS QDs, wie diese Korrektur verwendet werden kann, um Nanokristallgrößen mit angemessener Genauigkeit zu bestimmen, vorausgesetzt, dass elektronische, Quasiteilchen- oder optische Lücken experimentell gemessen werden.

In Kapitel 6 wird eine Erweiterung der AEP-Methode erörtert, die auf die Behandlung von Verunreinigungen und Defekten in Halbleitermaterialien zugeschnitten ist. Diese Erweiterung ermöglicht die Berechnung der elektronischen Struktur von Dotierungsverunreinigungen und Defekten, die in den Materialien eingebettet sind. Zur Veranschaulichung des praktischen Nutzens wird die elektronische Struktur von Mn als Verunreinigung in ZnS mit großer Bandlücke vorgestellt. Vorläufige Ergebnisse unterstreichen einen Vergleich zwischen den abgeleiteten Defekt-AEP und vollständigen *ab initio*-Berechnungen, was die Genauigkeit unseres AEP-Ansatzes für Defektsysteme bestätigt. Darüber hinaus demonstrieren wir die Anwendung unseres Korrekturschemas, um genaue Mn-Verunreinigungsenergieniveaus in ZnS zu erhalten. Mit diesen Bandlückenkorrigierten Ergebnissen legen wir den Grundstein für zukünftige Berechnungen der Vielteilchen-Multipletts von Mn in ZnS. Diese werden eine Kom-

bination der gerasterten CI-Methode, die sich für die Behandlung von Systemen mit offener Schale eignet, mit den abgeleiteten AEPs für Verunreinigungen/Defekte beinhalten.

Abschließend werden in Kapitel 7 die Ergebnisse zusammengefasst und ein Ausblick auf zukünftige Arbeiten gegeben.

Chapter 1

Introduction

Semiconductor nanostructures are a fascinating class of materials with unique properties driven by their size and dimensionality. These structures, typically with band gaps ranging from 1 to 4 electron volts (eV), display confinement effects that significantly impact their electronic behavior. When one or more dimensions are confined to a size smaller than the exciton Bohr radius, the confinement forces charge carriers (electrons and holes) into a smaller space, increasing their kinetic energy. This effect, overcoming the reduction in potential energy, leads to the formation of discrete electronic states [1, 2]. As a consequence, the properties of these nanostructures become highly dependent on their size and geometry, offering a playground for tailoring their functionalities. Fig. 1.1 illustrates different types of semiconductor nanostructures with

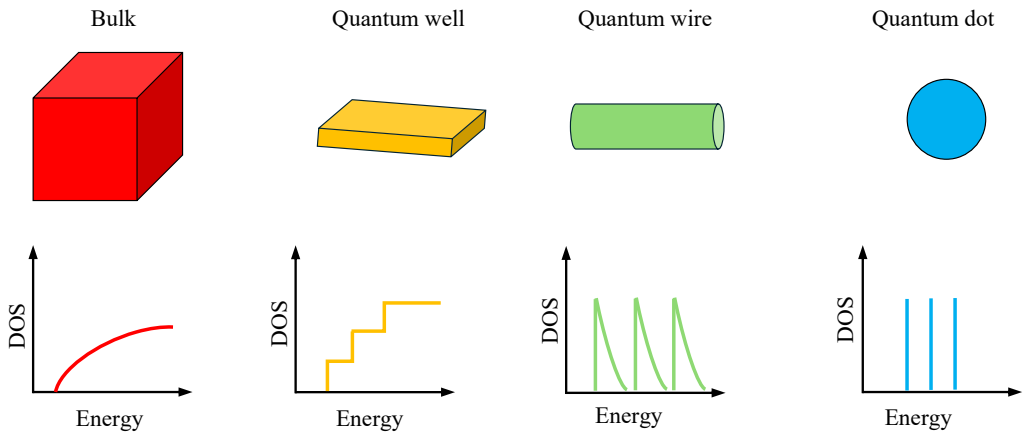

Figure 1.1: Schematic illustration of the density of electronic states (DOS) of a bulk semiconductor, 2D quantum well [3], 1D quantum wire [4], and 0D QD [5, 6].

varying dimensionality. Each type of nanostructure has very distinct characteristics. For example, quantum dots (QDs), with all three dimensions confined, are ideal for applications like single-photon emitters in quantum computing [7, 8] and QD-based solar cells [6]. Conversely, quantum wires, confined in two dimensions, show promise for advancements in thermoelectrics [9] and nanoscale lasers [10]. Quantum wells, with one-dimensional confinement, are widely used in optoelectronic devices like lasers and LEDs [11, 12]. Beyond these traditional structures, recent advancements have led to the development of ultra-thin 2D nanocrystals, such as nanoplatelets (NPLs), with exceptional properties for applications like laser diodes [13, 14, 15, 16].

While advances in synthesis have yielded stable colloidal nanostructures with narrow size distributions and intense fluorescence across the visible and infrared ranges, opening doors for diverse applications [17, 18, 19, 6], the focus extends beyond mere shape and size control. Modern synthesis methods allow for precise tailoring of surface composition [20, 21], alloying [22], and core/shell (CS) structures [23, 24], offering exquisite control over electronic, vibrational, and optical properties. For instance, ligands attached to the surface of QDs play a crucial role in influencing their photoluminescence (PL) decay and vibrational dynamics [20, 21]. While surface defects can catalyze broad-spectrum emission for applications like white LEDs [25], they aren't always desirable, often impeding optimal PL quantum yield. Ideal for applications requiring both stable and high quantum yield, core/shell nanostructures deliver improved performance compared to pure nanostructures [26]. Similarly, alloyed nanostructures are synthesized with interesting properties like wide absorption spectrum (visible to near-infrared) [27], large stokes shift [28], improved photostability [29]. Another fascinating way to exploit nanostructures is purposeful doping or impurity incorporation within nanostructures. These impurities/defects introduce mid-band gap states which have applications in realms like quantum information processing [30].

A critical challenge, yet also an exciting opportunity, lies in understanding and manipulating the underlying physics of the nanostructures. Here, computational methods at various levels of theory become invaluable tools. They allow us to decipher how factors like size, shape, surface composition, and internal structure influence the underlying physics, ultimately dictating the diverse properties of the materials. By simulating nanostructure behavior at the atomic level using a range of theoretical approaches, we can bridge the gap between theory and experiment. This multifaceted approach not only allows us to connect with experimental observations but also allows us to pre-

dict properties that can be targeted in future experiments. However, the choice of the theoretical method depends on its accuracy and the underlying material properties. Fully *ab initio* methods such as density-functional theory (DFT) are highly accurate but are limited due to computational demand for larger structures with thousands of atoms. On the other hand, methods based on empirical pseudopotentials excel in handling larger systems due to their efficiency, but their focus lies primarily on the electronic structure of the system. In this thesis, we utilize a multi-method approach to comprehensively explore the different vibrational and optical properties of various nanostructured materials.

1.1 Motivation

Cadmium selenide (CdSe) QDs from sub-2 nanometers (nm) to tens of nm [31, 32, 33, 21, 34, 35, 36, 37, 38] have been extensively explored due to their size tunable optical properties. These optical properties are strongly influenced by vibrational properties which lead to the appearance of rich phonon sidebands [39, 40, 41] and eventually play a role in shaping the recombination dynamics [42, 43]. Over the years, Raman spectroscopy has been effectively used to probe these vibrational properties [44, 45, 46, 47, 48, 49, 50, 51, 5, 52, 53, 44, 54]. For larger QDs (both core and core/shell), distinct longitudinal optical (LO) and surface-optical (SO) peaks have been observed in the Raman spectra. In addition to the well-established LO and SO peaks, Raman spectra of CdSe QDs often show a high-frequency shoulder (HFS) centered around 230 cm^{-1} above the LO region [46, 44, 51, 53, 45, 55]. The origin of this HFS remains debated, with hypotheses including amorphous surface selenium [45], surface bond reconstruction [45], and coupled optical-acoustic modes [45]. The disappearance of the HFS upon cadmium sulfide (CdS) shell deposition [51, 46, 53] suggests a surface-related origin, yet its precise nature is not fully understood. We investigate the origin of the HFS using state of art *ab initio* DFT-based calculations. We calculate the Raman intensity of realistic ligand-covered QDs with an emphasis on twofold coordinated Se-defect sites, that have been shown to play an important role in small CdSe QDs [56, 57, 58]. Prior *ab initio* Raman studies focused on defect-free structures [52, 59, 60] leaving the importance of defects mainly unexplored from a theoretical standpoint. The underlying theoretical methods and detailed results are presented in Chapter 3.

Another fascinating aspect of semiconductor nanostructures lies in their ability to

form bound electron-hole pairs called excitons upon interaction with the light of energy larger than their band gap. These excitons, classified as quasiparticle (QP), show properties distinct from their individual free electron and hole counterparts. They play a central role in governing the rich optical properties observed in semiconductor nanostructured materials. The fine structure (FS) of the exciton controls the carrier dynamics within the nanostructures [61, 62, 63, 20]. Excitonic FS is a consequence of atomistic effects and the exchange interaction among the carriers (electron and hole) due to their spins. Due to its atomistic nature, excitonic FS is strongly dependent on the crystal and wavefunction symmetries. Therefore, modification of the potential (or the wavefunctions) due to lattice mismatch induced strain and relative band offsets in alloys and core/shell morphology [64, 23, 24, 22, 65, 66] is expected to impact excitonic FS. However, the extent to which alloying and core/shell morphologies affect excitonic FS still lacks a proper understanding which we studied here. In general, calculating the FS is not straightforward, as it requires a proper treatment of the spin-orbit (SO) interaction, the crystal structure, and the electron-hole exchange interaction. Using an empirical pseudopotential-based atomistic approach, we calculate the excitonic FS of varying size $Zn_{1-x}Cd_xSe$ (x is concentration) alloyed dots, and these alloy dots in the shell of cadmium sulfide (CdS) rod on top. The theoretical framework and corresponding results for the calculations are detailed in Chapter 4.

Recently derived atomic effective pseudopotentials (AEPs) allow atomistic calculations of semiconductor nanostructures with scalability up to fifty thousand atoms [67, 68] which is above the practical limit of DFT. AEPs provide electronic structure calculations that are comparable in accuracy to DFT. This approach now extends to impurity/defect calculations in binary materials by creating impurity/defect AEPs. These derived AEPs enable the use of larger supercells for defect simulations, overcoming limitations of DFT for such systems [69, 70]. Notably, defect AEPs can be generated for both spin-unpolarized and spin-polarized systems. The AEPs (defect AEPs) approach, however, inherits the underestimation of the SP band gap and effective masses of the LDA used in their generation. This underestimation of the SP band gap and effective masses leads to discrepancies with experimental results obtained from spectroscopic techniques, such as QP and optical gaps, and different transition energies. For applications where these properties are crucial, a simple yet effective empirical correction method is necessary within the AEP framework to improve the quantitative accuracy of band gaps and effective masses. In this work, we propose a simple approach to achieve

the correct band gap and effective masses with the AEPs framework. Our approach involves modifications to the non-local part of the pseudopotential. By incorporating this correction scheme, we can achieve improved accuracy in the calculation of QP energies, optical band gaps, and the FS of excitons in nanostructures. The details of the correction scheme are presented in Chapter 5. To validate the effectiveness of our approach, we apply it to various binary bulk and QD structures of varying sizes. We demonstrate the accuracy of the correction through direct comparisons with experimental data. Additionally, we exemplify defect AEPs with the case of Mn as a magnetic impurity in a wide-gap semiconductor like ZnS. Mn^{2+} in ZnS exhibits an intra-Mn d-d* orbital spin-flip transition due to the presence of Mn defect levels within the ZnS band gap. At AEPs (LDA) accurate description of Mn levels is not possible and our gap correction addresses this limitation. This combined approach of gap-corrected defect AEPs and windowed full configuration interaction (CI) [71] opens doors to studying multiplets of Mn impurities in ZnS, which remain largely unexplored with traditional *ab initio* methods due to computational demands. The underlying theoretical formalism and preliminary results for the electronic structure of Mn in ZnS, calculated using gap-corrected defect AEPs, are detailed in Chapter 6.

Chapter 2

Theory of electronic structure calculations

This chapter lays the foundation for the theoretical calculations and methods employed throughout this work. It establishes the core theoretical principles that serve as the building blocks for the specific theories presented in subsequent chapters. In some cases, these core principles will be directly applied, while other chapters will elaborate upon them with more specific details.

2.1 Description of a many-body electron system and Born-Oppenheimer approximation

The Schrödinger equation is vital to understanding the properties of quantum systems and is the cornerstone for electronic structure calculations. It has two distinct forms: the time-dependent Schrödinger equation

$$i\hbar\frac{\partial}{\partial t}\Psi(\mathbf{r},t) = \hat{H}\Psi(\mathbf{r},t), \tag{2.1}$$

which describes temporal changes in the quantum system, and the time-independent Schrödinger equation

$$\hat{H}\Psi(\mathbf{r}) = E\Psi(\mathbf{r}), \tag{2.2}$$

describing the stationary states of the system. The generalized Hamiltonian, $\hat{H}$, that describes a solid can be written as

$$\hat{H} = \hat{T}_e + \hat{T}_n + \hat{V}_{ee} + \hat{V}_{nn} + \hat{V}_{en}, \tag{2.3}$$

where $\hat{T}_e$ and $\hat{T}_n$ represent the kinetic energies of the electrons and nuclei in the system, respectively. Similarly, $\hat{V}_{ee}$, $\hat{V}_{nn}$, and $\hat{V}_{en}$ denote the Coulombic electron-electron, nucleus-nucleus, and electron-nucleus interactions, respectively. For an N electron system, $\hat{H}$ (in SI units) can be described as

$$\begin{aligned}\hat{H} = &-\frac{\hbar^2}{2}\sum_{\mathrm{A}}\frac{\nabla^2_{\mathbf{R}_A}}{M_A} - \frac{\hbar^2}{2}\sum_i \frac{\nabla^2_{\mathbf{r}_i}}{m_{\mathrm{e}}} \\ &- \frac{1}{4\pi\epsilon_0}\sum_{A,j}\frac{e^2 Z_A}{\mid \mathbf{R}_A - \mathbf{r}_j \mid} + \frac{1}{8\pi\epsilon_0}\sum_{\substack{i,j \\ i\neq j}}\frac{e^2}{\mid \mathbf{r}_i - \mathbf{r}_j \mid} + \frac{1}{8\pi\epsilon_0}\sum_{\substack{A,B \\ A\neq B}}\frac{e^2 Z_A Z_B}{\mid \mathbf{R}_A - \mathbf{R}_B \mid}.\end{aligned} \tag{2.4}$$

where i, j and A, B denote electrons and nuclei, respectively. Furthermore, Z_A is the charge of nuclei A and M_A its mass, whereas R_{AB} represents the distance between nuclei A and B. Analogously, r_{ij} is the distance between electrons i and j, whereas r_{iA} describes the distance between electron i and nucleus A. ϵ_0 is the permittivity of vacuum and e is the electron charge.

The exact many-body (MB) Schrödinger equation is analytically and numerically unsolvable due to the involvement of $3N$ coupled degrees of freedom. Due to the complexity of the problem, approximations are necessary to make it solvable. The first approximation we introduce is the Born-Oppenheimer (BO) approximation [72]. BO approximation is based on the idea that the mass of an electron is much smaller than that of a proton ($m_p/m_e \approx 1836$) and therefore, electrons in a solid can be assumed to reach an equilibrium state on a much shorter timescale than the nuclei. Henceforth, BO allows for the adiabatic treatment of the nuclei, which means that the nuclear motion can be treated independently of the electronic motion. This allows for the separation of the nuclear and electronic components of the many-body wavefunction. Formally,

$$\Psi(\mathbf{r}_i; \mathbf{R}_A) = \psi(\mathbf{r}_i; \{\mathbf{R}_A\})\phi(\mathbf{R}_A), \tag{2.5}$$

where $\psi(\mathbf{r}_i; \{\mathbf{R_A}\})$ is the electronic wavefunction in a frozen ion configuration $\{\mathbf{R_A}\}$. $\phi(\mathbf{R}_A)$ is the ionic wavefunction describing the nuclear motion under the influence of the

Coulomb potential and the time-averaged adiabatic electronic potential. Thus, the MB problem transforms into a many-electron problem, and the electronic (el) Hamiltonian can be written as:

$$\left(-\frac{\hbar^2}{2}\sum_i \frac{\nabla^2_{\mathbf{r}_i}}{m_\mathrm{e}} - \frac{1}{4\pi\epsilon_0}\sum_{A,j}\frac{e^2 Z_A}{\mid \mathbf{R}_A - \mathbf{r}_j \mid} + \frac{1}{8\pi\epsilon_0}\sum_{\substack{i,j \\ i\neq j}}\frac{e^2}{\mid \mathbf{r}_i - \mathbf{r}_j \mid} + \frac{1}{8\pi\epsilon_0}\sum_{\substack{A,B \\ A\neq B}}\frac{e^2 Z_A Z_B}{\mid \mathbf{R}_A - \mathbf{R}_B \mid}\right)\psi(\mathbf{r}_i, \{\mathbf{R}_A\}) = E_\mathrm{el}\psi(\mathbf{r}_i, \{\mathbf{R}_A\}). \tag{2.6}$$

While the BO approximation significantly simplifies the complex many-body problem, solving the resulting Schrödinger equation (Eq. 2.6) remains a challenge for most systems. Several approximate methods, such as the Hartree-Fock (HF) method, DFT, and quantum Monte Carlo (QMC) methods [73], are available for solving the many-electron Schrödinger equation. Over the past few decades, DFT has been quite successful in describing the properties of materials with great accuracy at a reasonable computational cost. DFT solves the many-electron Schrödinger equation by using the electronic density as the central variable instead of the wavefunction, thus reducing the degrees of freedom by N.

2.2 Density Functional Theory

All modern-day density functional theories stand on the two landmark theorems formulated by P. Hohenberg and W. Kohn in 1964 [74]. The first theorem states that: *"the external potential $V_\mathrm{ext}(\mathbf{r})$ is (to within a constant) a unique functional of $n_0(\boldsymbol{r})$; since in turn $V_\mathrm{ext}(\mathbf{r})$ fixes $\hat{H}$ we see that the full many particle ground state is a unique functional of $n_0(\boldsymbol{r})$".* The proof of this theorem is based on *reductio ad absurdum* (see ref. [74]) and reducing the many-body problem to a one-body problem with a total energy E_0 that can be written as a functional of the density. Since the exact ground state energy E_0 is a functional of $n_0(\mathbf{r})$, so must be all its individual components: the kinetic energy T_e, the potential energy due to the interaction between electrons E_ee, and the potential energy $E_\mathrm{ext}[n_0(\mathbf{r})]$ due to the interaction between electron and the external potential. Therefore, the exact functional $E_0[n_0(\mathbf{r})]$ is given as:

$$E_0[n_0(\mathbf{r})] = T_\mathrm{e}[n_0(\mathbf{r})] + E_\mathrm{ee}[n_0(\mathbf{r})] + E_\mathrm{ext}[n_0(\mathbf{r})]. \tag{2.7}$$

Here the last term, $E_{\text{ext}}[n_0(\mathbf{r})] = \int n_0(\mathbf{r}) V_{\text{ext}}\, d\mathbf{r}$ depends on the system whereas the first two terms are universal. Now we can introduce the Hohenberg-Kohn functional (HK),

$$F_{\text{HK}}[n_0(\mathbf{r})] = T_e[n_0(\mathbf{r})] + E_{\text{ee}}[n_0(\mathbf{r})], \tag{2.8}$$

which describes the universal part of the ground state energy, and thus is of the same form for all electronic systems. If $F_{\text{HK}}[n_0(\mathbf{r})]$ is known exactly, the Schrödinger equation of the many-electron problem can be solved exactly. However, the forms of $T[n_0(\mathbf{r})]$ and $E_{\text{ee}}[n_0(\mathbf{r})]$ are not explicitly defined. $E_{\text{ee}}[n_0(\mathbf{r})]$ is composed of the classical Coulomb energy (Hartree energy) $E_{\text{H}}[n_0(\mathbf{r})]$, and the exchange and correlation interactions (XC), $E_{\text{XC}}[n_0(\mathbf{r})]$, where the latter includes non-classical and non-local effects. Formally, we can write:

$$E_{\text{ee}}[n_0(\mathbf{r})] = E_{\text{H}}[n_0(\mathbf{r})] + E_{\text{XC}}[n_0(\mathbf{r})]. \tag{2.9}$$

The major challenge in DFT is to determine the explicit expressions for $T_{\text{e}}[n(\mathbf{r})]$ and $E_{\text{ee}}[n(\mathbf{r})]$. Till now we have established that the ground state density determines uniquely the Hamiltonian and all properties of interest for a given system. The question that arises is how do we know exactly if any electron density $n(\mathbf{r})$ is the actual ground state density. This is answered by the second Hohenberg-Kohn theorem which states that the $E[n_0(\mathbf{r})]$ is minimum only and only for the true ground state electron density $n_0(\mathbf{r})$. This is simply the variational principle which in the present context is expressed as:

$$E[n_0(\mathbf{r})] \leq E[n(\mathbf{r})] = T[n(\mathbf{r})] + E_{\text{H}}[n(\mathbf{r})] + E_{\text{XC}}[n(\mathbf{r})] + E_{\text{ext}}[n(\mathbf{r})]. \tag{2.10}$$

It is not straightforward and practical to solve the many-body problem within the Hohenberg-Kohn formalism because the form of the universal functional $F_{\text{HK}}[n_0(\mathbf{r})]$ is not known. The electrostatic term $E_{\text{H}}[n_0(\mathbf{r})]$ can be expressed explicitly, but the functional forms of the remaining two terms, $T[n_0(\mathbf{r})]$ and $E_{\text{XC}}[n(\mathbf{r})]$, are unknown and therefore, must be approximated. After Hohenberg and Kohn stated their two theorems, in 1965, Kohn and Sham proposed a formalism to the unknown universal functional E_{HK} [75]. They introduced an auxiliary system of non-interacting electrons with the same ground-state electron density as the interacting system. The idea is now to compute the true kinetic energy by separating it into two parts. The main part is equal to the kinetic energy of the non-interacting reference system $T_{\text{S}}[n_0(\mathbf{r})]$ and the smaller remainder $T_{\text{XC}}[n_0(\mathbf{r})]$ is to be approximated. The universal functional

$F_{\mathrm{HK}}[n(\mathbf{r})]$ can thus be presented as:

$$F_{\mathrm{HK}}[n_0(\mathbf{r})] = T_{\mathrm{S}}[n_0(\mathbf{r})] + E_H[n_0(\mathbf{r})] + E_{\mathrm{XC}}[n_0(\mathbf{r})], \tag{2.11}$$

where $E_{\mathrm{XC}}[n_0(\mathbf{r})]$ is the so-called exchange-correlation energy. $E_{\mathrm{XC}}[n_0(\mathbf{r})]$ contains the non-classical effects as well as part of the kinetic energy. Up to now only $E_{\mathrm{XC}}[n_0(\mathbf{r})]$ is the energy contribution we do not know how to treat properly. However, with the introduction of a non-interacting system, it is formally possible to replace the many-electron wavefunction Ψ with a set of the single-particle (SP) wavefunctions or orbitals, ψ_i [75]. The electron density is then given as:

$$n_0(\mathbf{r}) = \sum_i l_i |\psi_i^2|, \tag{2.12}$$

where l_i is the occupation number. Now, the total energy of the electronic system is written (in atomic units) as:

$$\begin{aligned} E[n_0(\mathbf{r})] &= T_{\mathrm{S}}[n_0(\mathbf{r})] + E_H[n_0(\mathbf{r})] + E_{\mathrm{XC}}[n_0(\mathbf{r})] + E_{\mathrm{ext}}[n_0(\mathbf{r})] \\ &= T_{\mathrm{S}}[n_0(\mathbf{r})] + \frac{1}{2}\int\int \frac{n_0(\mathbf{r}_1)n_0(\mathbf{r}_2)}{r_{12}} d\mathbf{r}_1 d\mathbf{r}_2 + E_{\mathrm{XC}}[n_0(\mathbf{r})] + \int V_{\mathrm{ext}} n_0(\mathbf{r}) d\mathbf{r} \\ &= -\frac{1}{2}\sum_i^N \langle\psi_i|\nabla^2|\psi_i\rangle + \frac{1}{2}\sum_i^N\sum_j^N \int\int \mid \psi_i(\mathbf{r}_1) \mid^2 \frac{1}{r_{12}} \mid \psi_j(\mathbf{r}_2) \mid^2 d\mathbf{r}_1 d\mathbf{r}_2 \\ &+ E_{\mathrm{XC}}[n_0(\mathbf{r})] - \sum_i^N \int \sum_A^{N_A} \frac{Z_A}{r_{iA}} \mid \psi_i(\mathbf{r}_1) \mid^2 d\mathbf{r}_1. \end{aligned} \tag{2.13}$$

Now, we can obtain the ground state energy by minimizing the total energy functional $E[n_0(\mathbf{r})]$, as in equation (2.13), with the normalized SP wavefunctions $\langle\psi_i|\psi_j\rangle = \delta_{ij}$. This is equivalent to solving a set of self-consistent equations

$$\left[-\frac{1}{2}\nabla^2 + \left(\int \frac{n(\mathbf{r}_2)}{r_{12}} d\mathbf{r}_2 + V_{\mathrm{XC}}(\mathbf{r}_1) - \sum_A^{N_A} \frac{Z_A}{r_{iA}}\right)\right]\psi_i = \left[-\frac{1}{2}\nabla^2 + V_{\mathrm{KS}}(\mathbf{r}_1)\right]\psi_i = \epsilon_i\psi_i, \tag{2.14}$$

which are the well-known Kohn-Sham equations. The term V_{XC} is the potential due to the exchange-correlation energy, and is simply the functional derivative of E_{XC} w.r.t. $n_0(\mathbf{r})$,

$$V_{\mathrm{XC}}(\mathbf{r}) = \frac{\delta E_{\mathrm{XC}}}{\delta n_0(\mathbf{r})}. \tag{2.15}$$

Unfortunately, there is no method so far that can determine E_{XC} explicitly and exactly. Therefore, approximations are usually employed to calculate E_{XC}.

The E_{XC} functional's non-local nature and non-analytic relationship with the electron density in real systems make its calculations a complex and demanding task. In the simplest approximation the exchange and correlation energies are calculated from the solution of the homogeneous electron gas [75]. This widely used approximation is known as the Local Density Approximation (LDA) where $E_{\mathrm{XC}}[n_0(\mathbf{r})]$ can be expressed as

$$E_{\mathrm{XC}}^{\mathrm{LDA}}[n_0(\mathbf{r})] = \int n_0(\mathbf{r})\varepsilon_{\mathrm{XC}}(n_0(\mathbf{r}))d\mathbf{r}, \tag{2.16}$$

where $\varepsilon_{\mathrm{XC}}(n_0(\mathbf{r}))$ is the exchange-correlation energy per electron for a homogeneous electron gas corresponding to the electron density $n_0(r)$. The exchange-correlation energy per electron $\varepsilon_{\mathrm{XC}}(n_0(\mathbf{r}))$ can be written as a sum of exchange and correlation contributions

$$\varepsilon_{\mathrm{XC}}(n_0(\mathbf{r})) = \varepsilon_{\mathrm{X}}(n_0(\mathbf{r})) + \varepsilon_{\mathrm{C}}(n_0(\mathbf{r})), \tag{2.17}$$

where the exchange energy per electron, $\varepsilon_{\mathrm{X}}(n_0(\mathbf{r})) := \varepsilon_{\mathrm{X}}^{\mathrm{hom}}(n_0(\mathbf{r}))$, is taken from the results obtained for the homogeneous electron gas in the Slater approximation, based on the Hartree-Fock method, the so-called called Slater exchange [76]

$$\varepsilon_{\mathrm{X}}(n_0(\mathbf{r})) = -\frac{3}{4}\sqrt[3]{\frac{3n_0(\mathbf{r})}{\pi}}. \tag{2.18}$$

Although there is no explicit expression of the correlation contributions, a functional form of the correlation energy has been parametrized using highly accurate quantum Monte-Carlo numerical simulations of the homogeneous electron gas performed by Ceperly and Alder in 1980. One famous parametrization of $\varepsilon_{\mathrm{C}}(n_0(\mathbf{r}))$ was presented by Perdew and Zunger in 1981 [77]. In 1992, Perdew and Wang provided another simple analytic representation of $\varepsilon_{\mathrm{C}}(n_0(\mathbf{r}))$, which is still widely used [78]. The local spin density approximation (LDA) and its extension to spin-polarized systems, the so-called local spin density approximation (LSDA) provides a rather accurate description of structural and vibrational properties, such as lattice constants, bulk moduli, and phonon vibrational frequencies for weakly correlated solid systems. For the cohesive energy of solids, the dissociation energy of molecules and the ionization energy of atoms LDA is less accurate as it assumes a local nature of the E_{XC}.

However, the interacting systems do not have nearly uniform electron densities.

LDA ignores the effect of inhomogeneities of the electron density and this prompted the introduction of functionals that depend on more than just the local value of the density. The generalized gradient approximations (GGA) are the set of functionals that depend on the electron density and its first gradient

$$E_{xc}^{GGA} = E_{xc}[n_0, \nabla n].$$

Continuing along this path, more complicated and computationally expensive approaches [79, 80] have been proposed, but not used in this work.

2.3 Periodic supercell and plane-wave pseudopotential method

Although DFT solves an effective SP picture, the problem is to expand the SP eigenstates of the Kohn–Sham equations. The plane waves, which are the exact eigenfunctions of the homogeneous electron gas, are particularly well-suited expansion for the periodic systems.

Bloch's theorem states that for any perfect periodic system, the SP electronic wavefunction (for j^{th} eigenstate) can be written as

$$\psi_j(\mathbf{r}) = e^{i\mathbf{kr}} u_j(\mathbf{r}), \tag{2.19}$$

where $u_i(\mathbf{r})$ is a periodic function with the same periodicity as the system. $u_i(\mathbf{r})$ can be expanded in a discrete plane-wave basis set whose wave vectors ($\mathbf{k}$) are reciprocal space vectors ($\mathbf{G}$) of the crystal

$$u_j(\mathbf{r}) = \sum_{\mathbf{G}} c_{j,\mathbf{G}} e^{i\mathbf{Gr}}. \tag{2.20}$$

The electronic wavefunction can be written as the sum of plane waves

$$\psi_j(\mathbf{r}) = \sum_{\mathbf{G}} c_{j,\mathbf{k}+\mathbf{G}} e^{i(\mathbf{k}+\mathbf{G})\mathbf{r}}. \tag{2.21}$$

However, one needs an infinite number of plane waves to expand an electronic wavefunction, leading to large computational costs. Therefore it is important to truncate this expansion to only plane waves with the kinetic energy lower than cutoff energy,

namely $E_{\text{cut}} \geq (\hbar^2/2m)|\mathbf{k}+\mathbf{G}|^2$. The errors in the total energy due to this truncation can be minimized by the convergence of the total energy w.r.t. E_{cut}.

Solving the Schrödinger equation with full potential can be computationally expensive due to the high oscillation frequencies near the nuclei. Since valence electrons are primarily responsible for the physical properties of the material, core, and valence electrons can be treated separately. As core electrons are localized and strongly bound to the nuclei, they can be treated together with the nuclei via so-called pseudopotential approximation. Here the strong ionic potential is replaced by a weaker and smoother pseudopotential acting on the pseudo wavefunctions part of the valence electrons.

The pseudopotential needs to be constructed in such a way that the scattering properties are preserved and beyond a certain cutoff radius r_{C}, both pseudopotential and the real potential are identical. There are different forms of pseudopotential used such as projector augmented potentials (PAW), norm-conserving pseudopotential (NCPP), and ultrasoft pseudopotential (USPP). Throughout this work, the NCPPs were introduced by D. Hamann, M. Schlüter, and C. Chiang. [81] are used (unless specified). For the high transferability and the preserved scattering properties NCPP has to satisfy four criteria:
(i) Real and pseudo valence eigenvalues agree for the reference configuration.
(ii) Real and pseudo atomic wavefunctions agree beyond a chosen "core radius" r_{C}.
(iii) The integrals from 0 to r of the real and pseudo charge densities agree for $r > r_{\text{C}}$ for each valence state (norm conservation).
(iv) The logarithmic derivatives of the real and pseudo wavefunction and their first energy derivatives agree for $r > r_{\text{C}}$.

2.4 Configuration Interaction Method

SP picture assumes that electrons move independently of each other resulting in underestimated electron correlations. Electron correlation is vital for interpreting experimental spectra and predicting electronic transitions. Different methods such as CI, and coupled clusters include electron correlations. CI includes correlations by considering multiple electronic configurations where electrons are allowed to interact with each other. It is the matrix mechanics solution of the time-independent non-relativistic electronic Schrödinger equation. In CI, the wavefunction is a linear combination of Slater

determinants and the linear coefficients are determined variationally. Here, we discuss the CI method in detail.

2.4.1 N-particle wavefunctions

For any given complete set of functions $\psi_i(x_1)$ of a single variable x_1, we can expand any function $\phi(x_1)$ as:

$$\phi(x_1) = \sum_i a_i \psi_i(x_1), \tag{2.22}$$

where a_i are the expansion coefficients. Considering a two-particle system, the function $\phi(x_1, x_2)$ keeping x_2 fixed, we have:

$$\phi(x_1, x_2) = \sum_i a_i(x_2) \psi_i(x_1), \tag{2.23}$$

where $a_i(x_2)$ can be written as:

$$a_i(x_2) = \sum_j b_{ij} \psi_j(x_2). \tag{2.24}$$

Now from 2.23 and 2.24, we have $\phi(x_1, x_2)$ as:

$$\phi(x_1, x_2) = \sum_{ij} b_{ij} \psi_i(x_1) \psi_j(x_2). \tag{2.25}$$

However, electrons are fermions and the many-particle wavefunction must be antisymmetric w.r.t. the exchange of the coordinates of any two electrons as per the Pauli exclusion principle. For example, in case of $\phi(x_1, x_2)$, it means

$$\phi(x_1, x_2) = -\phi(x_2, x_1), \tag{2.26}$$

which is equivalent to $b_{ij} = -b_{ji}$ and $b_{ii} = 0$, or

$$\phi(x_1, x_2) = \sum_{j>i} b_{ij} [\psi_i(x_1) \psi_j(x_2) - \psi_j(x_1) \psi_i(x_2)]. \tag{2.27}$$

We can express $\phi(x_1, x_2)$ in the Slater determinants form as:

$$\phi(x_1, x_2) = \sum_{j>i} b_{ij} b_{ij} \begin{vmatrix} \psi_i(x_1) & \psi_j(x_1) \\ \psi_i(x_2) & \psi_j(x_2) \end{vmatrix}. \tag{2.28}$$

Similarly, we can construct any N-particle wavefunction as a linear combination of all possible N-particle Slater determinants formed from a complete set of SP wavefunctions $\psi_i(x)$. The solution of the many-body equation (2.3) in this complete basis set can be written as

$$|\Psi_j\rangle = \sum_i c_{ij} |\phi_i\rangle , \tag{2.29}$$

where $|\phi_i\rangle$ denotes N-particle basis functions. $|\Psi_j\rangle$ can be written as excitations from the Hartree-Fock "reference" determinants, i.e.

$$|\Psi_j\rangle = c_0 |\phi_0\rangle + \sum_{ra} c_a^r |\phi_a^r\rangle + \sum_{a<b,r>s} c_{ab}^{rs} |\phi_{ab}^{rs}\rangle + \sum_{r<s<t,a<b<c} c_{abc}^{rst} |\phi_{abc}^{rst}\rangle + ..., \tag{2.30}$$

where $|\phi_a^r\rangle$ means Slater determinant formed by replacing spin-orbital a in ground state $|\phi_0\rangle$ with spin-orbital r, and so on.

If we include all possible N-particle basis functions $\{|\phi_i\rangle\}$ formed by a given SP basis set $\{\psi_i(x)\}$ then it is called full-CI calculations. However, with the increasing N, it is impossible to use a complete set of SP basis function $\{\psi_i(x)\}$ in calculations. For a reasonable computational cost, a reduced but large enough basis set can be used to obtain good results. The quality/accuracy of the SP basis set used for the calculation can be checked by comparing the results of subsequent calculations using a progressively larger basis set.

Unfortunately, a full-CI calculation is still computationally expensive even with an incomplete SP basis set. Therefore, a reduced CI space is usually used in the calculations. So far, CI singles and doubles (CISD) are the most used approximation, which includes only those N-particle basis functions that represent single or double excitations relative to a given reference state. The reference state can be constructed using any ground state on a SP basis.

2.4.2 Screened CI calculation

The first step is to solve the SP Schrödinger equation to obtain $\psi_i(\mathbf{r}, \sigma)$. In the second step, obtained SP basis functions set $|\phi_i\rangle$ is used to construct a set of single-substitution Slater determinants $\Phi_{h,e}$ for the exciton. $\Phi_{h,e}$ is obtained from the ground-state determinant Φ_0 by promoting an electron from the occupied (h) valence state ψ_h with energy ε_h to the unoccupied (e) conduction state ψ_e with energy ε_e [63, 61]. The exciton wavefunctions Ψ^α (where α denotes the exciton quantum numbers) are expanded

in terms of the determinants basis set [63] as:

$$\Psi^{\alpha} = \sum_{h}^{N_h} \sum_{e}^{N_e} C_{h,e}^{\alpha} \Phi_{h,e}, \tag{2.31}$$

for N_{h} and N_e being the number of valence and conduction band states to be included in the expansion of the exciton wavefunctions. The matrix elements of the many-particle Hamiltonian H with basis set $\Phi_{h,e}$ are calculated as [63]:

$$\begin{aligned} H_{he,h'e'} &= \langle \Phi_{h,e} | \, H \, | \Phi_{h',e'} \rangle \, , \\ &= (\varepsilon_e - \varepsilon_h)\delta_{h,h'}\delta_{e,e'} - J_{he,h'e'} + K_{he,h'e'}, \end{aligned} \tag{2.32}$$

where J and K are the Coulomb and exchange integrals, respectively:

$$J_{he,h'e'} = e^2 \sum_{\sigma_1,\sigma_2} \int\int \frac{\psi_{h'}^{*}(\mathbf{r}_1,\sigma_1)\psi_{e}^{*}(\mathbf{r}_2,\sigma_2)\psi_{h}(\mathbf{r}_1,\sigma_1)\psi_{e'}(\mathbf{r}_2,\sigma_2)}{\epsilon(\mathbf{r}_1,\mathbf{r}_2)|\mathbf{r}_1-\mathbf{r}_2|} d\mathbf{r}_1 d\mathbf{r}_2, \tag{2.33}$$

$$K_{he,h'e'} = e^2 \sum_{\sigma_1,\sigma_2} \int\int \frac{\psi_{h'}^{*}(\mathbf{r}_1,\sigma_1)\psi_{e}^{*}(\mathbf{r}_2,\sigma_2)\psi_{e'}(\mathbf{r}_1,\sigma_1)\psi_{h}(\mathbf{r}_2,\sigma_2)}{\epsilon(\mathbf{r}_1,\mathbf{r}_2)|\mathbf{r}_1-\mathbf{r}_2|} d\mathbf{r}_1 d\mathbf{r}_2, \tag{2.34}$$

where $\sigma_{1,2}$ are spin indices and $\epsilon(\mathbf{r}_1,\mathbf{r}_2)$ is the dielectric screening function as a consequence of the neglected excitations from the deep core states. $\epsilon(\mathbf{r}_1,\mathbf{r}_2)$ is microscopic and isotropic i.e. $\epsilon(\mathbf{r}_1,\mathbf{r}_2) = \epsilon(|\mathbf{r}_1-\mathbf{r}_2|)$. It has both the long- and short-range of interaction. Since an electron is screened by the presence of other electrons as well as moving ions, the dielectric function $\epsilon^{-1}(\mathbf{k})$ has an electronic (high-frequency) $\epsilon_{\mathrm{el}}^{-1}$ and an ionic (low-frequency) contribution $\epsilon_{\mathrm{ion}}^{-1}$. In reciprocal space we can write this [82, 63]:

$$\epsilon^{-1}(\mathbf{k}) = \epsilon_{\mathrm{el}}^{-1}(\mathbf{k}) + \epsilon_{\mathrm{ion}}^{-1}(\mathbf{k}). \tag{2.35}$$

For the electronic part $\epsilon_{\mathrm{el}}^{-1}$, the Thomas-Fermi model proposed by Resta [83] is used while the ionic (or polaronic) part $\epsilon_{\mathrm{ion}}^{-1}$ is included using a derivation by Haken [82]:

$$\epsilon_{\mathrm{el}}^{-1}(\mathbf{k}) = \frac{\mathbf{k}^2 + \mathrm{q}^2 \sin(\mathbf{k}\mathrm{n}_\infty)/(\epsilon_\infty^{\mathrm{dot}}\mathbf{k}\mathrm{n}_\infty)}{\mathbf{k}^2 + \mathrm{q}^2}, \tag{2.36}$$

$$\Delta\epsilon_{\mathrm{ion}}^{-1}(\mathbf{k}) = \Big(\frac{1}{\epsilon_0^{\mathrm{dot}}} - \frac{1}{\epsilon_\infty^{\mathrm{dot}}}\Big) + \Big(\frac{1/2}{1+\mathrm{n_h^2}\mathbf{k}^2} + \frac{1/2}{1+\mathrm{n_e^2}\mathbf{k}^2}\Big), \tag{2.37}$$

with $q = 2\pi^{-1/2}(3\pi^2 n_0)^{1/3}$ being the Thomas-Fermi wave vector, n_0 is the electron density, n_∞ is the screening radius which can be calculated from $\sinh(qn_\infty)/(qn_\infty) = \epsilon_\infty^{\text{dot}}$, and $n_{h,e} = (\hbar/2m_{h,e}\omega_{\text{LO}})^{1/2}$, where $m_{h,e}$ are hole (h) and electron (e) effective masses, ω_{LO} is the frequency of the bulk LO phonon mode [63]. To include the size dependence (R) , the high-frequency dielectric constant is obtained from a modified Penn model [84, 63],

$$\epsilon_\infty^{\text{dot}}(R) = 1 + (\epsilon_\infty^{\text{bulk}} - 1)\frac{\left[E_{\text{gap}}^{\text{bulk}} + \Delta E\right]^2}{\left[E_{\text{gap}}^{\text{dot}} + \Delta E\right]^2}, \tag{2.38}$$

where $\epsilon_\infty^{\text{bulk}}$ is the bulk high-frequency dielectric constant of the material, $E_{\text{gap}}^{\text{bulk}}$ and $E_{\text{gap}}^{\text{dot}}$ are the SP bulk and QD band gaps, ΔE denotes the difference between the so-called E_2 and E_0 transitions in bulk. For semiconductors with tetrahedral crystal structure, E_2 is the transition with the strongest absorption [85]. The low-frequency dielectric constant is given as [63]:

$$\epsilon_0^{\text{dot}}(R) = \epsilon_\infty^{\text{dot}}(R) + (\epsilon_0^{\text{bulk}} - \epsilon_\infty^{\text{bulk}}). \tag{2.39}$$

Hence, the dielectric function depends both on the electron-hole separation as well as the dot size. Now the diagonalization of the many-body Hamiltonian is done to obtain the many-body eigenvectors and eigenenergies.

Chapter 3

Origin of the High-Frequency Shoulder in the Raman Spectra of CdSe Quantum Dots

This chapter is adapted from the published work 'Origin of the High-frequency Shoulder in Raman Spectra of CdSe Quantum Dots,' by **S. Kumar**, T. Steenbock, and G. Bester; *J. Phys. Chem. Lett.* 2024, 15, 41, 10392–10398 [86]. All calculations, data analysis, and drafting of the manuscript were conducted by the first author, **S. Kumar**.

Cadmium selenide (CdSe) QDs from sub-2 nm to tens of nm [31, 32, 33, 21, 34, 35, 36, 37, 38] are of great interest due to their size tunable optical properties. Their optical properties can be tailored by different factors such as size [38], shape anisotropy [68], ligands [20, 32, 33, 21], the surface stoichiometry [34], and surface defects [35, 58, 56], as emphasized by various experimental and theoretical studies. The optical properties are directly influenced by their vibrational dynamics which lead to the appearance of rich phonon sidebands [39, 40, 41] and eventually shape the recombination dynamics [42, 43]. Raman spectroscopy is an effective technique to probe these vibrational properties [44, 45, 46, 47, 48, 49, 50, 51, 5, 52], revealing, e.g., valuable information about alloying and strain at core-shell interfaces [53, 44, 54]. Based on Raman spectra, vibrations in CdSe QDs have been identified as bulk-like for diameters ≥ 2.1 nm or molecule-like for diameters < 2 nm [5]. For larger QDs (both core and core/shell), distinct longitudinal optical (LO) (bulk-like) and surface-optical (SO) peaks have been observed in the Raman spectra. The behavior of these peaks, influenced by factors such as size, strain,

and composition, has been thoroughly characterized and understood [87, 53, 46, 47, 88, 89, 90, 45].

In addition to the well-established LO and SO peaks, Raman spectra of CdSe QDs often show a high-frequency shoulder (HFS) centered around 230 cm^{-1} above the LO region [46, 44, 51, 53, 45, 55]. The HFS has been observed in QDs of different sizes, ranging from 1.44 nm to 3.4 nm [44, 51, 53, 45, 55]. The origin of this HFS remains debated, with hypotheses including amorphous surface selenium [45], surface bond reconstruction [45], and coupled optical-acoustic modes [45]. The disappearance of the HFS upon CdS shell deposition [51, 46, 53] suggests a surface-related origin, yet its precise nature is not fully understood.

We use DFT to calculate the Raman intensity of realistic ligand-covered QDs with an emphasis on twofold coordinated Se-defect sites, that have been shown to play an important role in small CdSe QDs [56, 57, 58]. While simplified models accurately predict Raman spectra of larger structures [91, 87, 47, 92], they are inadequate for capturing the surface effects that will turn out to be crucial for smaller QDs. Prior *ab initio* Raman studies focused on mainly defect-free structures [52, 59, 60]. Ahmed et al. [60] focused primarily on QDs interactions with capping ligands by demonstrating how vibrational spectroscopy can be useful for studying surface–ligand interactions. Manav et *al.* [59] investigated the impact of non-stoichiometry on Raman spectra of CdSe QDs. Therefore, so far the importance of defects mainly remains unexplored from a theoretical standpoint which we address here.

3.1 Raman spectroscopy

Raman spectroscopy is a non-destructive class of vibrational spectroscopy that uses light to inelastically scatter photons, inducing vibrational transitions in material. Inelastic scattering of light causes the incident photon (frequency ω) to either lose energy $\hbar\omega_s = \hbar\omega - \hbar\omega_p$ (Stokes scattering) or gain energy $\hbar\omega_s = \hbar\omega + \hbar\omega_p$ (Anti-Stokes scattering) after the scattering, where ω_s and ω_p is the frequency of scattered light and phonon respectively. Fig. 3.1 illustrate the excitation and de-excitation of energy levels in Stokes and Anti-stokes scattering in Raman Spectroscopy. These phonons are fundamental vibration motions induced by the collective excitation of atoms or molecules in a periodic and elastic arrangement. It corresponds to a lattice of atoms or molecules vibrating evenly at a single frequency. This frequency is known as the normal mode

frequency, and it is crucial because the lattice vibrations (or the phonons) can be expressed as a superposition of these fundamental vibrations.

Microscopically, Raman scattering is caused by photon-phonon interaction, and its intensity is defined by the change in polarizability w.r.t. atomic displacement corresponding to a certain vibration mode. For the first time, Raman and Krishnan observed the scattered light with distinct sidebands symmetrically arranged around the incident frequency in liquids [93].

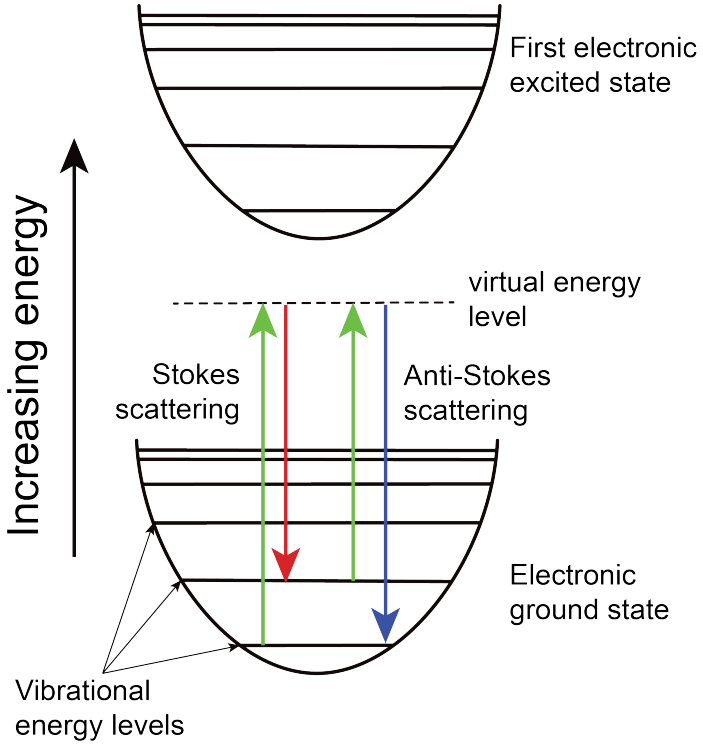

Figure 3.1: Illustration of excitation and de-excitation in energy levels using Stokes and Anti-stokes scattering in Raman spectra. Reprinted from ref. [94].

3.1.1 Vibrational analysis and Raman Calculations

The harmonic oscillator model under the Born-Oppenheimer approximation is commonly used in computing normal modes and thus the Raman spectra. When a molecule (or the considered material) is in equilibrium, it resides at the lowest energy point (at least locally) on its potential energy surface (PES). Around this equilibrium position, the PES profile is approximated as parabolic allowing us to treat the second derivative of energy w.r.t. a nuclear coordinate as a force constant for the harmonic oscillation of an atom along that coordinate. Since vibrations in materials involve multiple atoms

moving simultaneously (i.e. polyatomic vibrations), the harmonic oscillator model can be extrapolated to multiple nuclear coordinates. Furthermore, the N-dimensional nuclear coordinate harmonic oscillator can be decomposed into $3N$ independent harmonic oscillators, each corresponding to the frequency of a classical normal mode. To describe normal modes, imagine each atom (labeled with a capital letter I) is slightly shifted from its equilibrium position (denoted by R_I). This shift is described by a displacement pattern (U_I^α), where the Greek letter alpha refers to the x, y, and z directions in space. The normal mode frequencies are calculated as [95, 96, 87]:

$$\sum_{J,\beta}(C_{I,J}^{\alpha,\beta} - M_I\omega_p^2\delta_{\alpha\beta}\delta_{IJ})U_J^\beta = 0, \tag{3.1}$$

where M_I is the mass of atom I and $C_{I,J}^{\alpha,\beta}$ is the force constant (Hessian) matrix given as:

$$C_{I,J}^{\alpha,\beta}(R^\alpha - R^\beta) = \frac{\partial^2\mathcal{E}^{\mathrm{BO}}}{\partial R_I^\alpha \partial R_J^\beta}, \tag{3.2}$$

where $\mathcal{E}^{\mathrm{BO}}$ is the Born-Oppenheimer energy surface. $\tilde{C}_{IJ}^{\alpha\beta}$ can be diagonalized to obtain eigenvalues $\omega_p(q)$ and eigenvectors U_I^α.

Once the vibrational eigenvalues $\omega_p(q)$ and eigenvectors U_I^α are obtained, Raman scattering cross sections can be calculated using the polarizability theory, based on derivatives of the frequency-dependent polarizability tensor w.r.t. normal vibrational modes. The Raman scattering differential cross-section ($\frac{d\sigma}{d\Omega}$) in terms of frequency-dependent polarizability tensor is given as [97]:

$$\frac{d\sigma}{d\Omega} = k_\omega(c_i\alpha'^2(\omega) + c_j\gamma'^2(\omega)), \tag{3.3}$$

where $\alpha'(\omega)$ and $\gamma'(\omega)$ are the isotropic part and the anisotropic part of the differentiated polarizability tensor, respectively at incident frequency ω. The coefficients c_i and c_j depend on the scattering geometry and the polarization of the incident and scattered radiation. k_ω is a pre-factor given as:

$$k_\omega = \frac{\hbar}{4\,\pi\,\varepsilon_0^2\,c^4} n_v \frac{(\omega - \omega_p)^4\,g_p}{2\,\omega_p}, \tag{3.4}$$

where c is speed of light, frequency of vibration (ω_p) (or the phonon) and degeneracy of vibration (g_p) and ε_0 stands for the dielectric constant of vacuum. n_v is occupation of vibrational levels at temperature T and included through Boltzmann distribution

$1/(1-e^{hc\omega_p/k_BT})$ with h and k_B being Planck and Boltzmann constants respectively. The isotropic part $\alpha'(\omega)$ is given as:

$$\alpha'(\omega) = \frac{1}{3}\left(\alpha'_{xx} + \alpha'_{yy} + \alpha'_{zz}\right), \tag{3.5}$$

and the anisotropic part $\gamma'^2(\omega)$ is given as:

$$\begin{aligned}\gamma_i'^2 = \tfrac{1}{2}\left[(\alpha'_{xx}-\alpha'_{yy})^2 + (\alpha'_{yy}-\alpha'_{zz})^2 + (\alpha'_{xx}-\alpha'_{zz})^2\right] + \\ +\tfrac{3}{4}\left[(\alpha'_{xy}+\alpha'_{yx})^2 + (\alpha'_{xz}+\alpha'_{zx})^2 + (\alpha'_{yz}+\alpha'_{zy})^2\right],\end{aligned} \tag{3.6}$$

where α'_{mn} is differentiated polarizability with $m, n \in (x, y, z)$.

However, calculations of differentiated polarizability tensor is not straightforward and computationally expensive. Dmitrij and co-workers [98] presented an analytical implementation of first-order derivatives of frequency-dependent polarizabilities in the time-dependent density functional framework at low computational cost. Their analytical method utilizes a fully variational polarizability Lagrangian. This approach reformulates the individual components of the frequency-dependent polarizability as variational Lagrangians. The polarizability Lagrangian is given as [98]:

$$\begin{aligned}&L^{mn}[X^m, Y^m, X^n, Y^n, C, Z^{mn}, W^{mn}](\omega) \\ &\quad = \langle X^m, Y^m|\left(\Lambda - \omega\Delta\right)|X^n, Y^n\rangle + \langle X^m, Y^m|P^n, Q^n\rangle + \langle P^m, Q^m|X^n, Y^n\rangle \\ &\qquad + \sum_{ia\sigma} Z^{mn}_{ia\sigma}F_{ia\sigma} - \sum_{pq\sigma, p\leq q} W^{mn}_{pq\sigma}(S_{pq\sigma} - \delta_{pq}).\end{aligned} \tag{3.7}$$

The stationary point of L^{mn} is the negative mn component of the electronic polarizability (α'_{mn}) at the frequency ω within the adiabatic approximation. Here the supervectors $|X^{m/n}, Y^{m/n}\rangle$ contain the first-order density matrix response, expanded in the basis of products of virtual and occupied molecular orbitals and their transposes [98, 99]. These molecular orbitals (MOs) $\phi_{p\sigma}(\mathbf{r})$ are solutions of ground state spin (σ) unrestricted KS equations, as usual, indices i , j , ..., denote occupied, a , b , ..., virtual, and p , q , ..., general orbitals. The MOs are expanded in the basis of atom-centered contracted Gaussians $\chi_\mu(\mathbf{r})$ with expansion coefficients $C_{\mu p\sigma}$. The Lagrangian multipliers Z^{mn} and W^{mn} are introduced to make the MO coefficients C satisfy the ground state KS equations and S is the overlap matrix. The operators Λ

and Δ are given as:

$$\Lambda = \begin{pmatrix} A & B \\ B & A \end{pmatrix}, \quad \Delta = \begin{pmatrix} 1 & 0 \\ 0 & -1 \end{pmatrix}, \tag{3.8}$$

where $(A \pm B)$ are the electric and magnetic orbital rotation Hessians [100]. The external perturbation enters the Lagrangian through the vectors $|P^{m/n}, Q^{m/n}\rangle$ given by

$$P^{m/n}_{ia\sigma} = Q^{m/n}_{ia\sigma} = \int d^3\mathbf{r}\, \phi_{i\sigma}(\mathbf{r})\, (\mathbf{r})_{m/n}\, \phi_{a\sigma}(\mathbf{r}), \tag{3.9}$$

in the dipole-length gauge. For a stationary point of L^{mn}, the functional derivative w.r.t. all parameters must vanish, and dynamic polarizability derivatives are given by the negative derivatives of L^{mn} at its stationary point. L^{mn} is fully variational as stationarity w.r.t. $\langle X^m, Y^m|$ and $|X^n, Y^n\rangle$ leads to the time-dependent Kohn-Sham response problems (follow ref. [98, 99] for detailed discussion). Because of the fully variational nature of L^{mn}, computing the first-order derivative w.r.t. a nuclear displacement does not involve any derivatives of the parameters $X^{m/n}$, $Y^{m/n}$, C, L^{mn}, and W^{mn}. Now using variational stability and transforming to the atomic orbital (AO) basis, an expression reminiscent of the ground gradients can be obtained w.r.t. nuclear displacement (R_I)(follow ref. [98]).

Now we look back at Eq. 3.3 for a typical experimental setup where the incident light is plane-polarized (or linear) and the scattered light is measured at a 90° angle without any analyzers. For this case, we can write the differential cross section as [97]:

$$\frac{d\sigma}{d\Omega} = k_\omega \frac{(45\alpha'^2 + 7\gamma'^2)}{45}. \tag{3.10}$$

This polarizability Lagrangian-based approach is implemented in the TURBOMOLE 7.5 program package [101] which has been used for this work. All structural optimizations are carried out using Perdew–Becke–Enzerhoff (PBE) exchange-correlation functional [78, 102]. Ahlrich's double-ζ split-valence basis set with polarization functions on all atoms (def2-SVP) [103] and Grimme's empirical dispersion correction in the third generation (D3) [104] were used. Additionally, accelerated Coulomb integrals using a multipole-accelerated resolution of identity approximation (MARIJ) in the self-consistent field (SCF) algorithm [103, 105, 106, 107] were used. All structures were optimized with a convergence of 10^{-7} Hartree for energy and 10^{-6} Hartree/Bohr for the gradient. Furthermore, we have employed the aoforce module [108] for vibrational frequencies and eigenvectors. The egrad module [98] was used for Raman intensity

from the TURBOMOLE package with incident wavelength 850 nm.

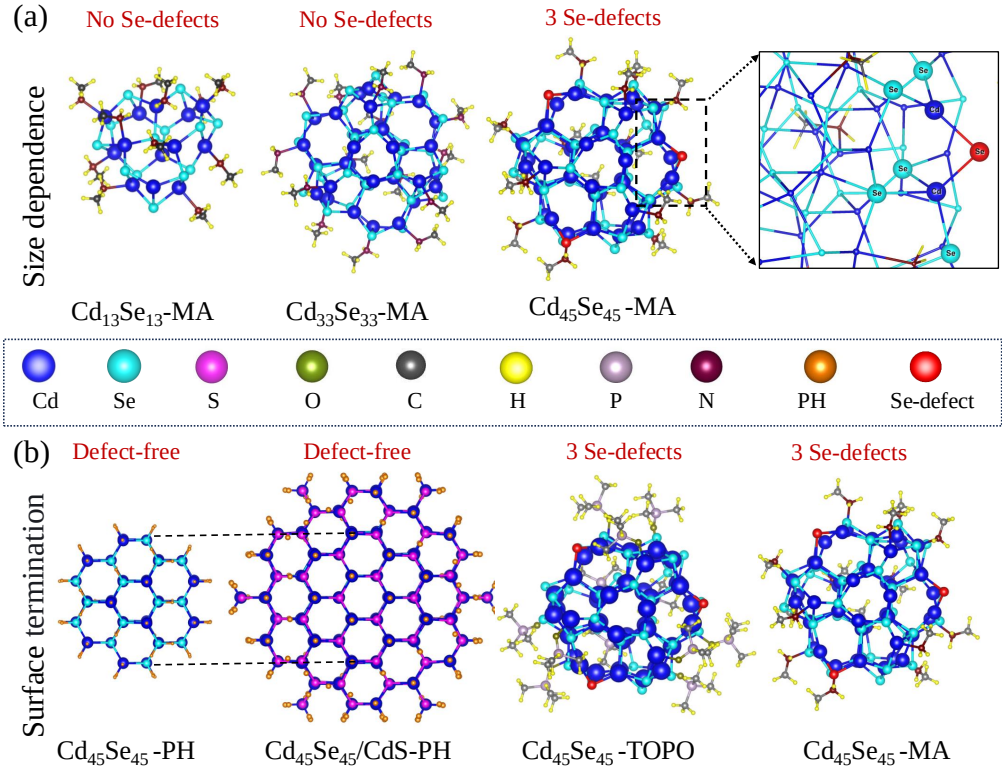

Figure 3.2: Optimized structure of (a) Methylamine (MA) passivated ultrasmall CdSe nanoclusters and QDs of varying sizes, represented by the number of constituent atoms. (b) Different surface termination of the $Cd_{45}Se_{45}$ structure including pseudohydrogen (PH), a CdS shell with PH on top, and trioctylphosphine oxide (TOPO). The inset provides an enlarged view of the local arrangement around the twofold coordinated Se defect, highlighted in red. The dotted lines delineate the core size in the core-shell structure. Reprinted from ref. [86].

3.2 Results and Discussion

In Fig. 3.2 we show the relaxed wurtzite wurtzite (WZ) nanoclusters and QDs investigated in this work. All initial structures are cut from bulk WZ lattice and subsequently relaxed to minimize the energy below the convergence criteria. The smallest structures (also experimentally realized), $Cd_{13}Se_{13}$ [109] and $Cd_{33}Se_{33}$ [109, 52, 110], are called magic-size clusters and have threefold coordinated Se, that do not develop a defect state in the gap [56, 57, 34, 58], and threefold coordinated Cd atoms that are partly passivated by methylamine (MA) (with a shortened alkyl chain compared to the experiment). This common L-type ligand selectively binds to surface Cd atoms [111, 21, 32, 33] via a co-

valent dative bond, where the nitrogen atom in MA donates an electron pair to the Cd atom. Some of the surface Cd that remain unpassivated and threefold coordinated do not form defect states in the gap. In this sense, the magic-size clusters are free from defects.

We keep the stoichiometry at 50% and increase the size to $Cd_{45}Se_{45}$. For this non-magic-size cluster, three twofold coordinated Se atoms (defects) are unavoidable in the QD construction. The top right panel of Fig. 3.2 gives a detailed view of the defect geometry: Se is bonded to a threefold Cd on one side and to a fourfold Cd on the other side. We supplement the portfolio of calculations by a trioctylphosphine oxide (TOPO, where octyl chains are replaced by methyl groups to reduce computational cost) passivated structure as well as pseudohydrogen (PH) [20, 68, 112] passivated structures. These pseudohydrogen atoms have a fractional charge of 3/2 (1/2) when attached to Cd (Se) and lead to electronic gaps free of defect states [91, 87]. We can see these structures as "ideally" passivated.

For consistency, all investigated structures will be denoted as Cd_aSe_a-(Surface/Ligand), where "a" represents the number of Cd or Se atoms in the structure and (Surface/Ligand) specifies the surface modification or ligand group attached to the CdSe core.

The L-type ligand coverage in our TOPO and MA structures is different, following literature [113, 114] we use a larger coverage for the smaller MA molecule (15) than for the bulky TOPO (12). The $Cd_{45}Se_{45}/Cd_{123}S_{129}$-PH structure is a core/shell structure where the CdSe core has the same size as the $Cd_{45}Se_{45}$-PH QD. Computational limitations prohibit the use of larger structures. In the calculations involving PH, the mass of PH is assigned the same as the atomic of the hydrogen element.

In Fig. 3.3 we show the single particle eigenvalues (a), isosurfaces of the defect molecular orbitals (DMO) (b) of the highest occupied molecular orbital (HOMO), and the lowest unoccupied molecular orbital (LUMO) (c). The isosurface values are chosen in such a way as to enclose 75% of the state density.

In Fig. 3.3a), we see that only the structures declared as defective ($Cd_{45}Se_{45}$-MA and $Cd_{45}Se_{45}$-TOPO) show defect levels (doubly occupied, shown in red) within the HOMO-LUMO gap. For these states, the wavefunction is strongly localized on the Se-defect (Fig. 3.3b)). For the $Cd_{45}Se_{45}$-MA structure the three defect levels are energetically split by as much as 263 meV, while for $Cd_{45}Se_{45}$-TOPO they remain nearly degenerate, so that the individual DMO look artificially distributed over the three defect sites.

We understand the splitting in $Cd_{45}Se_{45}$-MA as follows. In $Cd_{45}Se_{45}$-TOPO the L-

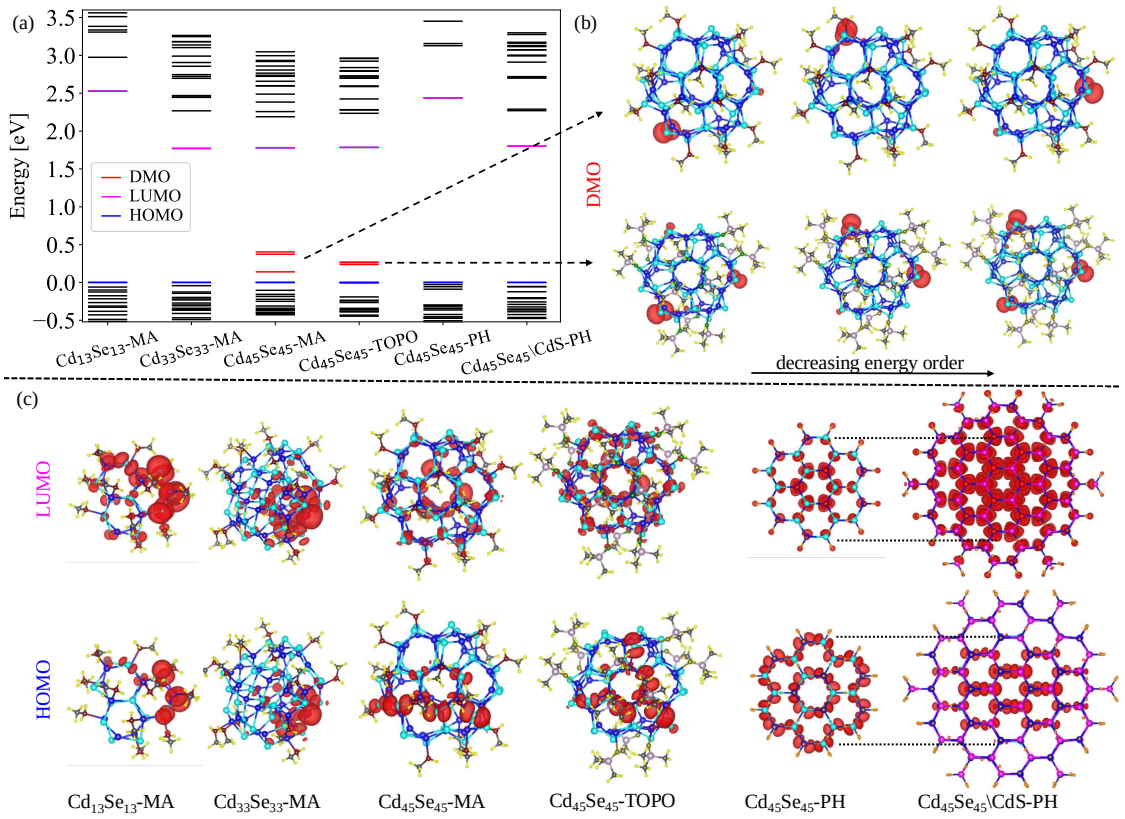

Figure 3.3: Electronic structure analysis. (a) Single-particle energy levels for the various structures (see Fig. 3.2). The HOMO, LUMO, and DMO are shown as blue, magenta, and red lines, respectively. The HOMO level is set to 0 eV for all structures. Isosurfaces of the wavefunction squared enclosing 75% of the state density for the DMOs (b), LUMO, and HOMO (c). Reprinted from ref. [86].

type ligands are placed in a relatively symmetric arrangement (although the structure has strictly speaking no remaining symmetry) and the three defect sites are nearly equivalent. The tree additional L-type ligands in $Cd_{45}Se_{45}$-MA break the symmetry (further) rendering the three defects inequivalent. A comparison of both structures (MA and TOPO) is given in Fig. 3.4. It is also interesting to see that the HOMO-LUMO gap of the smaller $Cd_{33}Se_{33}$ and the larger $Cd_{45}Se_{45}$ structures are nearly the same. This is a consequence of the hybridization of the DMO with the HOMO which pushes the HOMO to lower energy, opening the HOMO-LUMO gap in the defective larger structure.

In Fig. 3.3c) we notice that the HOMO tends to be more localized than the LUMO, in accordance to the heavier hole effective mass. This is also true for the magic size clusters we described earlier as "defect-free" and now exhibit a hole localization in an off-center location. It is clear that a static calculation for a chosen geometry, such as

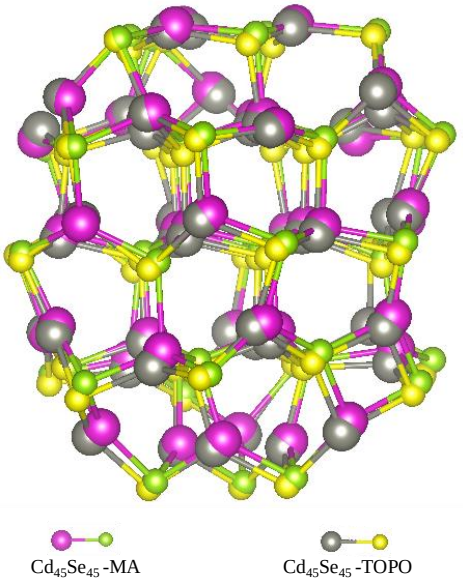

Figure 3.4: Comparison of optimized structure of $Cd_{45}Se_{45}$ with MA and TOPO passivants. Ligands are not shown here. Reprinted from ref. [86].

the one performed here, is only a snapshot of the true very dynamic situation where L-type ligands wiggle and presumably even interchange attachment sites [115]. The PH-passivated structures show almost no geometric relaxation and the HOMO and LUMO states are accordingly highly symmetric. The core \shell $Cd_{45}Se_{45}$\CdS-PH structure shows a *quasi* type-II character, where the hole is localized in the core and the electron over the entire structure.

3.2.1 Raman spectra

We deconvoluted the calculated Raman spectra of QDs into contributions from three distinct fragments of the QDs: ligands, the bulk-like core (Cd four-fold coordinated with Se and vice versa), and the surface (Cd atoms not four-fold coordinated with Se and vice versa). To understand how fragments of the QD contribute to the Raman spectra, we calculate the contributions from specific fragments (frag) of the structure to the Qth vibrational mode as:

$$c^{Q}_{\text{frag}} = \frac{\sum_{A\in\text{frag}} \sqrt{M_A}|R^{Q,\text{norm}}_A|^2}{\sum_{B}^{N_{\text{atom}}} \sqrt{M_B}|R^{Q,\text{norm}}_B|^2}, \tag{3.11}$$

where A and B are atom indices, $M_{A/B}$ is the mass of atom A/B, $R^{Q,\text{norm}}_{A/B}$ is the atomic displacement vector, which is normalized as $\sum_{B}^{N_{\text{atom}}} |R^{Q,\text{norm}}_B|^2 = 1$. c^{Q}_{frag} can take values

between 0 for no contribution from a given fragment to the vibrational mode and 1 for 100% contribution. Further, we study the degree of localization for vibrational modes by calculating the inverse participation ratio (IPR) [116]. The IPR ranges from 1 if all atoms contribute equally to the vibrational mode to $1/N_{\text{atom}}$ if only a single atom contributes. The IPR for the Qth mode can be calculated from c_A^Q to the overall phonon mode and the number of atoms in the structure, N_{atom}, as follows:

$$\text{IPR}^Q = \frac{1}{N_{\text{atom}} \sum_A^{N_{\text{atom}}} \left(c_A^Q\right)^2}. \tag{3.12}$$

The calculated Raman spectra are shown in Fig.3.5, for the $Cd_{13}Se_{13}$-MA, $Cd_{33}Se_{33}$-MA and $Cd_{45}Se_{45}$-MA structures. The top panels (a-c) are plotted using a Gaussian broadening of 23.5 cm^{-1}, while the bottom panels (d-f) show unbroadened results. We use two types of analysis of the signal, on the top, we discriminate surface/ligand/core contributions according to Eq. 3.11 and on the bottom, we use the inverse participation ratio (IPR) [116] from Eq. 3.12. A low value of IPR (red color) signifies localized

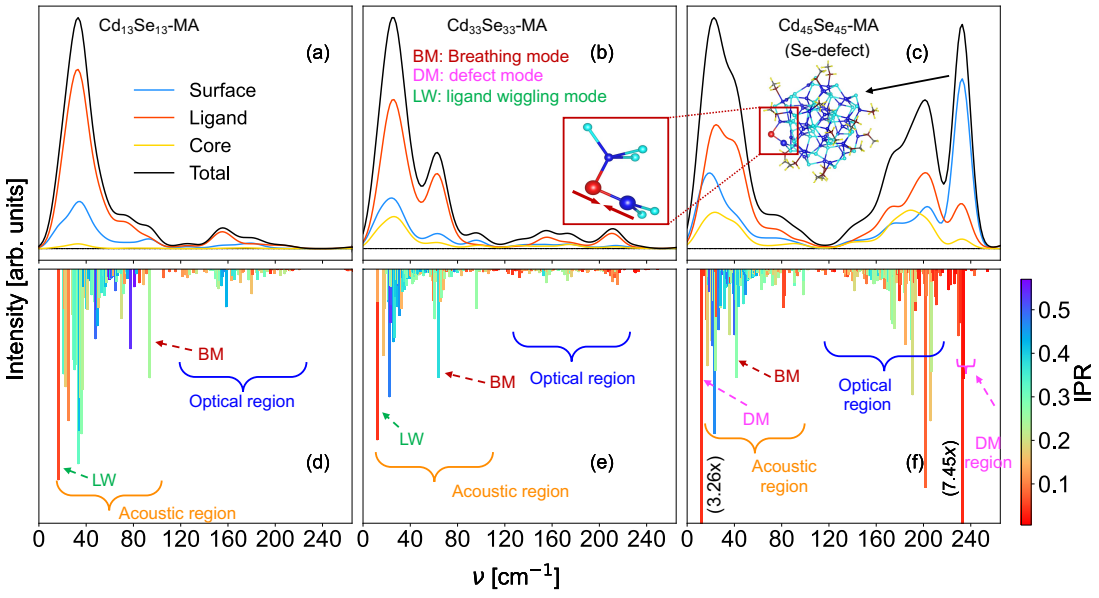

Figure 3.5: Calculated Raman spectra of (a,d) $Cd_{13}Se_{13}$-MA, (b,e) $Cd_{33}Se_{33}$-MA, (c,f) $Cd_{45}Se_{45}$-MA using a Gaussian broadening of 23.5 cm^{-1} (solid lines upper panels, a-c), and without broadening (bars on the lower panels, d-f). The broadened results are analyzed in terms of the three fragments: ligand, surface, and core (Eq. (3.11)). The bars (lower panels) are colored according to the IPR value (Eq. 3.12). The inset in (c) shows the QD highlighting the defect and the inset in (b) shows the vibrational eigenmode of the defect vibration at 233 cm^{-1}. Reprinted from ref. [86].

vibrations. For the lower panels, we have normalized the intensities according to the breathing mode, which is easy to identify. While this specific normalization is debatable, it is at least rather simple to comprehend. We focus on the region below 250 cm^{-1}, so that intra-ligand vibrations, typically upto around 3000 cm^{-1} [60], are not presented. The calculated Raman spectra presented here correspond to a simulated temperature of 298.15 Kelvin (room temperature).

As common for semiconductors, the vibrations can be divided into an acoustic and an optical region, as indicated in the lower panels of Fig.3.5. We notice that for the smaller magic size clusters the optical region is nearly Raman-inactive, so that dominant contributions originate from acoustic-type modes. The optical region becomes active already for the slightly larger $Cd_{45}Se_{45}$-MA structure. It is known that the LO-peak strongly dominates for larger, bulk-like, structures [88, 89, 90] and the emergence of the LO peak with QD size was investigated earlier [5]. We see in Fig.3.5c) that the rise of the optical region correlates with the emergence of modes with significant core characters (yellow line).

Generally, we see that many vibrations are, to a certain extent, Raman active, which makes a meaningful and concise analysis difficult. However, we can identify a few distinctive modes. The breathing modes (BM in Fig. 3.5d-f, see [117] for vibration movie) show the qualitative frequency shift we would expect from the Lamb model [91], i.e., to the red when the size increases: 93.86 cm^{-1}, 63.66 cm^{-1} and 41.53 cm^{-1} for $Cd_{13}Se_{13}$-MA, $Cd_{33}Se_{33}$-MA, $Cd_{45}Se_{45}$-MA, respectively. One further mode which strikes by its low IPR value (strong localization) and strong intensity is labeled as LW in Fig. 3.5d-f). It corresponds to a wiggling motion of the entire MA ligand molecule (see [117] for vibration movie). This vibration will most likely be hindered in a realistic setup including solvents and we highlight it here to point out possible pitfalls in the raw computational results.

Our most interesting result is the appearance of very intense defect-related peaks in the low (11.93 cm^{-1}) and the high-frequency regions (229.5, 231.1, and 232.99 cm^{-1}) of $Cd_{45}Se_{45}$-MA spectra (marked DM in Fig. 3.5f)). Each of the three Se defects produces one high-frequency Raman peak, while we could identify only one low-frequency defect-related peak. This low-frequency mode corresponds to the wagging vibration of the two-fold coordinated Se defect, where the Se moves perpendicular to the Cd-Se-Cd plane. The nature of the high-frequency mode is shown in the inset of Fig. 3.5b). The Se and the threefold coordinated Cd undergo a stretching vibration, which is

knowably strongly Raman active. The other Se-Cd bond (towards the threefold Cd) accommodates the stretching but with a very small bond-length change (see [117] for vibration movie).

It is noteworthy to mention that the threefold coordinated Cd atoms, present at the surface of all our structures, reconstructed into a planar geometry with high symmetry. The localized vibrations in these regions exhibit a symmetric, Raman-inactive character.

As a next step we will investigate the influence of the surface on the Raman intensity and show in Fig. 3.6 results for the same size QD, but with different terminations. Fig. 3.6d,h) is a repetition of Fig. 3.5c,f) and is used here again for ease of comparison.

The simplest structure is $Cd_{45}Se_{45}$-PH which has an idealized passivization and high symmetry. As expected, none of the defect features previously mentioned are present. The breathing mode at 55 cm^{-1} is the most intense, with a high IPR value indicating that many atoms vibrate collectively, as expected from a breathing mode in high symmetry. These types of modes are strongly Raman active. We also notice only very weak intensities in the optical region and it seems that lower symmetry (realistic surfaces) leads to an activation of the optical region already at smaller sizes.

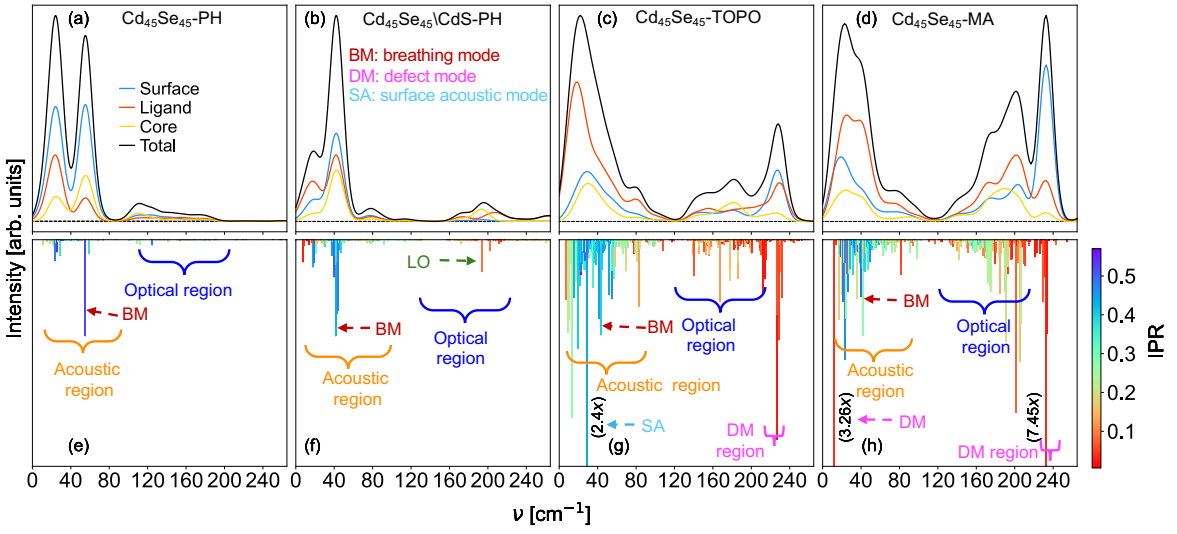

Figure 3.6: Similar to Fig. 3.5 but depicting $Cd_{45}Se_{45}$-PH (a,e) , $Cd_{45}Se_{45}$\CdS-PH (b,f), $Cd_{45}Se_{45}$-TOPO (c,g), and $Cd_{45}Se_{45}$-MA (d,h). Reprinted from ref. [86].

Covering the QD with a shell of CdS leads to the $Cd_{45}Se_{45}$\CdS-PH core-shell structure shown in Fig. 3.2b,f). The breathing mode still dominates, at a somewhat lower frequency of 41.8 cm^{-1}, following the larger size of the structure. The LO peak starts to appear at 194 cm^{-1} for the CdSe core. Movies of all vibrational modes can

be accessed in [117]. The optical region of the CdS shell appears at around 280 cm^{-1} and is presented in the appendix.

While both, the idealized passivated and the core-shell structures lead to the absence of defect peaks, the TOPO-covered structure shown in Fig. 3.6(c,g) resembles the one of the MA passivated structure. The breathing mode for TOPO and MA terminated structures have similar frequencies (43.39 cm^{-1} and 41.53 cm^{-1} respectively) and have in both cases significant intensities.

The optical region is somewhat more intense in the case of the MA terminated structure. Although the L-type ligands bind only very weakly to the surface Cd atoms, they have an influence on the Raman activity. In the case of TOPO oxygen binds to Cd, while it is nitrogen for MA. Also, the structure is affected by the type of ligand, although to a relatively low extent, as compared in Fig. 3.4. For $Cd_{45}Se_{45}$-TOPO, we observe the high-frequency defect peaks we described for $Cd_{45}Se_{45}$-MA but do not observe the low-frequency DM peak, which hints at a strong surface dependence of this specific vibration. We find, however, a vibration of acoustic character that is rather delocalized over a large part of the surface (on one "facet") and indicated it with SA for surface acoustic [91] in Fig. 3.6(g).

One further piece of information can be extracted from the calculations w.r.t. the defect peaks. The vibrational frequencies of the three peaks corresponding to the three defects are slightly split: 227.1 cm^{-1}, 227.2 cm^{-1}, and 228.5 cm^{-1} for TOPO; 229.5 cm^{-1}, 231.1 cm^{-1}, and 232.99 cm^{-1} for MA; and have significantly different intensities. We notice that the splitting in vibrational frequencies corresponds to the splitting in the DMO energies in the sense that we obtain large splittings in eigenvalues (263 meV) and frequencies (3.49 cm^{-1}) for MA and small splittings in eigenvalues (32 meV) and frequencies for (1.4 cm^{-1}) TOPO. We described this earlier as symmetry inequivalent Se-defects. If we look at the bond length on one and the other side of the twofold coordinated Se defect we notice that the strongest Raman intensity occurs for the situation where the imbalance is the greatest. In other words, the Raman intensities seem to be correlated to the difference in the Se-Cd bond lengths. Our largest difference is 0.039 Å (2.517 Å vs. 2.556 Å) for the defect with the largest Raman intensity at 232.99 cm^{-1} in $Cd_{45}Se_{45}$-MA. In Table 3.1, we present the bond lengths for all three Se-defects attached to a threefold-coordinated Cd on one side and a fourfold-coordinated Cd on the other, for both $Cd_{45}Se_{45}$-MA and $Cd_{45}Se_{45}$-TOPO structures.

Coordination	3-fold Cd	4-fold Cd
MA	2.517	2.547
	2.517	2.556
	2.542	2.565
TOPO	2.528	2.544
	2.528	2.544
	2.529	2.543

Table 3.1: Bond length (in Å) of three Se-defects in $Cd_{45}Se_{45}$-MA and $Cd_{45}Se_{45}$-TOPO structures

We finally compare our results with the experimentally measured spectra reported by Badlyan et al. [46], and reproduced in Fig.3.7. The authors reported a high-frequency shoulder (HFS), shown in magenta, above the optical region around 233 cm^{-1} in pure CdSe QDs, which is shown to disappear upon the growth of a CdS shell. This makes their data particularly relevant for direct comparison with our results. A similar HFS has been observed in QDs of different sizes, ranging from 1.44 nm to 3.4 nm [44, 51, 53, 45, 55].

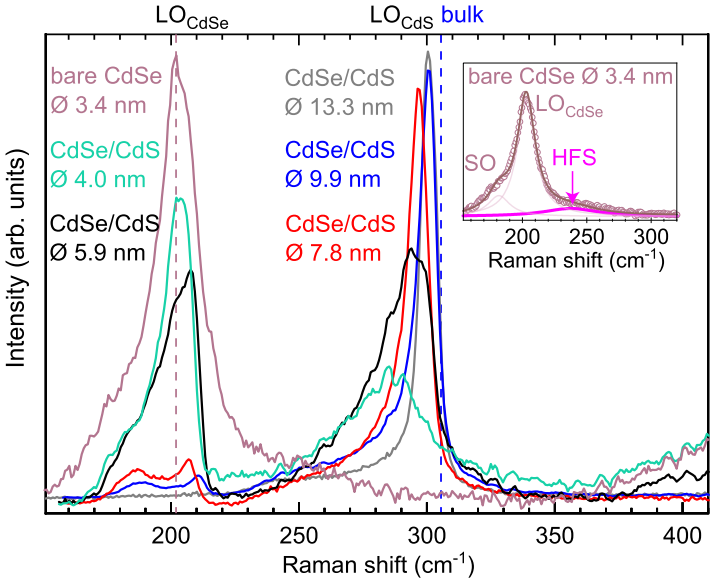

Figure 3.7: Measured Raman spectra of CdSe dots with HFS (shown in magenta) reproduced with permission from ref. [46](Copyright (2019) by the American Physical Society). Similar HFS has been measured in other experiments. [44, 51, 53, 45, 55]

Our calculated defect peaks, located above the optical region (228 cm^{-1} for TOPO and 233 cm^{-1} for MA), coincide with the experimentally observed HFS. Additionally,

our calculations for the core-shell structure do not exhibit this peak, which is consistent with the experimental findings. However, in the experimental data, the high-frequency shoulder (HFS) is relatively weak compared to the signals from the optical region, which is in contrast to our calculations. We attribute this discrepancy to two main factors. First, the size differences between the QDs in the experiments and our calculations certainly play a significant role, especially in the intensity of the LO peak. Our QD sizes only allow for a glimpse at the LO peak that is known to become very dominant as size increases. Second, it is most likely that not all the QDs in the experimental sample are defective, which would naturally lead to a weaker defect peak.

In conclusion, we identify, via state-of-the-art *ab initio* DFT on small CdSe QDs with various realistic surface passivations, an intense Raman signal at approximately 230 cm^{-1}, corresponding precisely to the frequency where the debated HFS is experimentally measured. This signal corresponds to the stretching vibration of a defective twofold coordinated Se atom. The Se atom is bonded to two inequivalent Cd atoms, one being threefold and the other fourfold coordinated. We observe that the inequivalence of the two bonds leads to the asymmetric geometry and the very intense Raman signal. The placement and the type of L-type ligands (TOPO or MA) influence this inequivalence and hence the intensity of the signal. However, the signal persists with significant intensity in all scenarios.

To compare with experimental observations, which reported the disappearance of the HFS after the growth of a protective shell, we constructed a core/shell structure and observed the same phenomenon. Accordingly, the signal disappears in defect-free (magic size cluster) structures, making it a distinctive marker for identifying defective versus non-defective structures. More generally, we observe that the Raman signal in the optical vibrational region is activated when realistic, partly reconstructed, L-type ligand-protected surfaces are considered. In contrast, QDs modeled with idealized passivation, and thus higher symmetry, exhibit comparatively weaker Raman signals in this spectral region.

Chapter 4

Excitonic fine structure in alloyed QDs and type-II dot-rod nanostructures

All the calculations and data analysis presented in this work were carried out by the author, **S. Kumar**, in collaboration with Nadine Tewonoue Djota.

Changing composition via control of constituent stoichiometry, i.e., alloying in nanostructures can provide desirable band gaps and properties. The alloys are formed by combining two differing energy gaps semiconductors. By adjusting the ratio of the constituents, the band gap can be precisely controlled [118]. Generally, increasing the concentration of the wider band gap semiconductor in the same size structure increases the band gap or vice versa. Building upon the compositional control, it is possible to achieve a finer manipulation of the band gap by creating core/shell (CS) heterostructures. This involves growing a shell of another semiconductor material around a core, which can be either pure or alloyed. This offers full control over the band gap and helps to control the tunability of energy levels and wavefunctions of different carriers for desirable applications.

CS nanostructures are heterostructures that can be classified into different categories depending on the band gaps and the relative position of the valence and conduction bands of the involved materials. Depending on the band offsets, electrons or holes can be confined within either material, be trapped at the interface, or even delocalize across the entire structure. Fig. 4.1 gives an overview of these different types of heterostructures. Three distinct cases based on band alignments are type-I, type-II, and *quasi*-type-II CS nanostructures. For the type-I (inverted type-I) CS case, electrons

and holes are both spatially localized in the core (shell), while type II has a spatial separation of the electron and hole. *Quasi*-type-II has one of the carriers spatially localized over the whole structure while the other carrier is spatially localized either in the core or the shell.

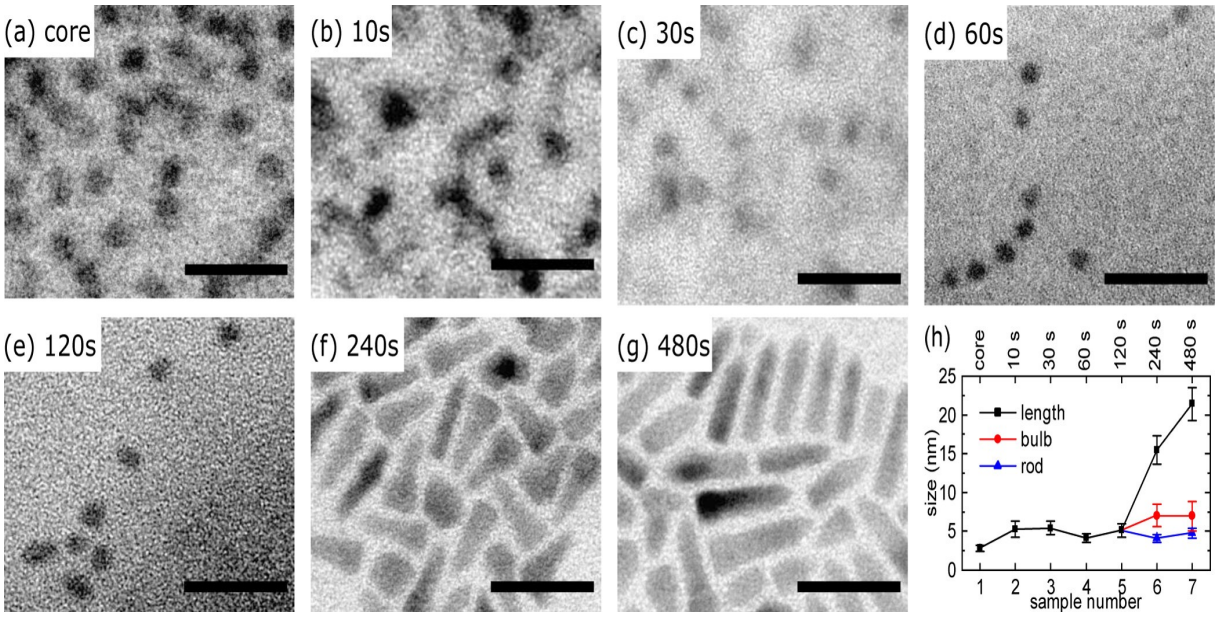

Figure 4.2: (a–g) Representative TEM images of (a) ZnSe core sample and (b–g) aliquots of the growth series, belonging to reaction times as noted. Scale bars: 25 nm. (h) Sizes of the length, rod diameter, and bulb diameter (if distinguishable) as determined by TEM vs the sample number. Lines connecting data points are guides to the eye. Reproduced from ref. [119].

Over the years, different alloyed and CS structures have been explored [120, 121, 122, 123, 124]. Recently, Rebmann and co-workers [119] have synthesized alloyed

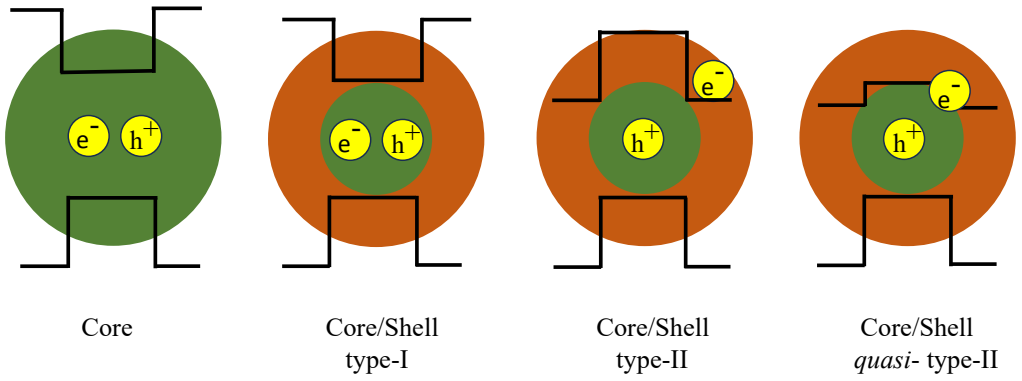

Figure 4.1: Schematic illustration of various QD types classified by relative charge carrier localization.

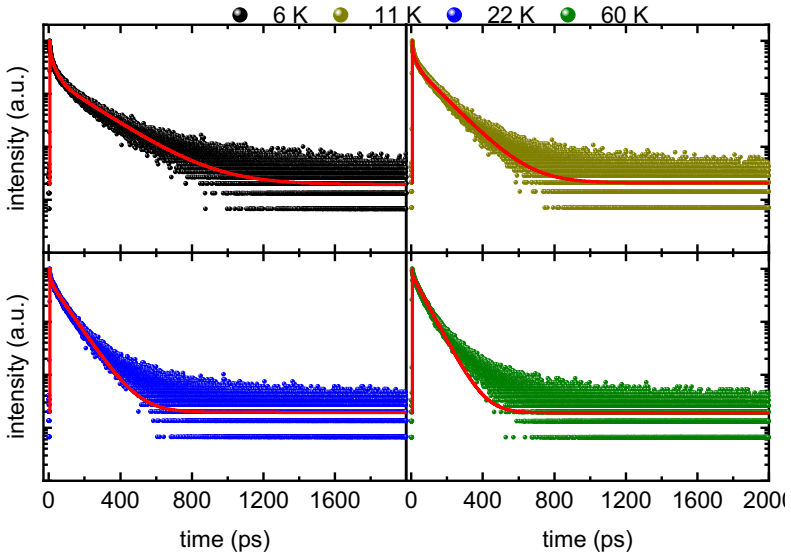

Figure 4.3: Temperature dependent PL decay of $Zn_{0.45}Cd_{0.55}Se$ alloyed dot in CdS rod sample shown in Fig. 4.2. Reproduced from the unpublished work of Hans Werners from the group of Prof. Mews at the University of Hamburg..

$Zn_{1-x}Cd_xSe$ (x is concentration) dots in CdS rod nanostructures. Fig. 4.2 shows the TEM images of their synthesized nanostructures. The synthesis starts with pure ZnSe dots, which undergo cation exchange to form the $Zn_{1-x}Cd_xSe$ dot, followed by the growth of a CdS shell. The final core-shell nanostructures have two variations: one with a $Zn_{0.45}Cd_{.55}Se$ dots and another with a $Zn_{0.55}Cd_{.45}Se$ dot (sample 7 in Fig. 4.2). Fig. 4.3 presents the photoluminescence (PL) decay curve measured on $Zn_{0.45}Cd_{.55}Se$ dots in CdS rod shell structures at various low temperatures (ranging from 6 Kelvin to 60 Kelvin). The behavior of PL decay in semiconductor nanostructures is determined by the material's excitonic fine structure (shown in Fig. 4.4) and commonly interpreted using a simplified three-level decay model [125, 36, 126, 127]. This decay model includes an optically allowed bright state, an optically forbidden dark state, and the ground state. This three-level model is derived from highly symmetric spherical dots (shown in Fig. 4.4) and is generally adopted for different nanostructures [127, 128, 129]. However, the measured PL decay curves for these structures show a multi-exponential character at lower temperatures and, as the temperature increases, the decay behavior simplifies to a bi-exponential character due to thermal energy (k_BT i.e. product of the Boltzmann constant, k_B, and the temperature, T) exceed the exciton level splittings. Therefore, a simplified three-level model will not be able to explain the multi-exponential nature of PL decay at lower temperatures. Apart from that, creating alloys in nanostructures

can introduce strain due to lattice mismatch. This lattice mismatch can change the energy levels and spatial distribution of electron and hole wavefunctions. Similarly, core/shell nanostructures can have different localization of charge carriers depending on the specific structure. For example, in type-I CS heterostructures, the electron and hole wavefunctions overlap significantly. In contrast, type-II CS heterostructures have spatially separated wavefunctions. This spatial separation significantly affects the exchange interaction and the excitonic fine structure, which has not been considered in a simplified three-level model.

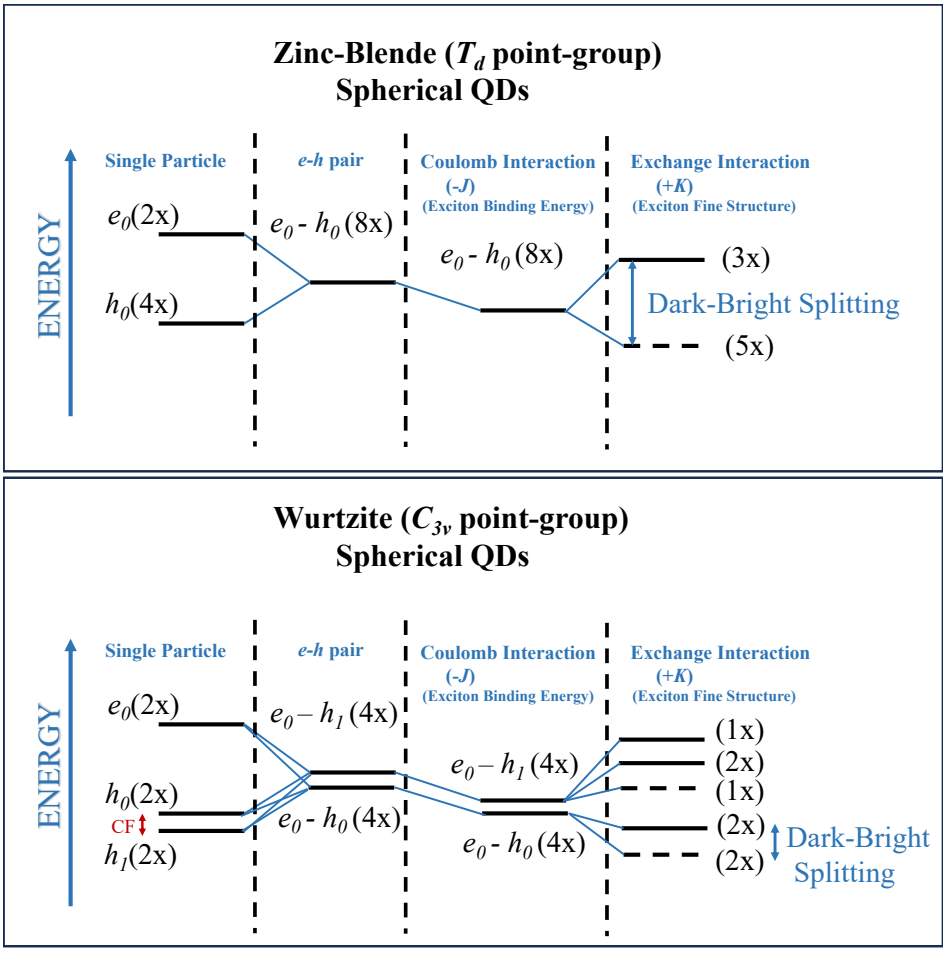

Figure 4.4: Schematic representation of the exciton FS formation from the ground state electron (e_0, unoccupied) and hole (h_0, h_1 occupied) states (SO coupling included) for ZB and WZ spherical nanocrystals. Optically passive dark states are shown with dashed lines while active bright states are plotted with solid lines. The dark-bright (DB) splitting is a difference in energy between the lowest dark and lowest bright exciton state. The degree of degeneracy is given in parentheses next to the state label.

4.1 Excitonic fine structure

Excitonic fine structure (FS) is a direct consequence of electron and hole spins. When an exciton originates from the same Kramer's doublet (a pair of states differing only in spin) of the electron and hole, their combined spin states can lead to four unique configurations: $|e\uparrow h\uparrow\rangle$, $|e\uparrow h\downarrow\rangle$, $|e\downarrow h\uparrow\rangle$, $|e\downarrow h\downarrow\rangle$. The spin-dependent electron-hole exchange interaction Hamiltonian, $\hat{H}_{exch}$, takes on different forms due to the varied pseudo-spin wavefunctions associated with each exciton state.

Therefore, these distinct pseudo-spin basis states lead to the splitting of these exciton states, known as exciton fine structure (FS). The fine structure consists of optically allowed (bright) and forbidden (dark) states. The splitting of the lowest bright and the upper dark states is called dark-bright (DB) splitting. FS splitting is an atomistic effect and is strongly dependent on crystal symmetries as well as the symmetry of the wavefunctions.

The lowest exciton FS formation for spherical QDs with ZB and WZ crystal structure is shown schematically in Fig. 4.4. The SP eigenstates of the lowest unoccupied orbitals (e_0) and the highest occupied orbitals (h_0 and h_1) create the band-edge excitonic states. In the WZ structure (C_{3v} symmetry), the lower symmetry compared to the ZB structure (T_d symmetry) lifts the degeneracy of the SP states h_0 and h_1, resulting in crystal field (CF) splitting. In the absence of Coulomb and exchange interaction, electron-hole (e-h) pairs are simple products of the SP states which can be four- or eight-fold degenerate, depending on the crystal structure. The addition of Coulomb interaction only lowers the energy of e-h pair without lifting its degeneracy. However, the addition of exchange interaction lifts the degeneracy, leading to exciton FS. The excitonic FS is highly dependent on the crystal structure. In the highly symmetric T_d structure, the excitonic states split into a lower-energy, five-fold degenerate, spin-forbidden (dark) state and a higher-energy, three-fold degenerate, spin-allowed (bright) state, highlighted in Fig 4.4.

Large DB splittings exceeding thermal energy can trap carriers in the lower-energy dark state, prohibiting efficient emission [126, 130, 36]. At low temperatures, the polarization properties of the emitted light from colloidal nanostructures are directly determined by the excitonic FS [131, 132, 133, 134, 135, 136]. Given the influence of alloying and core/shell growth on wavefunction localization and carrier interaction, it becomes crucially important to understand how these factors affect the excitonic fine

structure and their potential applications.

However, calculating FS is not straightforward as it needs a proper treatment of the crystal structure, the spin-orbit interaction (for qualitatively correct h_0, h_1 states), and the electron-hole exchange integrals. In the past, different atomistic approaches [61, 62, 63, 137, 138, 139, 140] have been used to calculate excitonic FS.

In this work, we use atomistic million-atom many-body pseudopotential calculations based on the empirical pseudopotential method in combination with screened configuration interaction. We calculate the excitonic FS of $Zn_{1-x}Cd_xSe$ (where x is concentration) alloyed dots of varying sizes, followed by an investigation of these dots within CdS rod heterostructures. We provide compelling evidence that the exciton fine structure in alloyed nanostructures shows qualitative differences compared to pure, highly symmetrical spherical dots. This observation challenges the limitations of the simplified three-level decay model typically used for describing PL decay.

4.2 Empirical Pseudopotential Method

The empirical pseudopotential method (EPM) is a computationally efficient tool to calculate the optical properties of materials [142, 61], particularly suitable for large systems containing millions of atoms. EPM bypasses the self-consistent solutions and ignores the oscillations of valence electrons in the core region to significantly reduce computational costs. Furthermore, standard DFT tends to underestimate the band gap quite significantly, which is an especially significant problem for spectroscopic properties. The construction of an empirical pseudopotential involves fitting the reciprocal space pseudopotential $V(\mathbf{G})$ to experimentally known quantities and therefore provides accurate results. The self-consistent effective pseudopotential of the crystal (V for crystal potentials and v for atomic potentials) conceivably written as a sum of atom-centered pseudopotentials:

$$V(\mathbf{r}) = \sum_{\alpha,j,n} v_\alpha(\mathbf{r} - \mathbf{R}_n - \mathbf{r}_{\alpha,j}), \tag{4.1}$$

where α is the atom type index, n being the index for the primitive unit cells, $\mathbf{R}_n$ is the corresponding lattice vector, and $\mathbf{r}_{\alpha,j}$ is basis vector in unit cell n for atom j of type α. For crystals with single atom type (e.g. Ge, Si), v, the potential in reciprocal

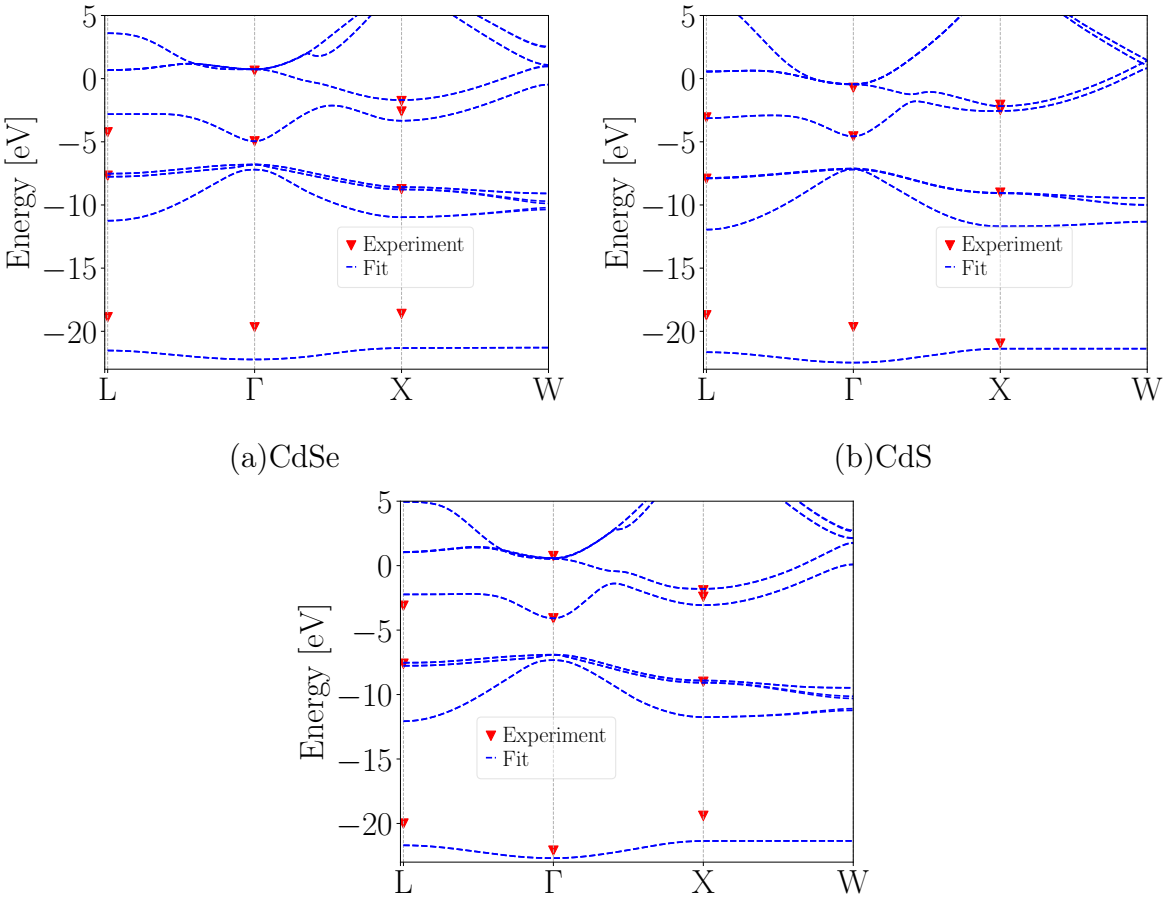

Figure 4.5: Calculated bulk band structures using the fitted empirical pseudopotential for (a) CdSe, (b) CdS, and (c) ZnSe. Red triangles are experimentally measured energy gaps at various high-symmetry points used in the EPM fitting. The experimental data is taken from refs. [141, 85] and references within.

space can be written as:

$$V(\mathbf{r}) = \sum_{\mathbf{G}} v(\mathbf{G}) S(\mathbf{G}) e^{i\mathbf{G}\cdot\mathbf{r}}, \tag{4.2}$$

or for the ZB structure as:

$$V(\mathbf{r}) = \sum_{\mathbf{G},\alpha} v_\alpha(\mathbf{G}) S_\alpha(\mathbf{G}) e^{i\mathbf{G}\cdot\mathbf{r}}, \tag{4.3}$$

with geometry-dependent structure factor S being:

$$S(\mathbf{G}) = \frac{1}{N} \sum_j e^{i\mathbf{G}\cdot\mathbf{r}_j}, \tag{4.4}$$

where N is the number of basis atoms. Potential $v(\boldsymbol{G})$ (form factor) is considered as a disposable parameter in EPM. EPM also allows us to fit the effective masses and the band gap simultaneously due to the rescaling of the kinetic energy for missing the non-local part [61]. Now, the SP Schrödinger equation can be solved as:

$$\widehat{\mathrm{H}}\psi_i(\mathbf{r}) = \left\{-\frac{\beta}{2}\nabla^2 + V_{\mathrm{loc},\alpha}^{\mathrm{EPM}}(\mathbf{r}) + \widehat{V}_{\alpha}^{\mathrm{SO}}(\mathbf{r})\right\}\psi_i(\mathbf{r}) = \epsilon_i\psi_i(\mathbf{r}). \tag{4.5}$$

where i denotes eigenstates and β is only used to rescale the kinetic energy term $-\nabla^2/2$ (in atomic units). $V_{\mathrm{loc}}^{\mathrm{EPM}}(r - r_\alpha)$, where $\mathbf{r} = r - r_\alpha$, is the local potential fitted to known experimental quantities for each atom type α and the spin-orbit interaction is included as [61]:

$$\hat{V}_{\alpha}^{\mathrm{SO}} = \sum_{l} |l\rangle V_{l,\alpha}^{\mathrm{SO}}(r - r_\alpha)\hat{\boldsymbol{L}}\cdot\hat{\boldsymbol{S}}\langle l|, \tag{4.6}$$

in which $|l\rangle$ is the projection operator of spatial angular momentum l.

Fig. 4.5 presents the calculated band structures of bulk CdSe, CdS, and ZnSe. These calculations were performed using a fitted empirical pseudopotential, which will be the basis for further calculations in this chapter.

4.2.1 Linear Combination of Bulk Bands (LCBB)

Solving the time-independent Schrödinger equation, Eq. (4.5), requires the selection of an initial form for the wavefunctions, often plane waves in DFT. Among various approaches, the LCBB method [143] stands out as a better choice, offering several advantages. By confining the basis states to a subset of physically relevant bands n and k-points (k), the LCBB method reduces computational complexity without compromising accuracy. Unlike conventional approaches that approximate the symmetry of the nanostructure based on its shape, this method maintains the system's full atomistic symmetry. This method can also include strain dependence in the basis set, the band as well as valley mixing in Hamiltonian. The LCBB wavefunctions are written in real

space as:

$$\psi(\mathbf{r},\sigma) = \sum_{n}^{N_B}\sum_{k}^{N_k} C^{\sigma}_{k,n}\phi^0_{k,n}(\mathbf{r}) \ , \tag{4.7}$$

$$\phi^0_{k,n}(\mathbf{r}) = \frac{1}{\sqrt{N}} u_{k,n}(\mathbf{r}) e^{i\mathbf{k}\cdot\mathbf{r}} \ , \tag{4.8}$$

$$u_{k,n}(\mathbf{r}) = \frac{1}{\sqrt{V_0}} \sum_{G}^{N_G} A_{k,n}(\mathbf{G}) e^{i\mathbf{G}\cdot\mathbf{r}} \ , \tag{4.9}$$

with $V_0 = a_0^3$ and $N = n_x n_y n_z$. Here, a_0 denotes the lattice constant of the material such that V_0 constitutes the volume of the primary cell. $n_{x,y,z}$ is the size of the supercell in each dimension x, y, z. $\phi^0_{k,n}(\mathbf{r})$ represents a Bloch function whose periodic part, $u_{k,n}(\mathbf{r})$, can be expanded in reciprocal space. The expansion coefficients $C^{\sigma}_{k,n}$ will be obtained after numerically diagonalizing the EPM Hamiltonian. σ accounts for the spin but this index will be omitted in the next sections as the spin has no incidence on the energies in the absence of magnetic field. The wavefunction can be expanded as:

$$\psi(\mathbf{r},\sigma) = \sum_{n}^{N_B}\sum_{k}^{N_k} C^{\sigma}_{k,n} \frac{1}{\sqrt{N}} \left[\frac{1}{\sqrt{V_0}} \sum_{G}^{N_G} A_{k,n}(\mathbf{G}) e^{i\mathbf{G}\cdot\mathbf{r}} \right] e^{i\mathbf{k}\cdot\mathbf{r}}, \tag{4.10}$$

such that the Bloch basis states are written:

$$\phi^0_{k,n}(\mathbf{r}) = \frac{1}{\sqrt{\Omega_0}} \sum_{G}^{N_G} A_{k,n}(\mathbf{G}) e^{i(\mathbf{G}+\mathbf{k})\cdot\mathbf{r}}, \tag{4.11}$$

where $\Omega_0 \equiv V N_0$ is the volume of the supercell. In Dirac bra-ket notation, this basis state can be rewritten as:

$$\langle \mathbf{r}|\phi^0_{k,n}\rangle = \frac{1}{\sqrt{\Omega_0}} \sum_{G}^{N_G} A_{k,n}(\mathbf{G}) \langle \mathbf{r}|\mathbf{k}+\mathbf{G}\rangle, \tag{4.12}$$

where we have defined

$$\langle \mathbf{r}|\phi^0_{k,n}\rangle = \phi^0_{k,n}(\mathbf{r}), \tag{4.13}$$

$$\langle \mathbf{r}|\mathbf{k}+\mathbf{G}\rangle = e^{i(\mathbf{k}+\mathbf{G})\cdot\mathbf{r}}, \tag{4.14}$$

and finally:

$$|\phi^0_{k,n}\rangle = \frac{1}{\sqrt{\Omega_0}} \sum_G^{N_G} A_{k,n}(\mathbf{G})|\mathbf{k}+\mathbf{G}\rangle. \tag{4.15}$$

Formally, we have removed the r-dependence of the Bloch states which is useful to understand the derivation of the matrix elements of the Hamiltonian both in the unstrained and strained cases. The equation that we want to solve is the following:

$$\left[\frac{-\beta}{2}\nabla^2 + \sum_\alpha \left(W_\alpha(\mathbf{k})\hat{v}_\alpha(\mathbf{r}-\mathbf{k}_\alpha - d_\alpha(\mathbf{R})) + \hat{V}^{SO}_\alpha\right)\right]\psi_j(\mathbf{r}) = E_j\psi_j(\mathbf{r}). \tag{4.16}$$

The weight function $W_\alpha(\mathbf{R})$ is used to denote whether an atom of type α occupies site $\mathbf{R}+d_\alpha(\mathbf{R})$. The atomic positions $\{\mathbf{R}+d_\alpha(\mathbf{R})\}$ are deviated from their "ideal" positions $d_\alpha(\mathbf{R})$ (e.g., perfect ZB crystal structure) to minimize the strain energy. For strain-dependent pseudopotentials, $W_\alpha(\mathbf{R})$ could deviate from 0 or 1, being instead a function of local strain.

4.3 Calculation of equilibrium atomic positions via valence force field method (VFF)

For heterogeneous structures, lattice constant mismatch plays a crucial role in modifying their electronic and optical properties. In real experimental structures, the energy is always minimized. For our simulated crystal structures, artificially cut from the ideal ZB configuration, minimizing strain energy through structural relaxation is therefore crucial. While *ab initio* methods offer better accuracy, they are limited to up to 1000 atoms. The Keating valence force field (VFF) model [144] offers a computationally efficient alternative for atomic relaxation. Here, relaxing the atomic positions with the VFF Hamiltonian includes bond stretching, bond-angle bending, and bond-length/bond-angle interactions. The inclusion of higher-order bond-stretching terms ensures a correct dependence of Young's modulus on the pressure as well as an accurate representation of the C_{11}, C_{12}, and C_{44} elastic constants in a ZB bulk material [145].

The total VFF energy E_{VFF} is given by:

$$\begin{aligned} E_{VFF} = & \sum_i \sum_j^{nn_i} \frac{3}{8}[\alpha_{ij}^{(1)} \Delta d_{ij}^2 + \alpha_{ij}^{(2)} \Delta d_{ij}^3] \\ & + \sum_i \sum_{k>j}^{nn_i} \frac{3\beta_{ijk}}{8 d_{ij}^0 d_{ik}^0} [(\mathbf{R}_j - \mathbf{R}_i) \cdot (\mathbf{R}_k - \mathbf{R}_i) - \cos\theta_{jik}^0 d_{ij}^0 d_{ik}^0]^2 \\ & + \sum_i \sum_{k>j}^{nn_i} \frac{3\sigma_{ijk}}{d_{ik}^0} \Delta d_{ij} [(\mathbf{R}_j - \mathbf{R}_i) \cdot (\mathbf{R}_k - \mathbf{R}_i) - \cos\theta_{ijk}^0 d_{ij}^0 d_{ik}^0], \end{aligned} \tag{4.17}$$

with $\Delta d_{ij} = [(R_i - R_j)^2 - d_{ij}^{0^2}]/d_{ij}^0$. Here $\mathbf{R}_i$ is the position of atom i, d_{ij}^0 is the ideal bond distance between atom types i and j and θ_{jik}^0 is the ideal angle of the bonds $j-i-k$. The $\sum^{nn_i}$ denotes the summation over the nearest neighbors of atom i. To calculate the bond stretching, bond-angle bending and bond-length/bond-angle interaction coefficients $\alpha_{ij}^{(1)}(\equiv \alpha)$, $\beta_{ijk}(\equiv \beta)$ and $\sigma_{ijk}(\equiv \sigma)$ the elastic constants of a bulk ZB structure can be used [146]:

$$C_{11} + 2C_{12} = \frac{\sqrt{3}}{4d_0}(3\alpha + \beta - 6\sigma), \tag{4.18}$$

$$C_{11} - C_{12} = \frac{\sqrt{3}}{d_0}\beta, \tag{4.19}$$

$$C_{44} = \frac{\sqrt{3}}{d_0}\frac{\alpha\beta - \sigma^2}{\alpha + \beta + 2\sigma}. \tag{4.20}$$

The second-order bond stretching coefficient $\alpha^{(2)}$ is related to Young's modulus by the pressure derivative $\frac{dB}{dP}$, while Young's modulus is $B = (C_{11} + 2C_{12}/3)$. All elastic constants used are summarised in Tab. 4.1. After strain energy minimization, the new relaxed atomic positions are used in the SP calculations.

Material	C_{11}	C_{12}	C_{44}	Ref.
CdSe	74.6	46.1	13.17	[141]
CdS	77.0	53.90	23.6	[147]
ZnSe	90.3	53.6	39.4	[141]

Table 4.1: Elastic constants (in GPa) of bulk materials considered in this work for VFF relaxation.

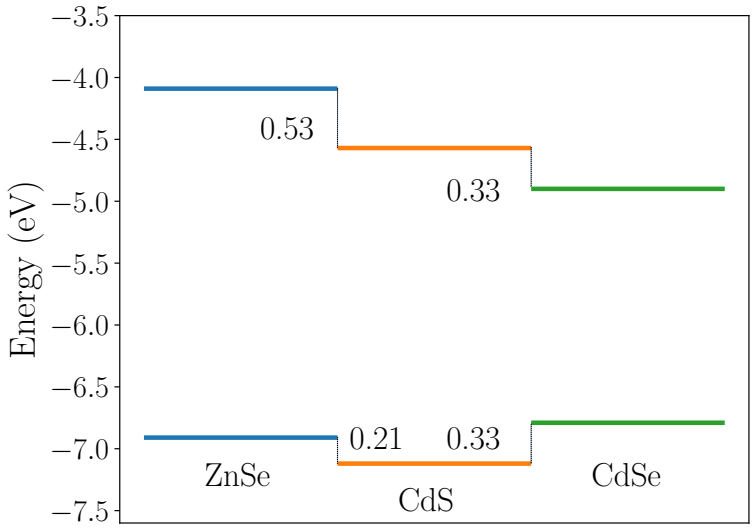

Figure 4.6: Schematic illustration of the relative band alignment for bulk ZnSe, CdS, and CdSe, showing conduction and valence band offsets. The experimental data is taken from refs. [141, 85] and references within.

4.4 Embedding in high gap artificial material

In the experiments, synthesized structures are capped with ligands. In our theoretical simulations, nanostructures are cut out from the bulk structure, and surface atoms remains unpassivated. These dangling bonds or unpassivated surface bonds can create electronically active traps and need to be removed. For theoretical calculations, simplified ways to mimic ligands are usually models like pseudo-hydrogen [148] or parameterized ligand potential of a Gaussian form [149]. Such artificial passivation removes the trap or the surface states from the band gap. For the work discussed in this chapter, we embed our structure in an artificial material with a large band gap to remove dangling bond states. The EPM of this material was fitted with a lattice constant of 6.052 Å. The artificial material is considered very fragile (or soft) so that it does not create an artificial strain in the structure and therefore the choice of lattice parameter of the artificial barrier is arbitrary. The fake barrier is fitted with a band gap of 8 eV to ensure enough confinement.

4.5 Results and Discussion

In this chapter, we investigate materials with ZB crystal structure for bulk, as well as QDs and dot-in-rod heterostructures. The experimental bulk lattice constants, band

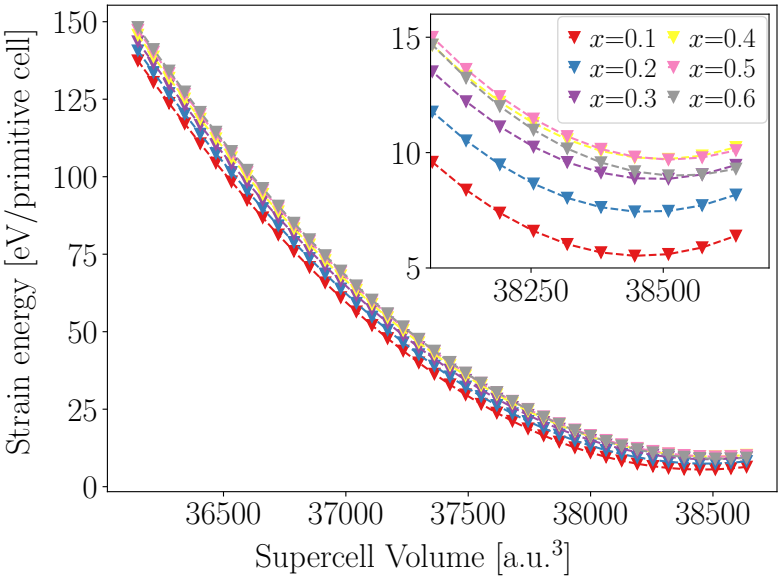

Figure 4.7: Strain energy dependence on supercell volume for $Zn_{1-x}Cd_xSe$ dots (3.2 nm diameter) with varying concentration (x). The supercell dimensions are $15\times15\times15\times a_0$, where a_0 is the lattice constant, which is varied from ZnSe to CdSe bulk values. The inset shows a magnified view around the minimum strain energy.

gaps, and spin-orbit splitting Δ_{SO} of CdSe, CdS, and ZnSe are summarized in Table 4.2. Fig. 4.6 then illustrates the relative band alignment for these bulk materials. To explore the influence of size and composition, alloyed QDs were studied with diameters between 3.2 nm and 6.1 nm. For each dot size, the alloy composition (x) was varied in steps of 0.1. We investigated dot-in-rod heterostructures consisting of an alloyed core QD (3.2 nm diameter) with varying Zn composition (45% and 55%). The surrounding rod has a diameter of 7 nm and a length of 27.7 nm as synthesized in experiments [119].

After embedding the structure in the artificial barrier material, we proceed to minimize the strain energy using VFF (see sec. 4.3). A significant challenge arises due to the lattice constant mismatch between ZnSe, CdSe, and the surrounding material (fake barrier). This mismatch makes it difficult to select the optimal lattice parameter for the supercell containing the embedded material. Since this choice can impact

Material	Band gap [eV]	Lattice constant [Å]	spin-orbit splitting Δ_{SO} [eV]
CdSe	1.82	6.052	0.41
ZnSe	2.82	5.668	0.42
CdS	2.55	5.818	0.07

Table 4.2: Experimental parameters for bulk CdSe, ZnSe, and CdS taken from ref. [141].

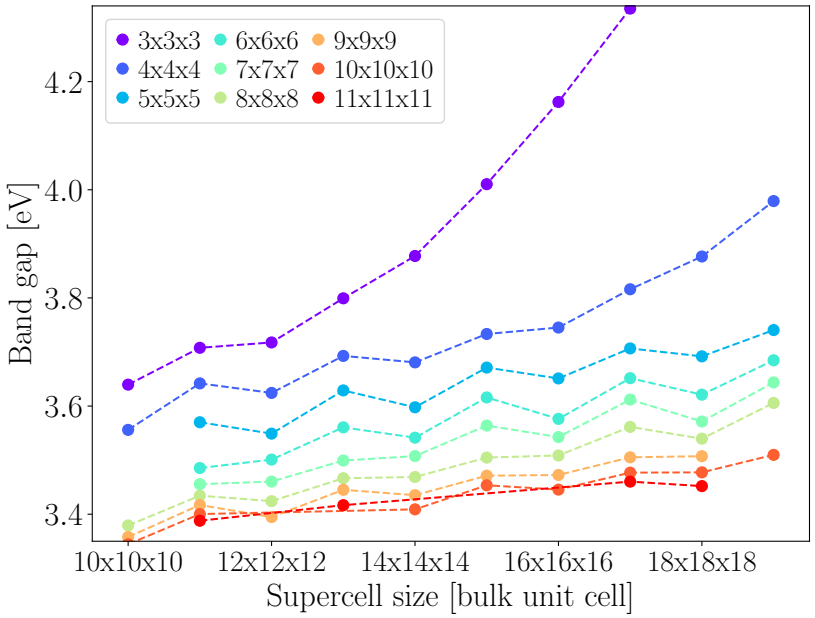

Figure 4.8: SP band gap dependence on different supercell sizes and k-point grids for a 3.2 nm $Zn_{0.9}Cd_{0.1}Se$ alloyed dot.

the accuracy of our calculations, we have minimized the strain energy as a function of supercell volume. We have systematically varied the supercell size, ranging from n_x x n_y x n_z unit cells (where n_i with $i \in \{x, y, z\}$ represents the number of unit cells along each direction) with the smallest bulk lattice constant (5.668 Å for ZnSe) to the largest (6.052 Å for CdSe). By minimizing the strain energy within this range of supercell sizes, we aimed to find a compromise that best accommodates the different lattice constants and minimizes the impact on the calculations. Fig. 4.7 shows the calculated strain energy as a function of supercell volume for 3.2 nm $Zn_{1-x}Cd_xSe$ alloyed dots with varying alloy compositions (x). The supercell size used is 15x15x15 unit cells which was obtained after the convergence of the SP energy band gap as discussed in the next step. The plotted results show two key findings: (i) The relaxed supercell size leans towards a lattice parameter closer to the larger bulk lattice constant (CdSe). (ii) For each alloy composition (x), the minimum value of the strain energy is at a slightly different lattice constant (or volume), indicating that every single structure has to be strain-minimized. While the strain-minimization procedure outlined above applies to all structures studied in this chapter, including dot-in-rod nanostructures, the strain profiles for these additional structures are omitted here for conciseness.

In the next step, we focus on finding optimal n_x x n_y x n_z unit cells in the supercell and k-point sampling in our calculations. In Fig. 4.8, we present the calculated band

gap of a 3.2 nm $Zn_{0.9}Cd_{0.1}Se$ dot as a function of the number of unit cells along each direction (n_x, n_y, n_z) within the supercell. The different colors correspond to calculations performed with varying k-point grids. For a fixed supercell size, the band gap has a stronger dependence on the k-point grid density. For example, the band gap significantly changes when the k-point grid is increased from 3x3x3 to 10x10x10. Typically, the convergence of the band gap w.r.t. the k-point grid is achieved around an 8x8x8 grid. In comparison, increasing the supercell size typically leads to a smaller change in the band gap, on the order of 0.2 eV for a converged k-grid. In contrast, increasing the supercell size has a comparatively weaker effect on the band gap for a converged k-point 8x8x8 or above grid. While the band gap shows some degree of convergence with respect to both the k-point grid and supercell size, it appears to be a slow process. This necessitates a careful selection of these parameters to achieve a balance between accuracy and computational cost. As observed in the figure, increasing the supercell size from 15x15x15 to 18x18x18 with a corresponding increase in k-point grid density (8x8x8 to 10x10x10) only leads to a band gap change of around 50 meV. In light of the observed slow convergence of the band gap with respect to supercell size and k-point grid, we opted for a compromise that balances accuracy and computational efficiency. Therefore, a supercell size of 15x15x15 bulk unit cells and a k-point grid of 8x8x8 was chosen for the calculations of the alloyed QDs, and a similar convergence procedure was extended for dot-in-rod nanostructure but not shown here.

4.5.1 Single-particle results

In this section, we study the influence of alloying on SP states. We investigate both bulk $Zn_{1-x}Cd_xSe$ alloys and the spherical alloyed QDs. We analyze how the alloy composition (x) affects the relative positions of the VBM (HOMO) and the CBM (LUMO). Subsequently, we discuss the further effects of alloying on the degeneracy of various electronic levels. Following the analysis of bulk and spherical dots, we examine the SP electronic states in dot-in-rod nanostructures.

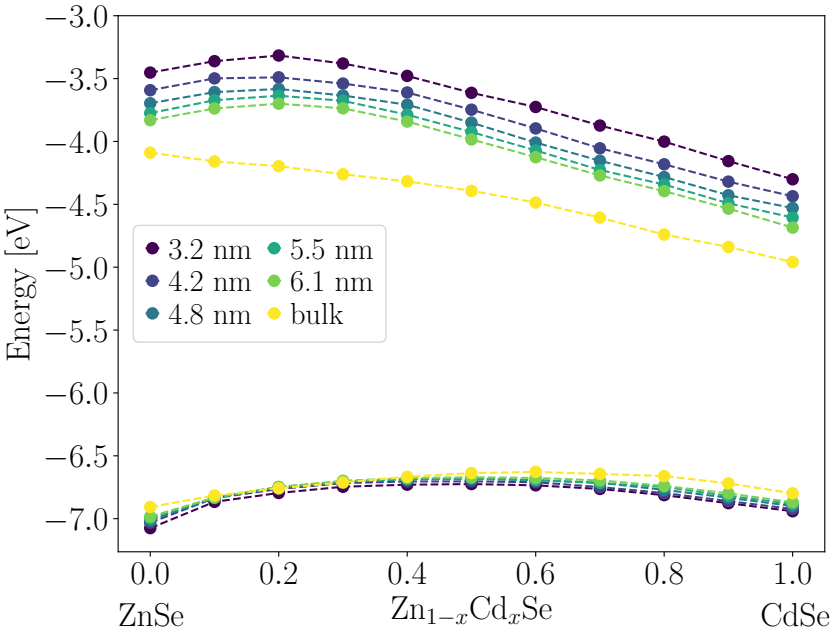

Figure 4.9: SP band gap dependence on alloy composition (x) in bulk and dots of different sizes.

4.5.1.1 Alloyed QDs

In Fig. 4.9, we show the calculated energies of the VBM (HOMO) and CBM (LUMO) for $Zn_{1-x}Cd_xSe$ alloys at the SP level. These SP states are shown for both bulk material and QDs with varying diameters, as the alloy composition x changes. The alloy composition (x) is varied from 0 (pure ZnSe) to 1 (pure CdSe) in steps of 0.1. Fig. 4.9 shows the expected band gap increase for a given x on going from bulk to 3.2 nm dot due to stronger confinement. However with the varying alloy composition x, the VBM and CBM, hence the band gap, deviate from a simple linear behavior for bulk (shown in yellow). Similar non-linear behavior is observed for the HOMO and LUMO levels in the QDs. This deviation from linearity is well-known in alloys and is called band gap bowing [150]. Interestingly, in our case, the band gap bowing becomes significantly stronger for the QDs compared to the bulk material. This band gap bowing arises from a combination of structural and chemical factors. Structurally, the size mismatch between Cd and Zn atoms induces lattice strain. This strain disrupts the ideal crystal structure, modifying cation-anion-cation and anion-cation-anion bond angles and leading to the relaxation of anion-cation bond lengths within the alloy. Additionally, the replacement of the binary constituents' lattice constants with an alloy lattice

constant causes a volume deformation of the band structure [151]. Chemically, bowing can also be attributed to differences in electronegativity and band offsets between the constituent binary materials [151].

In Fig. 4.9 it is easily noticeable the bowing effect is more pronounced for the LUMO compared to the HOMO. For example, as the alloy composition (x) increases from 0 to 0.2, the LUMO level shows a significantly larger shift of approximately 200 meV, while the HOMO level experiences a shift of less than 100 meV in the case of a 3.2 nm dot. This difference in the energy level shifts is due to the distinct orbital character of the HOMO and LUMO states. The LUMO in II-VI semiconductors is primarily composed of cation s-states (Cd or Zn in our case), while the HOMO is dominated by anion p-states. Since we have varied the cation composition (Cd and Zn), the impact on the s-orbital-dominated LUMO is more significant, leading to a stronger bowing effect compared to the p-orbital-dominated HOMO.

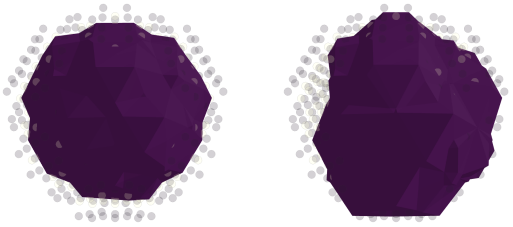

(a) e_0 (b) h_0

Figure 4.10: Squared wavefunction envelopes with 75 % state density for (a) LUMO (e_0) and (b) HOMO (h_0) for a 3.2 nm $Zn_{0.2}Cd_{0.8}Se$ alloyed QD. The small grey scatter dots represent the atoms in the QD.

Alloyed $Zn_{1-x}Cd_xSe$ quantum have type-I band alignment irrespective of the variations in size and alloy composition. Fig. 4.10 exemplifies this for a 3.2 nm $Zn_{0.2}Cd_{0.8}Se$ alloyed dot where squared wavefunction envelopes of both HOMO and LUMO states remain well localized within the dot, signifying a type-I alignment. The observed distortion of the squared wavefunction envelopes in Fig. 4.10 likely arises from the small size of the dot and a small compositional in-homogeneity which influences the shapes of the wavefunctions.

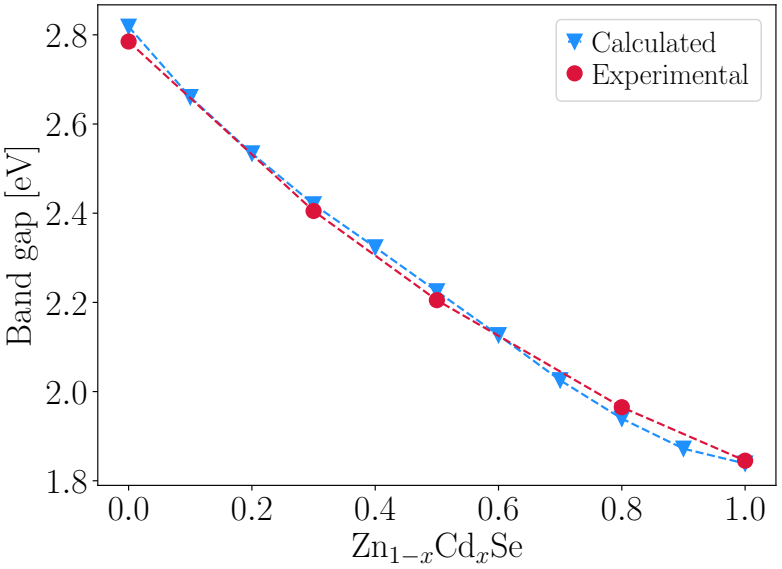

Figure 4.11: Comparison of calculated and experimental band gap in bulk $Zn_{1-x}Cd_xSe$ for varying x. Experimental data is taken from ref. [152, 153]. To account for the temperature effect at room temperature, we shifted the experimental data by adding 100 meV.

Fig. 4.11 compares our calculated band gap for bulk $Zn_{1-x}Cd_xSe$ alloys with experimental measurements of band gaps in bulk-like $Zn_{1-x}Cd_xSe$ nanowires [152, 153]. These nanowires have diameters ranging from 60 to 150 nm and lengths of several tens of micrometers. The experimental data is shifted upward by 100 meV to account for the temperature effect, as the measurements were performed at room temperature. A good agreement is observed between the measured and calculated data.

In the next step, we investigate strain effects on individual energy levels in alloyed dots. In Fig. 4.12 (unoccupied states) and Fig. 4.13 (occupied states), we show the first 18 SP states including spin for alloyed dots. Each subplot displays the energy levels for a specific alloy composition (x) as different colors for varying size dots.

In pure spherical QDs with T_d symmetry, the lowest unoccupied electronic state has two-fold degeneracy, including spin (see Fig. 4.12 for $x = 0$ or $x = 1$ case). This is followed by a set of 6 p-states and followed by a set of 10 d-states including spins. The highest occupied state is a four-fold degenerate set and is followed by another set of four-fold degenerate states (see Fig. 4.13 for $x = 0$ or $x = 1$ case). Alloying breaks the degeneracy observed in pure CdSe or ZnSe QDs, as shown in Figs. 4.12 and 4.13. For example, in the case of $0 < x < 1$, the p-states lose their six-fold degeneracy and split into distinct energy levels. This splitting depends on both the alloy concentration and the size of the dot. Interestingly, for a fixed alloy composition, the splitting becomes

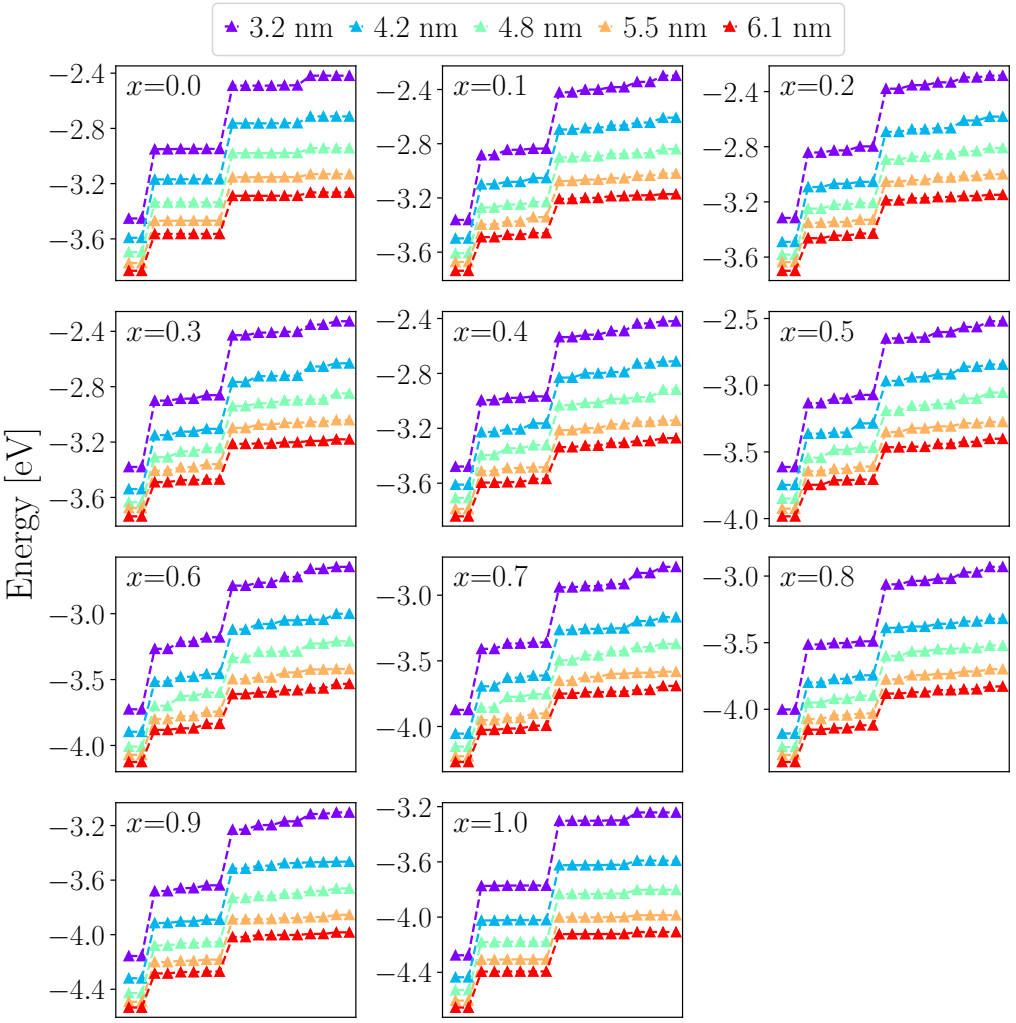

Figure 4.12: First 18 lowest unoccupied SP energy levels for $Zn_{1-x}Cd_xSe$ alloyed QDs with varying diameters.

more pronounced for smaller dots due to the enhanced influence of alloying effects under stronger confinement. Similar to the unoccupied states, the four-fold degenerate highest occupied states also splits, reaching up to several meV in energy difference. The observed splitting of the first two occupied states (excluding spin) arises from the crystal field effect due to a change in bond lengths within the alloyed QD. This splitting plays a significant role in the fine structure of excitonic states, which will be discussed in detail in the next section.

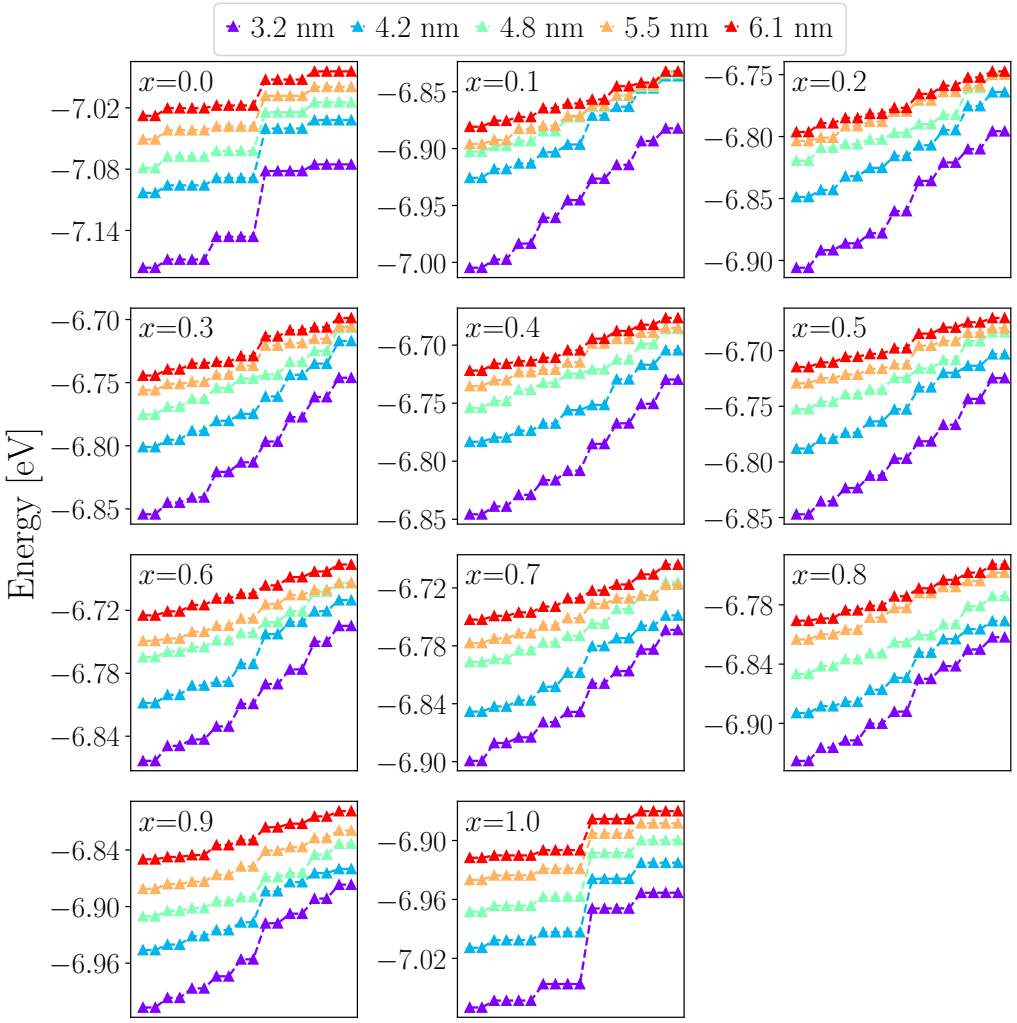

Figure 4.13: First 18 highest occupied SP energy levels for $Zn_{1-x}Cd_xSe$ alloyed QDs with varying diameters.

4.5.1.2 Dot-in-rod heterostructures

In Fig. 4.14, we present the calculated energies of the HOMO and LUMO states for dot-in-rod heterostructures. While experimentally fabricated structures have incorporated alloyed dots, we have also calculated the case of a pure ZnSe dot within a CdS rod for a better understanding. For comparison, Fig. 4.14 additionally shows the HOMO and LUMO levels for 3.2 nm pure CdSe and ZnSe dots. As presented in Fig. 4.14, the calculated band gap for the 3.2 nm pure ZnSe dot is 3.623 eV. On growing a CdS shell on top of the ZnSe dot, the band gap decreases sharply to 2.634 eV. While the LUMO state is lowered in energy sharply, the HOMO state is slightly moved up in energy. This behavior is consistent with the type-II band alignment of ZnSe and CdS, as illustrated

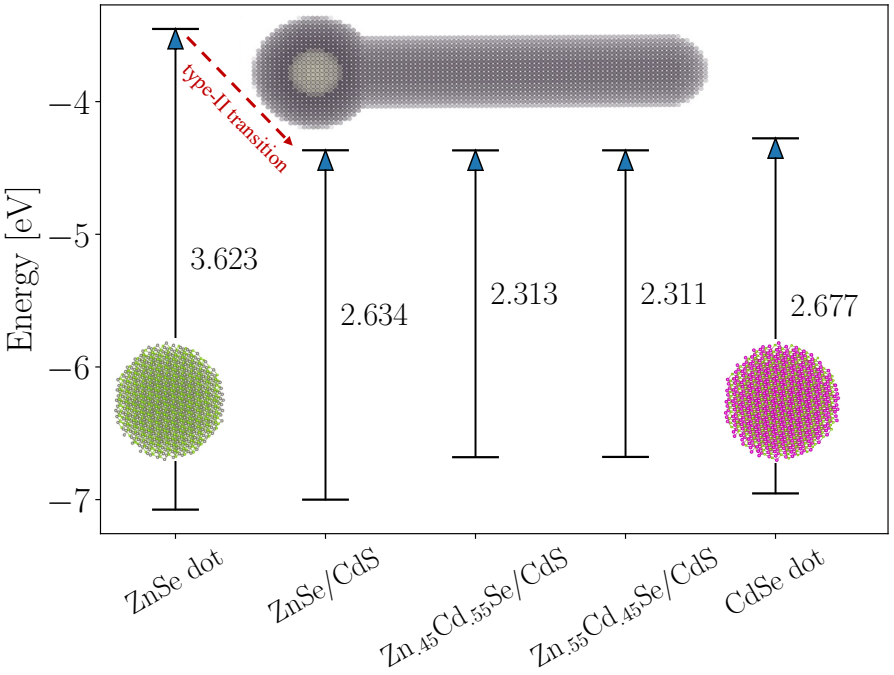

Figure 4.14: SP HOMO and LUMO levels for 3.2 nm dot and 3.2 nm dot in CdS rod structure. Arrow (red) indicates the type-II transition upon CdS rod growth on top of the pure dot.

in Fig. 4.6. The figure shows that the VBM of CdS is lower in energy than ZnSe by 210 meV, while the CBM of CdS is significantly lower by 530 meV. This large offset in the conduction band edges confines the electrons (LUMO) within the CdS shell, leading to the observed decrease in the overall band gap and a type-II nanostructure.

When considering 45% and 55% Zn alloyed dots within the CdS rod structure (compared to the pure ZnSe case), the calculated results show a minimal change in the LUMO state energy as it is still localized in the CdS shell. In contrast, the HOMO state has an upward shift in the energy. This behavior is due to the band gap bowing effect observed in the alloyed dots, as discussed previously and illustrated in Fig. 4.9. The alloyed dot within the CdS shell likely retains a type-II band alignment, similar to the pure ZnSe dot in CdS. This means the electron (LUMO) is still primarily confined within the CdS shell, while the hole (HOMO) is localized in the alloyed dot, as shown in Fig. 4.15(a).

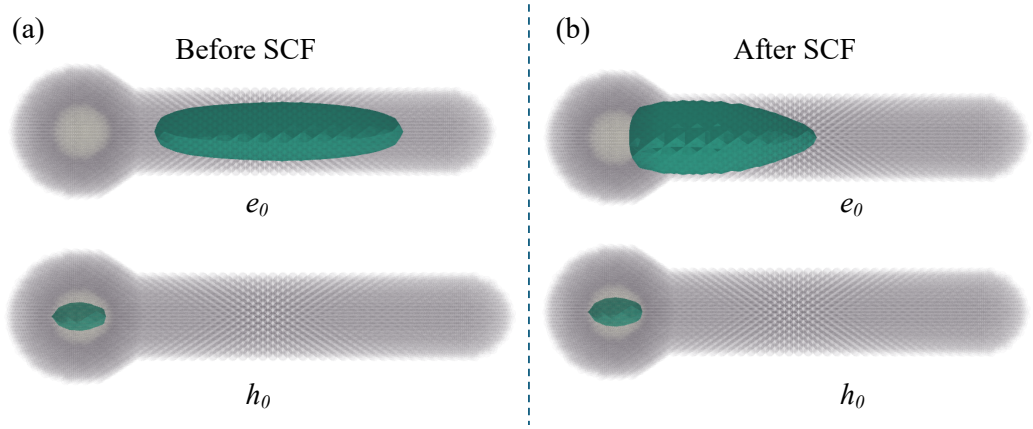

Figure 4.15: Calculated HOMO (h_0) and LUMO (e_0) wavefunction probability density (in green) with 75 % distribution for a ZnSe/CdS dot-in-rod nanostructure (a) Results without electron-hole (e-h) interaction (b) Results including e-h interaction after self-consistent calculations (SCF).

In dot-in-rod structures, the spatial separation of electrons and holes weakens their interaction. The conventional CI approach, commonly used for type I QDs, becomes impractical for calculating exciton states in this situation. We therefore include a self-consistent mean field self-consistent (SCF) calculation method for electron-hole pair excitations within the EPM framework. A similar approach has been developed previously by Matsuda et al. [154]. The SCF Hamiltonian is written as:

$$\left\{-\frac{\beta}{2}\nabla^2 + V_{\mathrm{loc},\alpha}^{\mathrm{EPM}}(\mathbf{r}) + \widehat{V}_{\alpha}^{\mathrm{SO}}(\mathbf{r}) + e^2\int \frac{\rho(\mathbf{r}')}{\varepsilon(\mathbf{r}-\mathbf{r}')|\mathbf{r}-\mathbf{r}'|}d^3\mathbf{r}'\right\}\psi_i(\mathbf{r}) = \epsilon_i\psi_i(\mathbf{r}). \quad (4.21)$$

where $\rho(\mathbf{r}')$ represents the electron (or hole) density at point $\mathbf{r}'$. We then self-consistently solve the Hamiltonian for an electron in the presence of a hole (or vice versa). Here, the dielectric screening $\varepsilon(\mathbf{r}-\mathbf{r}')$ is approximated as constant bulk screening obtained by averaging the ZnSe and CdSe. Additionally, the surrounding low-dielectric constant media leads to dielectric confinement, which further influences the excitonic FS by introducing electron-hole self-interaction and affecting the electron-hole overlap. However, the effect of dielectric confinement is neglected due to the bigger size of the structure.

Fig. 4.15 compares the electron and hole wavefunctions before and after self-consistent calculations for a pure ZnSe dot embedded in a CdS rod. As expected, the hole wavefunction shows minimal change due to its strong confinement within the dot. In contrast, the electron wavefunction moves closer to the dot as a result of the self-consistent interaction with the hole. This leads to an increased overlap between the electron and

hole wavefunctions. Interestingly, despite this overlap, the change in the energy of electron and hole states is relatively small, on the order of 50 meV. For $Zn_{0.55}Cd_{0.45}Se/CdS$ dot-in-rod nanostructure results are presented in Fig. 4.16. Compared to the pure ZnSe/CdS case, e_0 and h_0 relatively have small overlap in $Zn_{0.55}Cd_{0.45}Se/CdS$ structure.

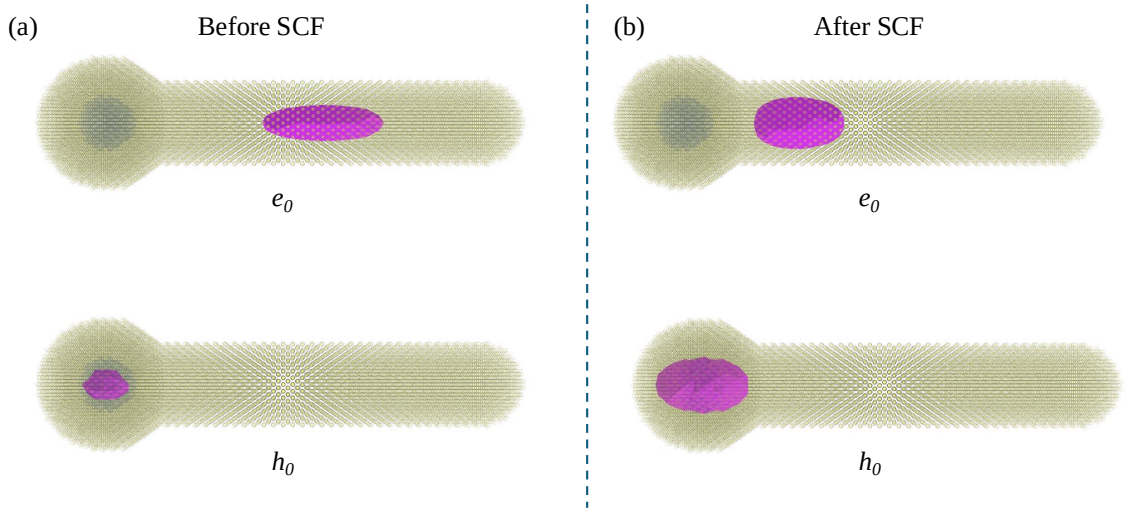

Figure 4.16: Similar to Fig. 4.15 but for $Zn_{0.55}Cd_{0.45}Se/CdS$ dot-in-rod nanostructure.

4.5.2 Excitonic Fine Structure

In this section, we show the effect of alloying on the excitonic FS in both alloyed QDs and dot-in-rod nanostructures. The excitonic fine structure is calculated within screened configuration interaction formalism (see sec. 2.4) with SP wavefunctions obtained within the SLCBB method discussed in sec. 4.2.1.

4.5.2.1 Alloyed dots

In Fig. 4.17, we present the calculated excitonic fine structure of different size $Zn_{1-x}Cd_xSe$ dots with varying x. The energy of the lowest exciton state (E_0) is set to zero for a comparative reference. Each subplot shows the fine structure for a specific dot size, with varying color intensity representing the oscillator strength of each energy level. The black lines in each subplot of Fig. 4.17 correspond to the energy splitting between the two highest occupied SP states (excluding spin).

Group theory analysis predicts a five-fold low-energy dark state and a three-fold high-energy bright state for spherical pure dots in T_d point group [63, 68], as illustrated

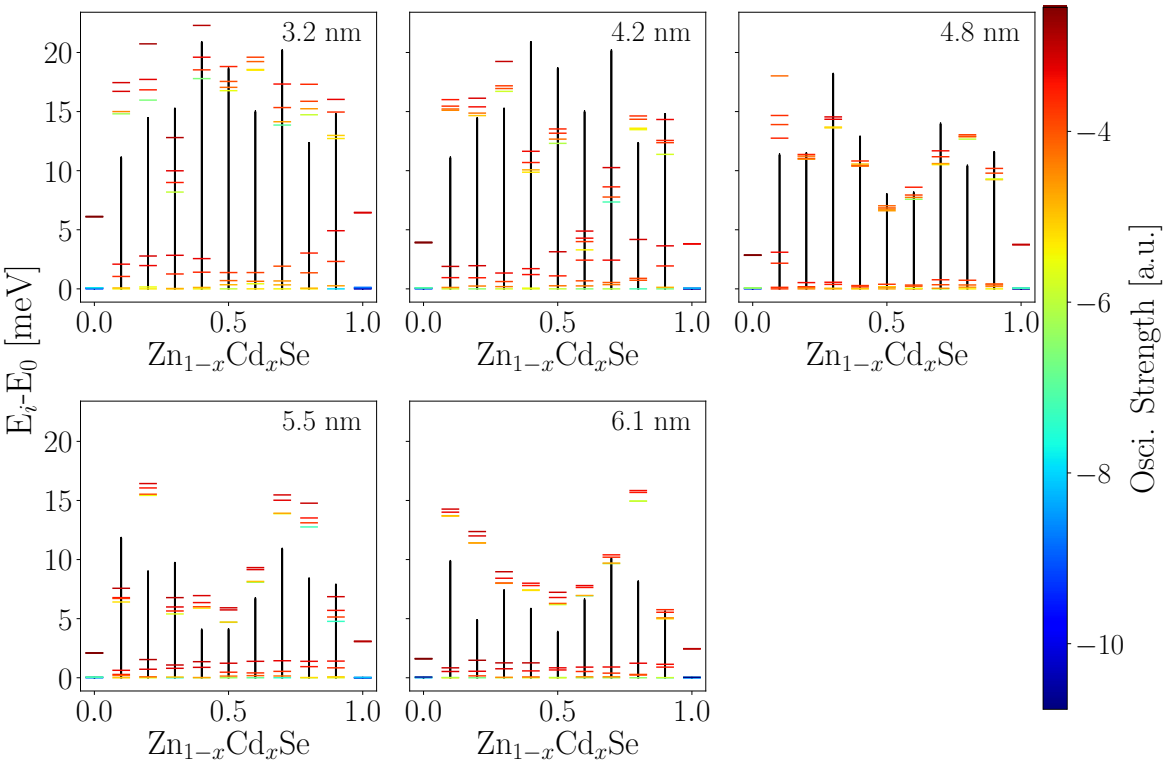

Figure 4.17: Calculated excitonic fine structure for $Zn_{1-x}Cd_xSe$ dots with various alloy compositions (x) and sizes. The energy of the lowest exciton state (E_0) is set to zero for reference. The black lines correspond to the energy splitting between the two highest occupied SP states (excluding spin). Color represents the logarithm (base 10) of the oscillator strength for each excitonic level.

in Fig. 4.18. As expected from theory, our calculations for pure ZnSe ($x = 0$) and CdSe ($x = 1$) dots have five low-energy, dark electronic states and three high-energy, bright states for all dot sizes. This degeneracy (five-fold for dark and three-fold for bright states) is consistent with the spherical symmetry of the pure dots. Furthermore, the energy difference between the bright and dark states, known as the dark-bright (DB) splitting, increases as the dot size decreases. This trend is well understood as stronger localization of wavefunction in small dots leads to their higher overlap and hence increases exchange integral which increases the DB splitting.

However, the situation changes significantly for the alloyed dots. Unlike the pure case, the degeneracy of the excitonic states is lifted. In pure dots, the SP state h_0 is a four-fold state while in alloyed dots this is no longer four-fold due to crystal field i.e. change in bond lengths. The electron-hole pair, which was 8x degenerate for T_d symmetry becomes split into two 4x states due to this crystal field splitting. The lower 4x set originated from e_0 and h_0 states at SP levels while the upper 4x set is originating

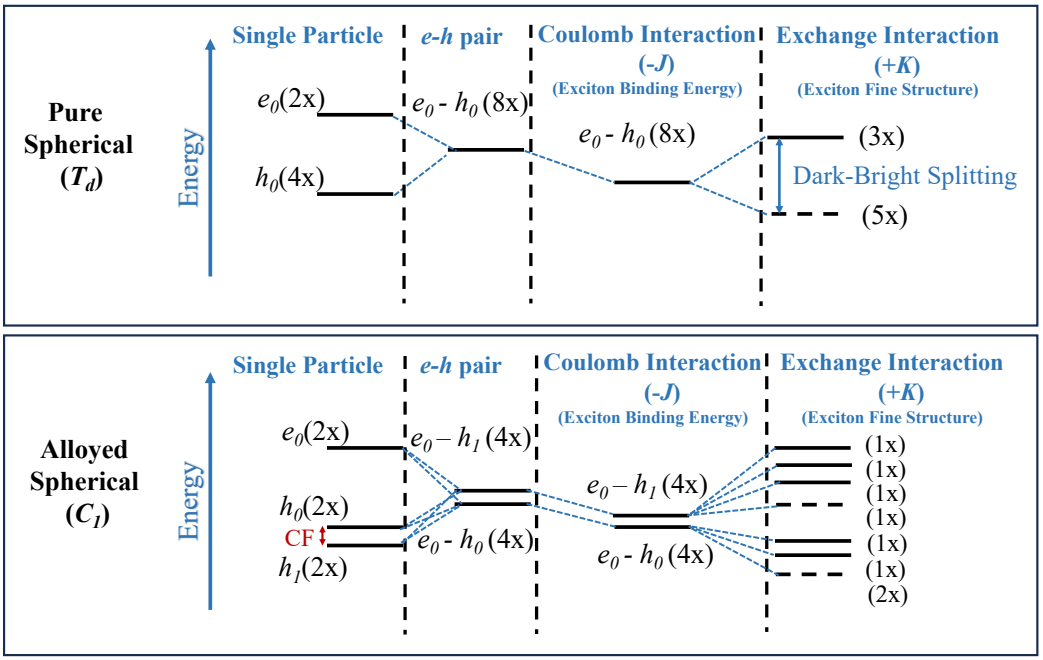

Figure 4.18: Illustrative comparison of excitonic fine structure of highly symmetric (T_d) pure dots with reduced symmetry (C_1) alloyed dots. Optically passive dark states are shown with dashed lines and optically active bright states are represented by solid lines with their degeneracy indicated.

from e_0 and h_1. Including the J lowers the energy of these states similar to the pure case but does not change the degeneracies of the levels. The addition of K further splits these 4x states. A schematic comparison of excitonic fine structure for pure spherical dots and alloyed dots is presented in Fig. 4.18. For the lower energy 4x set originating from $e_0 - h_0$, the lowest two states are always dark and are very close in the energy of the order of less than 0.1 meV which can easily be overcome by thermal energy above 2 Kelvin and hence we consider them as degenerate. The other two states are bright and split differently for different alloy concentrations. However, the 4x set originating from $e_0 - h_1$ becomes split by the exchange interaction into a set of 4 singly degenerate states where the lowest state is dark and the other three are bright states. These three states split differently for different alloy concentrations. Noticeably, the splitting between the 4x-4x electron-hole pair sets is also modified by alloy concentration. The splitting between the two 4x-4x electron-hole sets is larger than the splitting between states within those sets. The splitting between the two 4x electron-hole sets arises from the splitting of h_0 and h_1 at the SP level and the exchange interaction while within the two 4x-4x electron-hole sets, it is due to exchange interaction. Splitting of

SP h_0 and h_1 (magnitude marked with a black arrow in Fig. 4.17) is larger than the exchange interaction causing a larger splitting between these two 4x-4x sets. Overall, no general trends can be established for the splitting behavior as it varies significantly across different alloy compositions for all sizes.

4.5.2.2 Dot-in-rod

This section presents the calculated FSS of three different dot-in-rod structures. We investigated a pure ZnSe dot embedded in a CdS rod, as well as $Zn_{0.45}Cd_{0.55}Se$ and $Zn_{0.55}Cd_{0.45}Se$ alloyed dots within a CdS rod. All structures have identical dot and rod dimensions. The FSS is presented after including the Coulomb interaction at the SP level discussed previously. The qualitative trend of the FSS for these structures

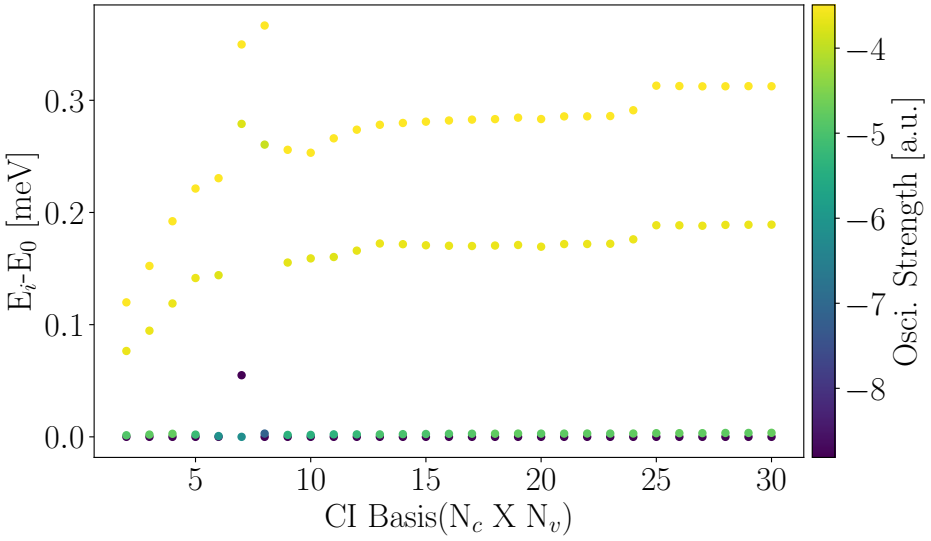

Figure 4.19: Convergence of excitonic fine structure in ZnSe/CdS dot-in-rod structure with increasing configuration interaction (CI) basis size. The number of unoccupied (N_c) and occupied (N_v) states included in the CI basis are increased equally in steps of 1.

remains very similar to that observed for the isolated alloyed dot with two 4x-4x sets in the lowest exciton. These two sets are separated by order of $>$ 10 meV ($\sim$110 Kelvin). Consequently, the higher energy set of 4x states will have negligible influence on photoluminescence (PL) dynamics at low temperatures. Therefore, we focus solely on the properties and discussion of the lower-energy 4x states.

Fig. 4.19 illustrates the convergence behavior of the four lowest excitonic states

with respect to the size of the CI basis set in a pure ZnSe dot embedded within a CdS rod structure. The energy of the lowest exciton state (E_0) is set to zero as a reference for comparison. Each data point represents the energy of an individual excitonic state, while the color coding indicates the corresponding state's oscillator strength. As can be seen, the lowest two states are dark while the two higher energy states are bright. The convergence of the FSS (or exchange splitting) is quite slow compared to colloidal spherical QDs the FSS converges very quickly [68]. This happens due to a strong interaction between different configurations within the dot-in-rod structure. While we achieved proper convergence of the FSS for all investigated structures, the convergence behavior itself is not presented here for other structures. In the final results, we have included 30 e and 30 h states in the CI basis.

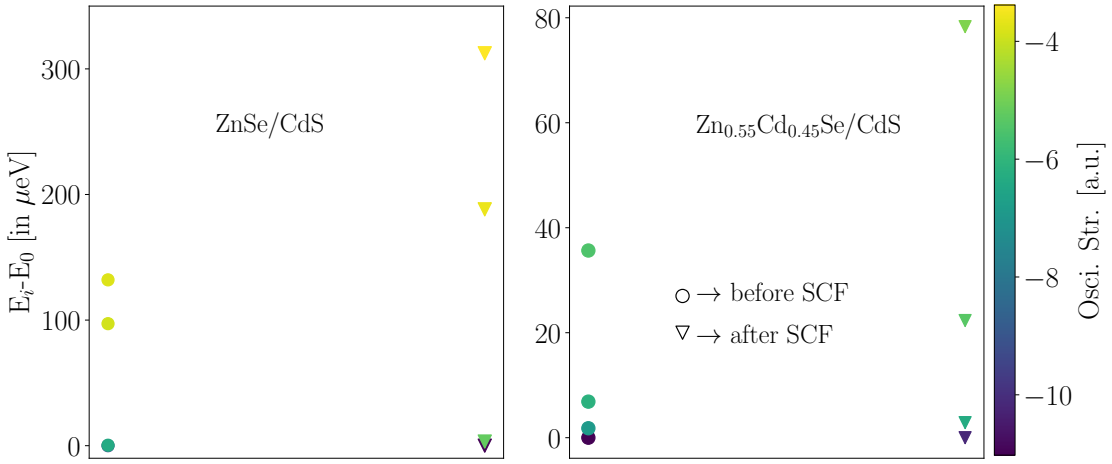

Figure 4.20: FS in ZnSe/CdS and $Zn_{0.55}Cd_{0.45}Se$/CdS structures before (filled circles) and after (filled triangles) SCF.

In Fig. 4.20, we illustrate the impact of including the e-h Coulomb interaction, as described by Eq.4.21, on the excitonic fine structure (FS). The results are shown for ZnSe/CdS and $Zn_{0.55}Cd_{0.45}Se$/CdS structures, both before (filled circles) and after (filled triangles) including the Coulomb interaction (or SCF). We focus on the four lowest excitonic states. It is evident that, in both structures, the character of the states remains largely consistent before and after the SCF cycle, with the two lowest states being dark and the two higher states being bright. However, the energy splittings between these states are significantly influenced by the SCF cycle. Specifically, in both cases, the splitting between the upper and lower states increases by approximately a factor of three after the SCF cycle.

This increase in splittings is a direct consequence of the enhanced e-h exchange

integrals, as reflected by the wavefunction overlap shown in Fig.4.15 and Fig.4.16, following the SCF cycle. These results underscore the critical importance of the SCF optimization of the wavefunctions before CI.

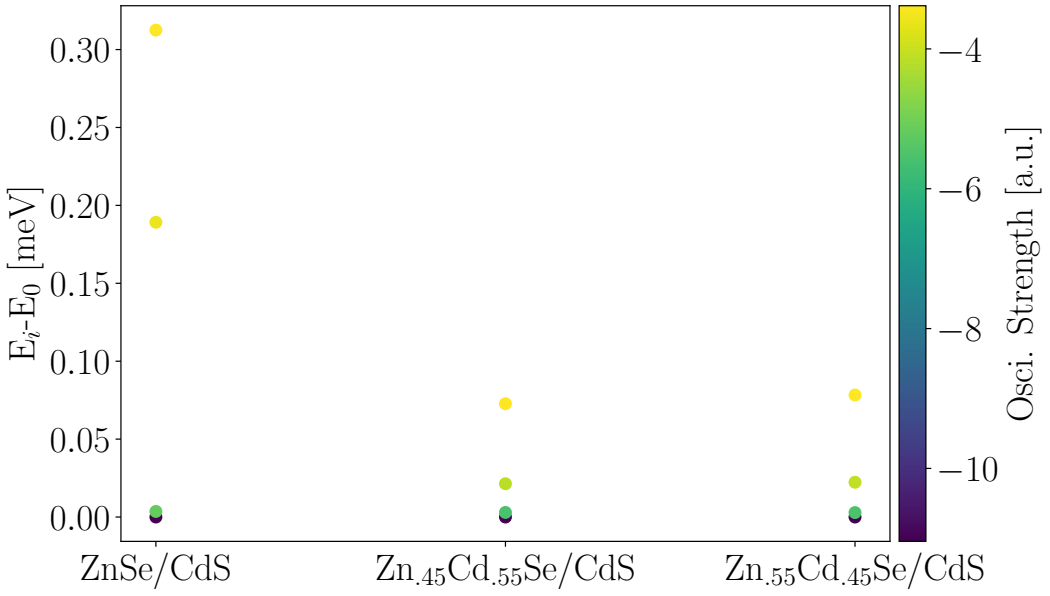

Figure 4.21: Energy levels and oscillator strengths of the lowest four excitonic states in various dot-in-rod structures after SCF. The Color represents the oscillator strength's logarithm (base 10) for each excitonic level.

In Fig. 4.21 we present the calculated energies of the four lowest excitonic states for all three investigated dot-in-rod structures. For all structures, we have obtained a qualitatively similar trend: the two lower energy states are 'dark', while the higher energy states are 'bright'. The exchange splitting between the excitonic states is three times larger in pure ZnSe/CdS structure compared to the two other cases due to larger strain in $Zn_{0.55}Cd_{0.45}Se/CdS$ and $Zn_{0.45}Cd_{0.55}Se/CdS$ structures.

The calculated results for the exciton fine structure in these dot-in-rod nanostructures provide valuable insights into the low-temperature PL decay behavior we expect to observe (referencing Fig. 4.3). These calculations show the low-temperature decay will involve 2 energetically separated bright states and two energetically very close (order of μeV) dark states and the ground state. This existence of multiple radiative and non-radiative decay pathways arising from different excited states can contribute to a multi-exponential decay profile in the PL decay curve. As temperature increases, some of the slower decay pathways involving the dark states might become suppressed. This could lead to a simplification of the PL decay curve at higher temperatures, potentially transitioning towards a more single-exponential character.

In conclusion, we use a fully atomistic approach to calculate the exciton fine structure of alloyed $Zn_{1-x}Cd_xSe$ dot structures as well as $Zn_{0.45}Cd_{0.55}Se$, $Zn_{0.55}Cd_{0.45}Se$ dots in CdS rod structures. Our calculated results show that creating alloys introduces strain due to lattice mismatch which creates crystal field splitting among SP levels as compared to the pure dots. This splitting at a SP level translates to qualitative different excitonic fine structures in alloyed dots and shows that alloyed dots will have inherently multi-exponential PL decay. The calculated FS for dot-in-rod structures shows that the low-temperature PL decay will include multiple excitonic levels and explains the multi-exponential PL decay measured in experiments. The calculated excitonic levels provide a foundation for further studies. We can now extend this work to encompass calculations of excitonic lifetimes and model PL decay, ultimately leading to a more comprehensive understanding of the material's exciton dynamics and radiative recombination processes.

Chapter 5

Empirical Band-Gap Correction for LDA-Derived Atomic Effective Pseudopotentials

This chapter is adapted from the published work "Empirical Band-Gap Correction for LDA-Derived Atomic Effective Pseudopotentials" by **S. Kumar**, H. Bui, and G. Bester, *Comp. Cond. Mat.* **40** (2024) e00917 [112]. All calculations, data analysis, and drafting of the manuscript were conducted by the first author, **S. Kumar**

Experimentally synthesized nanostructures can range from just a few to several thousand atoms. DFT provides accurate qualitative descriptions of material properties for structures up to a few hundred atoms. However, for bigger structures, DFT is limited by a high computational cost. As an alternative, Cardenas and co-workers [67] have developed atomic effective pseudopotentials (AEPs) that can handle up to several thousand atoms with high accuracy. AEPs were derived via an analytic connection to the effective crystal potential from DFT. The concept of AEPs ideally bypasses the need for a self-consistent solution. Additionally, it opens the possibility to focus only on a selected part of the eigenvalue spectrum. Here, unlike DFT calculations, the number of total states required is independent of the number of atoms. Hence, AEPs are ideal for observing the optical properties of nanostructures where only energy states in the neighborhood of the band gap are of importance.

5.1 Atomic Effective Pseudopotentials

5.1.1 Analytic connection between AEPs and effective Kohn-Sham potentials

As already mentioned in chapter 2, the basis of DFT is the KS equation:

$$\Big(-\frac{\hbar^2}{2m}\Delta + V_{\mathrm{KS}}(\mathbf{r})\Big)\psi_i(\mathbf{r}) = \epsilon_i\psi_i(\mathbf{r}),$$

where the effective KS potential $V_{\mathrm{KS}}(\mathbf{r})$ describes the interaction of an electron with its environment including other electrons:

$$V_{\mathrm{KS}}(\mathbf{r}) = V_{\mathrm{ext}}(\mathbf{r}) + V_{\mathrm{H}}[n_0(\mathbf{r})] + V_{\mathrm{XC}}[n_0(\mathbf{r})] \tag{5.1}$$

with

$$n_0(\mathbf{r}) = \sum_{i}^{occ} |\psi_i(\mathbf{r})|^2$$

is the electron density of all occupied states. The external potential $V_{\mathrm{ext}}(\mathbf{r})$ is replaced by a weaker one pseudopotential $V(\mathbf{r})$ in the pseudopotential approximation. The local and non-local part of the pseudopotential, in the representation of angular momentum projectors, can be expressed:

$$V_{\mathrm{loc}}(\mathbf{r}) = \sum_{\alpha n} v^{\alpha}_{\mathrm{loc}}(|\mathbf{r} - \boldsymbol{\tau}^{\alpha n}|), \tag{5.2}$$

$$V_{\mathrm{nloc}}(\mathbf{r}) = \sum_{\alpha n}\sum_{lm} \delta v^{\alpha l}(|\mathbf{r} - \boldsymbol{\tau}^{\alpha n}|)\hat{P}^{\alpha n, lm}, \tag{5.3}$$

where α stands for atom type running from 1 to N_{species}, n is the atom index which runs from 1 to the total number of atoms N_α for each atom type α. $\boldsymbol{\tau}^{\alpha n}$ are the atomic position and $\hat{P}^{\alpha n, lm}$ is the projection operator. The potential $v^{\alpha}_{\mathrm{loc}}$ defined in Eq. (5.2) is the norm-conserving pseudopotential constructed using the approach of Troullier and Martins [155]. Using the Kleinman and Bylander form [156, 157], the pseudopotential is rewritten as:

$$V_{\mathrm{KS}} = V_{\mathrm{loc}}(\mathbf{r}) + V_{\mathrm{H}}[n_0] + V_{\mathrm{XC}}[n_0] + \sum_{lm} |\chi^{lm}_{\mathrm{KB}}\rangle E^{l}_{\mathrm{KB}} \langle\chi^{lm}_{\mathrm{KB}}|, \tag{5.4}$$

where the last term is the non-local part of the potential and E^l_{KB} are the Kleinman-Bylander eigenvalues

$$E^l_{\mathrm{KB}} = \frac{\langle \delta V_l u_l | \delta V_l u_l \rangle}{\langle u_l | \delta V_l | u_l \rangle}, \tag{5.5}$$

and χ^{lm}_{KB} being the normalized Kleinman-Bylander projectors

$$|\chi^{lm}_{\mathrm{KB}}\rangle = \frac{|\delta V_l u_l m|}{\langle u_l \delta V_l | \delta V_l u_l \rangle}, \tag{5.6}$$

where u_{lm} is an eigenstate of the atomic pseudo-Hamiltonian. To construct AEPs, we use the local part of the self-consistent effective Kohn-Sham potential

$$V_{\mathrm{loc,KS}}(\mathbf{r}) = V_{\mathrm{loc}}(\mathbf{r}) + v_{\mathrm{H}}[n_0] + v_{\mathrm{XC}}[n_0]. \tag{5.7}$$

The effective potential in reciprocal space is Fourier transformed from real space effective potential as:

$$V_{\mathrm{loc,KS}}(\mathbf{G}) = \frac{1}{\Omega_{\mathrm{c}}} \int_{\Omega_{\mathrm{c}}} V_{\mathrm{loc,KS}}(\mathbf{r}) e^{-i\mathbf{G}.\mathbf{r}} d^3r, \tag{5.8}$$

where Ω_{c} is the volume of the unit cell. In real space, we can write effective potential as a sum of atom-centered potentials

$$V_{\mathrm{loc,KS}}(\mathbf{r}) = \sum_{\alpha}^{N_{\mathrm{species}}} \sum_{n}^{N_\alpha} v_\alpha(\mathbf{r} - \boldsymbol{\tau}^{\alpha n}), \tag{5.9}$$

and then transformed back into the reciprocal space as:

$$V_{\mathrm{loc,KS}}(\mathbf{G}) = \frac{1}{\Omega_{\mathrm{c}}} \sum_{\alpha}^{N_{\mathrm{species}}} \sum_{n}^{N_\alpha} v_\alpha(\mathbf{G}) e^{-i\mathbf{G}.\boldsymbol{\tau}^{\alpha n}}, \tag{5.10}$$

where

$$v_\alpha(\mathbf{G}) = \int_{\infty} v_\alpha(\mathbf{r}) e^{-i\mathbf{G}.\mathbf{r}} d^3r, \tag{5.11}$$

are the AEPs for different types of atoms.

5.1.2 AEPs construction

The AEPs of a binary system are indirectly constructed through v_+ and v_-:

$$v_+ = v_{\mathrm{a}} + v_{\mathrm{c}}, \tag{5.12}$$

$$v_- = v_\mathrm{a} - v_\mathrm{c}, \tag{5.13}$$

using the anion v_a and the cation v_c potentials. In any binary system, the effective is presented as the sum of anion and cation components

$$V^{(1)}_{\mathrm{loc,KS}}(\mathbf{r}) = \sum_{i=1}^{N_\mathrm{a}} v_\mathrm{a}(\mathbf{r} - \boldsymbol{\tau}^i) + \sum_{j=1}^{N_\mathrm{c}} v_\mathrm{c}(\mathbf{r} - \boldsymbol{\tau}^j). \tag{5.14}$$

With an inverted position structure where anion and cation positions are interchanged with the same atomic positions, the effective local potential is expressed as:

$$V^{(2)}_{\mathrm{loc,KS}}(\mathbf{r}) = \sum_{i=1}^{N_\mathrm{c}} v_\mathrm{c}(\mathbf{r} - \boldsymbol{\tau}^i) + \sum_{j=1}^{N_\mathrm{a}} v_\mathrm{a}(\mathbf{r} - \boldsymbol{\tau}^j). \tag{5.15}$$

From sum of equations (5.14) and (5.15), we simply lead to

$$\sum_{n=1}^{N_\mathrm{atoms}} v_+(\mathbf{r} - \boldsymbol{\tau}^n) = V^{(1)}_{\mathrm{loc,KS}}(\mathbf{r}) + V^{(2)}_{\mathrm{loc,KS}}(\mathbf{r}) = V^{(1+2)}_{\mathrm{loc,KS}}(\mathbf{r}), \tag{5.16}$$

and

$$\sum_{n=1}^{N_\mathrm{atoms}} (-1)^{n+1} v_-(\mathbf{r} - \boldsymbol{\tau}^n) = V^{(1)}_{\mathrm{loc,KS}}(\mathbf{r}) - V^{(2)}_{\mathrm{loc,KS}}(\mathbf{r}) = V^{(1-2)}_{\mathrm{loc,KS}}(\mathbf{r}). \tag{5.17}$$

The Fourier transforms of Eqs. (5.16) and (5.17) gives us following expressions:

$$V^{(1+2)}_{\mathrm{loc,KS}}(\mathbf{G}) = \frac{1}{\Omega}\int_\Omega V^{(1+2)}_{\mathrm{loc,KS}}(\mathbf{r}) e^{i\mathbf{G}.\mathbf{r}} d^3r = \frac{1}{\Omega}\sum_{n=1}^{N_\mathrm{atoms}} e^{i\mathbf{G}.\boldsymbol{\tau}^n} v_+(\mathbf{G}), \tag{5.18}$$

$$V^{(1-2)}_{\mathrm{loc,KS}}(\mathbf{G}) = \frac{1}{\Omega}\int_\Omega V^{(1-2)}_{\mathrm{loc,KS}}(\mathbf{r}) e^{i\mathbf{G}.\mathbf{r}} d^3r = \frac{1}{\Omega}\sum_{n=1}^{N_\mathrm{atoms}} (-1)^{n+1} e^{i\mathbf{G}.\boldsymbol{\tau}^n} v_-(\mathbf{G}). \tag{5.19}$$

Obtained $v_+(\mathbf{G})$ and $v_-(\mathbf{G})$ are complex in nature. However, only real parts of $v_+(\mathbf{G})$ and $v_-(\mathbf{G})$ are of interest within spherical approximation (SA) and can be extracted from 5.18 and 5.19 as:

$$V^{(\mathrm{SA})}_\pm(|\mathbf{G}|) = Re[v_\pm(\mathbf{G})] = \Omega\Big[\frac{Re[V^{(1\pm2)}_{\mathrm{loc,KS}}(\mathbf{G})]}{\beta_\pm} + \frac{Im[V^{(1\pm2)}_{\mathrm{loc,KS}}(\mathbf{G})]}{\alpha_\pm}\Big] \times \Big(\frac{\beta_\pm\alpha_\pm}{\beta_\pm^2 + \alpha_\pm^2}\Big) \tag{5.20}$$

where
$$\begin{aligned}\beta_+ &= \sum_{i=1}^{N_{\text{atoms}}} sin(\mathbf{G}.\boldsymbol{\tau}^n),\\ \alpha_+ &= \sum_{i=1}^{N_{\text{atoms}}} cos(\mathbf{G}.\boldsymbol{\tau}^n),\\ \beta_- &= \sum_{i=1}^{N_{\text{atoms}}} (-1)^{n+1} sin(\mathbf{G}.\boldsymbol{\tau}^n),\\ \alpha_- &= \sum_{i=1}^{N_{\text{atoms}}} (-1)^{n+1} cos(\mathbf{G}.\boldsymbol{\tau}^n).\end{aligned}$$

To obtain $V^{(1)}_{\text{loc,KS}}(\mathbf{G})$ and $V^{(2)}_{\text{loc,KS}}(\mathbf{G})$, DFT calculations are performed on two [100] elongated 24 atoms supercells. Both the supercells are identical with only cation and anion exchanged with each other. To extract long-range interaction, a deformation (5%) is applied along the slab direction to break the symmetry of the crystal. Calculation of potential from slabs and bulk unit-cell have a small difference [67] and therefore a Gaussian correction was applied to have the same effective local potential in supercells and bulk unit-cell calculations.

For heterostructures, the band offsets are very crucial and the band alignment needs to be determined correctly. We therefore link the AEPs of different binary materials together. We perform DFT calculations of two quantum wells (QWs) which comprise materials whose AEPs need to be linked. The lattice parameter is defined as the average of the lattice constants of the considered two materials. The values of $V(G)$ at $G = 0$ and small G are adjusted to reproduce DFT calculation of deformation potential of the valence band.

AEPs can be derived by using the LDA or the GGA. Over the years LDA/GGA has been very successful in describing ground-state properties, such as total energies and structural properties. However, these approximations usually result in a significant underestimation of the band gap and effective masses for semiconductors and insulators in DFT calculations. These errors are large, with differences ranging up to 100% [158, 159] from experimental values. Sometimes, LDA can even lead to the incorrect order of electronic states for materials such as HgTe [160, 161] and InAs [162]. This is a limitation when comparing with the experimental results and extracting the underlying physics. Consequently, being derived from LDA, AEPs inherit the underestimated band gaps and effective masses, which represents a serious problem in the realm of spectroscopic techniques.

Historically, great efforts have been made on the calculation of QP and optical gaps since the middle of the last century [163, 164, 165]. Based on many-body perturbation theory, the QP energies are described by Dyson's equation and are typically solved within the GW approximation [164, 159, 166, 167]. The optical gaps can be calculated *ab initio* by solving the Bethe-Salpeter equation [165, 168], using time-dependent

density functional theory [169] or the quantum Monte Carlo method [170, 171]. Additional methods such as hybrid functionals [80], self-interaction correction [77], and LDA+U [172] have also aimed at addressing the gap underestimation issue. Although these approaches can give an accurate description of the fundamental and optical gaps, all of them are currently only possible for either bulk systems or molecules up to one hundred atoms, due to the high computational demand.

As an alternative, various empirical corrections retaining the computational simplicity of LDA have been proposed. Such as corrections on the kinetic-energy density [79, 173, 174], correction to the local [175, 176], and the non-local [177, 178, 179, 180] components of the different pseudopotentials.

Motivated by the fact that the *GW* results suggest that the LDA bandstructure is qualitatively correct up to a rigid energy shift of the conduction bands, the so-called scissor shift has been introduced [181, 182, 158]. While the underlying idea is simple, the operator (scissor-operator) fulfilling the task is non-trivial, and also non-local [183, 184, 185, 186, 187], making this approach computationally more demanding. Furthermore, a rigid shift will not explicitly correct the low effective masses, which is a significant drawback for nanostructures, since confinement effects are directly linked to effective masses, as we will discuss further below.

In this work, we propose a simple empirical correction scheme (β-correction) to correct the band gap and improve the effective masses of LDA-derived AEPs. We validate our correction by a direct comparison with experimental results for (a) band energies at high-symmetry points in the Brillouin zone (b) effective masses for bulk InP, ZnS, GaAs, and HgTe (c) optical gaps (d) excitonic fine structure splitting for InP, CdSe, and GaAs QDs with different diameters. We use our findings to formulate a straightforward analytic expression, which can be adopted to correct the band gaps obtained using standard DFT codes in (small) QDs. Based on our excitonic screened configuration interaction (CI) results, we further provide an expression to obtain accurate optical gaps.

5.2 Correction Scheme

Using the separable form of the norm-conserving pseudopotential formulated by Kleinman and Bylander [81, 67, 156, 157], we can express the effective self-consistent poten-

tial as:

$$\widehat{V}_{\text{eff}} \equiv \widehat{V}_{\text{AEP}} + \widehat{V}_{\text{NL}},$$

with the non-local part from eq. 5.4:

$$\hat{V}_{\text{NL}} = \sum_{l,m} |l,m\rangle \, \delta V_l(r) \, \langle l,m| \quad , \tag{5.21}$$

where $|l,m\rangle$ are the spherical harmonics and δV_l is the difference between the l-dependent pseudopotential $V_l(r)$ and the selected local part part already taken into account in $\widehat{V}^{\text{AEP}}$ (see Refs. [157, 67]).

In order to improve the band gap and the effective masses we modify the non-local component of the pseudopotential according to:

$$\delta V_l^{\text{corr.}} = \begin{cases} \delta V_l(r) + \beta_l(1 + \cos\frac{\pi r}{r_c}) & \text{for} \quad r < r_c \\ 0 & \text{for} \quad r \geq r_c \quad , \end{cases} \tag{5.22}$$

within cut off radius $r_c = 2.25$ Bohr and β_l as correcting parameter. Our correction is localized close to the atomic core where we expect less impact on the inter-atomic bonding. The idea to correct only close to the atomic core is in line with the atomic pseudopotential idea in general. Indeed, a match between the pseudopotential and the accurate all-electron result in the pseudopotential construction is only guaranteed beyond a cut-off radius similar to ours [81, 155].

In most III-V and II-VI bulk semiconductors, the anion's p-orbital (l=1) largely determines the valence band maximum (VBM), while the cation's s-orbital (l=0) shapes the conduction band minimum (CBM). Although β-parameters can be applied for any orbital, here we need two parameters $\beta_{Cation-s}$ and $\beta_{\text{A}nion-p}$ for l=0 and l=1 respectively.

We choose bulk ZB InP as an example and in Fig. 5.1 plot the difference between AEP (LDA) and experimental results for (a) band gap and (b) the effective mass error as a function of the β-parameters. The thick lines in Fig. 5.1 indicate the values of β-parameters for which the differences between the calculated AEP and experimental values are zero. We can correct both, the band gap and masses, for moderate values of the parameters. However, both lines in Fig. 5.1 are nearly parallel pointing out that it is not possible to correct both the masses and gaps with the same set of parameters

which is the limitation of the approach. Therefore, we can correct either the band gap or the effective mass. In this work, we choose to correct the band gap at the cost of having overestimated effective masses. The opposite procedure, to correct the effective masses at the cost of having too low band gaps is a viable alternative that may be advantageous whenever the extracted physical observable depends strongly on the effective masses.

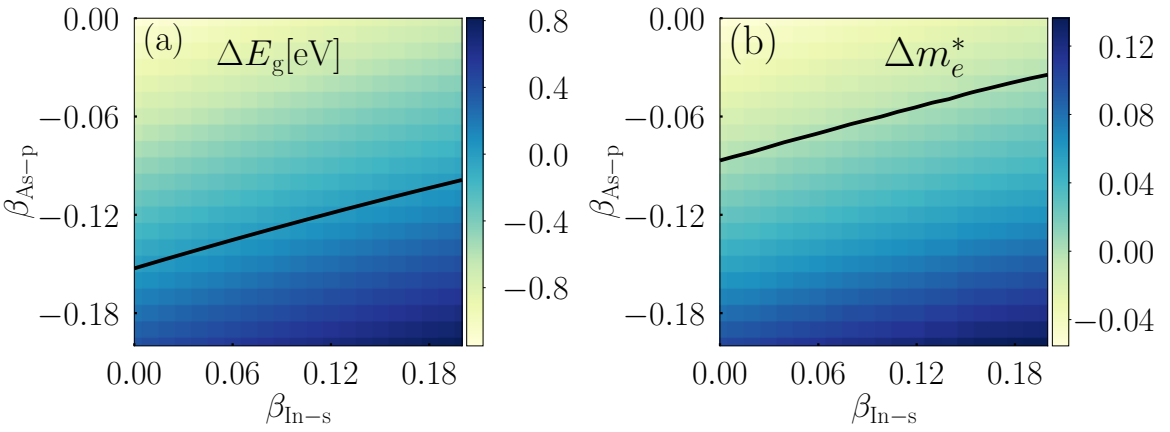

Figure 5.1: InP color-plot of the difference between the calculated and experimental values of (a) the band-gap ΔE_g and (b) the electron effective mass Δm_e^* as a function of the β-parameters. The solid line corresponds to the zero-value contour line and represents the perfect match to the experiment. Reprinted from ref. [112].

In Fig. 5.1(a) we show that any pair of correcting parameters (β_{In-s}, β_{As-p}) residing on the solid line yields the exact experimental band gap. Now we are left with the question related to the appropriate selection of this pair. Since β_{In-s} (β_{As-p}) is almost directly proportional to the CBM (VBM) shift, we use *GW* corrections to establish the appropriate weight of the CBM/VBM corrections, but fit the band gap to the experimental results and not to *GW* gap. We follow the simple procedure by initiating the selection by quantifying the error in the band gaps between the AEPs (LDA) and the *GW* methods for the given material. This involves determining the individual shifts in the CBM and VBM between LDA and *GW*. The shift can be determined with direct computation or from known literature [188, 160, 161]. For example, Klimes and co-workers [188] have presented results for most of the II-VI and III-V binary semiconductor materials and one can directly obtain the values for VBM and CBM shifts from their work. We then compute the relative contributions (in %) of the VBM and CBM shifts to the overall band gap difference between LDA and *GW* to use these values to correct the VBM and CBM energy levels in AEPs to fit the experimental gap.

For example, consider ZB bulk GaAs, which show a 0.87 eV gap difference between the LDA and GW_0 [188] results. The VBM shift of -0.78 eV in GW_0 w.r.t. LDA contributes 90% to the total gap difference, while the remaining 10% is contributed by the CBM. When applying β-correction to GaAs's AEP band gap with the experimental value (and not the GW gap, which can be off by several tens of percent, in this example 21%), we also choose a 90% VBM shift and a 10% CBM shift. This ensures a better physical description as GW results are of higher accuracy.

We now evaluate the corrections applied to both bulk and confined structures. For bulk materials, we calculate various band structure parameters, including energy band gaps for different symmetry points and effective masses. We then compare these calculated values with the experimentally extracted data and analyze the physical consequences of applied correction. For QDs, we explore the impact of corrections on the optical gap and fine structure.

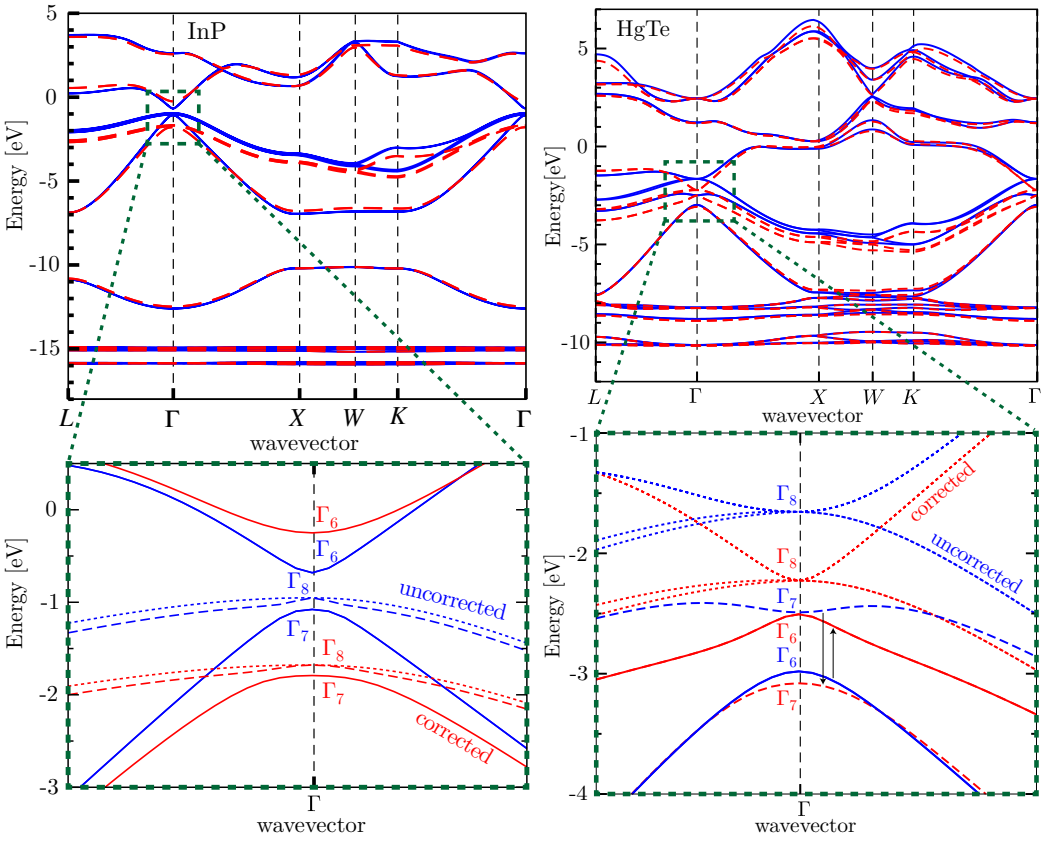

Figure 5.2: Band structure of ZB InP (left) and HgTe (right) calculated before (blue line) and after the β-correction (red dashed line). Bottom: magnification of the area in the green square. Reprinted from ref. [112].

5.3 Effect of the β-correction on the band structure

Band structure describes energy states for electrons as a function of momentum in a material, dictating its electrical, optical, and thermal properties which play a crucial role in designing materials for electronics, photonics, and many other applications.

We, therefore, illustrate the impact of the correction on the band structure for direct band gap InP and the semi-metal HgTe [160, 161] materials and show the results in Figs. 5.2. A qualitative comparison of corrected (red) and uncorrected bands (blue) shows that the top of the valence bands rigidly shifts to lower energies across the entire Brillouin zone, whereas deep bands are significantly less affected. A qualitative change in the bands is primarily seen close to the band gap. For InP (Fig. 5.2) the CBM is shifted up in energy. The curvature of the band is reduced after the correction and effective mass has increased. For HgTe, we observe very significant energy shifts and reordering of the bands around the Γ-point. In LDA calculations, and hence our AEPs [160, 161], a band inversion of the Γ_6 and Γ_7 bands is obtained, with Γ_7 being higher in energy than Γ_6 . This results in a qualitatively incorrect order of states, as the experimental order is Γ_7 being lower in energy than Γ_6. With β-correction, this issue is resolved such that ordering is restored of the Γ_6 and Γ_7 bands by shifting the Γ_6 band up and the Γ_7 band down in energy (following the arrows in Fig. 5.2).

We now compare further important band structure properties including band gaps at different symmetry points, spin-orbit splitting (Δ_{SO}), crystal field splitting (Δ_{CF}, only for WZ structures), and effective masses for bulk GaAs, InP, ZnS, and HgTe. All the results are summarised in Table 5.1. The corrected results have improved for the Γ-L_c (VB top at Γ to bottom of the CB at L) gap, the Γ-X_c (VB top at Γ to bottom of CB at X) gap. The error in the AEP (LDA) calculated Γ-L_c and Γ-X_c has decreased from approximately 40 % to about 5 % after our correction. The potentials for spin-orbit interaction are directly taken from DFT-derived norm-conserving pseudopotentials and not modified in our AEP methodology [156]. The agreement of the spin-orbit splitting Δ_{SO} with the experiment is generally very good. The electron effective masses tend to be too large after the correction. While they are underestimated by 36-67 % at the DFT level, they are overestimated by 14-67 % after the correction. The hole-effective masses are generally improved by the correction except for WZ ZnS. The hole-effective masses are generally improved by the correction with the exception of ZnS WZ. The results for HgTe have to be assessed separately since the correction changes the order of

the bands. In this case, both electron and hole effective masses are in good agreement with the experiment.

		GaAs	InP	ZnS (ZB)	ZnS (WZ)	HgTe
E_g (eV)	AEP	0.359	0.270	1.760	1.930	-1.300
	AEP+β	1.520	1.420	3.720	3.910	-0.300
	Exp.	1.520[a]	1.420[a]	3.720[a]	3.910[a]	-0.300[a,c]
$\Gamma_v - L_c$ (eV)	AEP	0.730	1.180	3.280	3.880	1.500
	AEP+β	1.730	2.220	5.170	5.520	1.230
	Exp.	1.850	1.930			
	GW			5.010[b]		1.230[c]
$\Gamma_v - X_c$ (eV)	AEP	1.090	1.610	3.500		2.870
	AEP+β	1.850	2.420	5.140		2.440
	Exp.	1.980	2.190			
	GW			4.920[b]		2.450[c]
Δ_{SO} (eV)	AEP	0.355	0.120	0.067	0.107	0.837
	AEP+β	0.399	0.110	0.064	0.096	0.856
	Exp.	0.346[a]	0.110[a]	0.064[a]	0.092[a]	1.080[a]
Δ_{CF} (meV)	AEP				27	
	AEP+β				25	
	Exp.				29[a]	
m_e^* (m_0)	AEP	0.023	0.026	0.140	0.140	0.216
	AEP+β	0.096	0.130	0.340	0.320	0.024
	Exp.	0.066[d]	0.082[e]	0.220[f]	0.280[g]	0.028[h]
m_{hh}^* (m_0)	AEP	0.285	0.366	0.765	1.596_α, 0.48_γ	0.210
	AEP+β	0.362	0.473	1.396	1.990_α, 0.61_γ	0.337
	Exp.	0.340[i]	0.450[j]	1.760[k]	1.400_α, 0.49^g_γ	0.320[l]
E_g/m_e^*	AEP	15.608	10.384	12.571	13.785	6.018
	AEP+β	15.833	10.923	10.941	12.218	12.500
	Exp.	23.030	17.317	16.909	13.964	10.714

Table 5.1: Calculated band gaps and effective masses without correction (AEP) and with correction (AEP+β) for different high symmetry points compared with experimental and *GW* results. For ZnS WZ, the subscripts α and γ for the hole effective masses indicate the reciprocal space direction [001] and [010] respectively. The superscript alphabets correspond to the data references, as follows: *a*: [141], *b*: [188], *c*: [161], *d*: [189], *e*: [190], *f*: [191], *g*: [192], *h*: [193], *i*: [194], *j*: [195], *k*: [196], *l*: [197].

5.4 Effect of the β-correction on the wavefunctions

Our correction acts as a perturbation and the modification of the non-local part of the pseudopotential leads to new eigenfunctions. It is difficult to assess whether the new wavefunctions represent an improvement as it would require high-quality self-consistent *GW* calculations. We scrutinize the extent of the modification by analyzing the wavefunction overlap and Coulomb matrix elements in QDs.

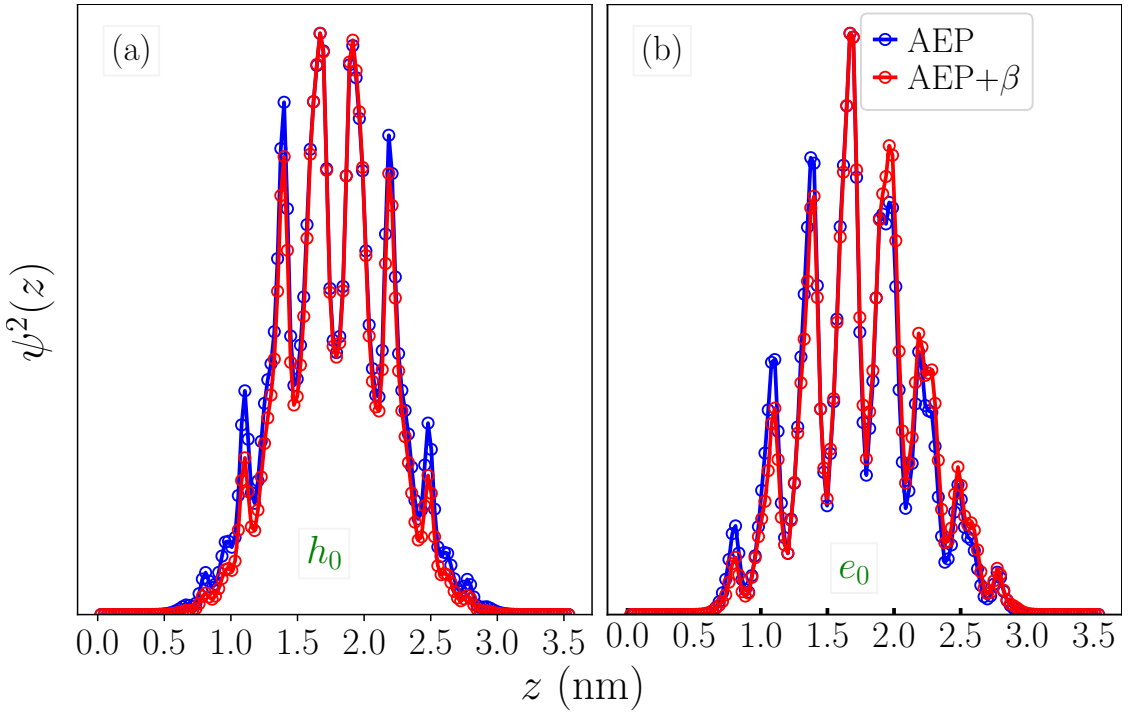

Figure 5.3: Square of the wavefunction plotted along the [001]-direction for (a) the e_0 state and (b) the h_0 state of an InP QD with diameter 1.97 nm. Reprinted from ref. [112].

5.4.1 Bulk

The overlap between the uncorrected and the corrected wavefunction is usually above 99% for the first electron (e_0) and first hole (h_0) states for all the materials (see Table 5.2 for InP). $k \cdot p$ perturbation theory offers a check on the extent of wavefunctions modification through the ratio E_g/m_e^*, shown at the bottom of Tab. 5.1, which is nearly unaffected by the correction (HgTe being a special case). Indeed, according to

Diameter (nm)	e_0	h_0
bulk	99.8	99.8
1.61	99.3	99.1
1.97	98.8	98.7
2.42	99.3	98.7
2.91	98.0	98.3
3.18	98.3	98.3
3.74	99.1	98.1

Table 5.2: Wavefunction overlap $\langle \Psi_{AEP} | \Psi_{AEP+\beta} \rangle$ (in %) for e_0 and h_0 states before and after the correction for InP bulk and QDs.

$k \cdot p$ perturbation theory [198], we have:

$$\frac{m_0}{m_e^*} \approx \frac{2}{m_0} \frac{P_{cv}^2}{E_{gap}}, \tag{5.23}$$

with $P_{cv} = \langle u_c \,|\, \hat{p} \,|\, u_v \rangle$ and the Bloch function $u_{c,v}$ for the conduction and the valence bands, suggesting a constant ratio of E_g/m_e^*. The deviation of approximately 50% observed for HgTe is due to the incorrect ordering of the Γ_6 and Γ_7 states in the AEP (LDA), as presented in Fig. 5.2.

5.4.2 QDs

The central aim of the AEPs method is to study the electronic and optical properties of larger semiconductor structures such as QDs (QDs), nanoplatelets, and more. We therefore investigate the correction's influence on QDs properties as an example, especially how the correction influences the wavefunctions. We initially compute SP energies and wavefunctions for InP NCs with different diameters (d). These calculations were performed using the LATEPP package [156] in combination with the AEP approach [67]. All calculations for the QDs were performed with non-relaxed geometries. The relaxation effects are negligible for optical properties. All the QDs considered in this work have a ZB (ZB) crystal structure. A minimum separation of 0.6 nm between periodically repeated QDs avoids electrostatic interaction among them. The InP QDs are passivated with fractional charge non-spherical pseudo-hydrogen (with charge values of 1.25H and 0.75H) potentials [148]. This ideally removes the surface or dangling bond states from the band gap. Subsequently, we determined the degree of overlap for the e_0 and the h_0 wavefunctions both before and after the correction. In Table 5.2

the overlap results are presented. For all sizes of InP dots, the change of less than 2%, between wavefunctions before and after the correction is observed. In Fig. 5.3, 1D wavefunctions along [001]-direction are plotted before and after the correction for h_0 and e_0 states. We see relatively small changes, with a tendency for the corrected wavefunctions to be more localized, in agreement with their larger effective masses after correction.

In Fig. 5.3, we show the e_0 and h_0 wavefunctions for an InP QD with 1.97 nm diameter before (blue) and after the band gap correction (red). We see relatively small changes, with a tendency for the corrected wavefunctions to be more localized, in agreement with their larger effective masses. A simple calculation of the wavefunction overlap between corrected and uncorrected wavefunctions shows deviations from the unity of less than 2% as shown in Table 5.2.

Diameter (nm)	$J_{e_0h_0}$ (AEP)	$J_{e_0h_0}$ (AEP+β)	Diff. in %
1.61	0.324	0.328	1.2
1.97	0.251	0.257	2.3
2.91	0.150	0.154	2.7
3.18	0.142	0.146	2.8
3.74	0.116	0.123	6.0
4.45	0.094	0.102	8.5

Table 5.3: Coulomb integral $J_{e_0h_0}$ (in eV) between the e_0 and the h_0 states calculated before and after the corrections for InP QDs with varying diameters.

Since the change in electron distribution (wavefunction squared) is small, we expect small variations in the energy contributions. The Coulomb integral (J) between the electron (e) and hole (h) states, a parameter intrinsically dependent on the wavefunctions [61, 63], should lead to comparably small variations. J is defined as:

$$J_{he,h'e'} = e^2 \sum_{\sigma_1,\sigma_2} \iint \frac{\psi^*_{h'}(\mathbf{r_1},\sigma_1)\,\psi^*_{e}(\mathbf{r_2},\sigma_2)\,\psi_{h}(\mathbf{r_1},\sigma_1)\,\psi_{e'}(\mathbf{r_2},\sigma_2)}{\varepsilon(\mathbf{r_1},\mathbf{r_2})\,|\mathbf{r_1}-\mathbf{r_2}|} d\mathbf{r_1} d\mathbf{r_2}, \tag{5.24}$$

where σ_1, σ_2 are spin indices, and $\varepsilon(\mathbf{r_1},\mathbf{r_2})$ is the microscopic screening function. Here, $\varepsilon(\mathbf{r_1},\mathbf{r_2})$ is accounted by employing the modified Penn-Resta-Haken approach [68, 63]. For the sake of comparison, J values with and without β-correction are calculated with the same screening function. As shown in Table 5.3, the Coulomb integrals increase

slightly (approx. 8 %) when the correction is applied. This is expected due to an increase in the effective mass and the stronger localization of the carrier. However, the effect is rather small, indicating that correction maintains wavefunction quality.

5.5 Comparison to experiments

5.5.1 Optical Band Gap

We calculate the optical band gap for InP and CdSe dots with varying d, including the correlation effects using configuration interaction [63]. We compare our results, numerically obtained both with and without our β-correction, with available experimental data, other theoretically calculated known results, and analytical spherical well approximation (both infinite and finite). For the analytical infinite (ISW) case, we have used the well-known equation:

$$E_{nl} = \frac{\hbar^2}{2m^*_{e/h}\, a^2} z^2_{nl} \tag{5.25}$$

where z_{nl} is the n-th root of the Bessel Function, a is the radius of nanocrystal and $m^*_{e/h}$ is the effective mass of the electron/hole.

For finite (FSW) case, we use the following analytical equations:

$$-k\cot(ka) = q, \qquad \textit{for } l = 0 \textit{ case}, \tag{5.26a}$$

$$k^{-2}(1 - ka\cot(ka)) = -q^{-2}(1 + qa) \quad \textit{for } l = 1 \textit{ case} \tag{5.26b}$$

with,

$$k^2 = \frac{2m^*_{e/h}}{\hbar^2}(E + V_0),$$

$$q^2 = -\frac{2m^*_{e/h}}{\hbar^2}E,$$

where V_0 is the height of the barrier's well. Similar to FSW, the solution of ISW cannot be obtained analytically. Instead, one needs to solve Eq. (5.26a) numerically or graphically (by intersection of the graphs) to determine the solution. Here we present the results with a height of 0.7 eV for the barrier as it provides a reasonable agreement

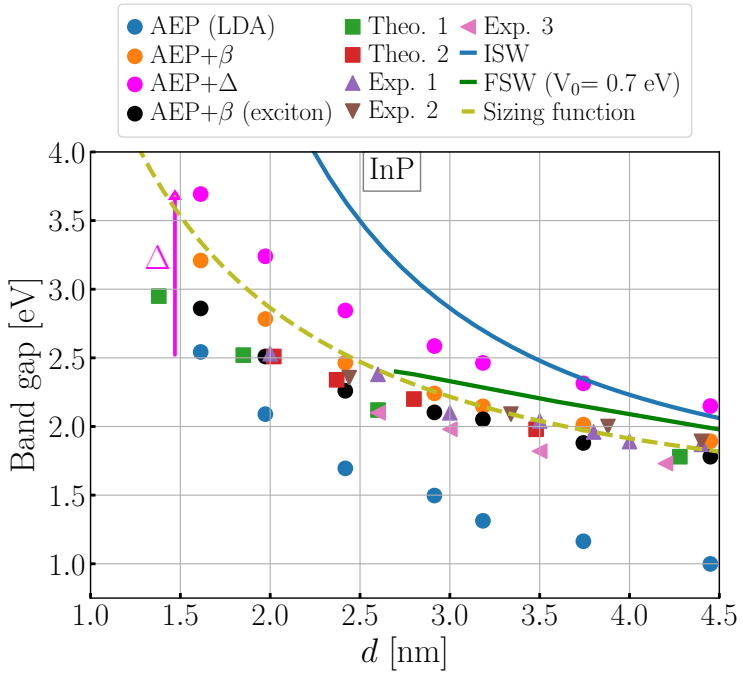

Figure 5.4: Optical band gap of ZB InP QDs obtained from calculations at different levels of theory (see text for details, the black filled circles being the final theoretical result), compared with earlier theoretical work (Theo. 1 [199], Theo. 2 [200]), with the "sizing function" from Ref. [201] and with experimental work (Exp. 1 [200], Exp. 2 [202] and Exp. 3 [203]). ISW and FSW are effective mass results for infinite and finite spherical wells, respectively.Reprinted from ref. [112].

with the experimental data.

In Fig. 5.4 we present the optical gap for InP dots and the black-filled circles are our final β-corrected exciton results including correlation effects. With different experiments (filled triangles), our β-corrected results agree very well and with other theoretical calculations (square symbols) based on the EPM approach [199, 200]. In orange-filled circles the band-gap corrected SP or the QP results are shown. The QP results do not include Coulomb $e-h$ binding energy and therefore overshoot the band gap. A simple "scissor" operator that rigidly shifts the conduction band states with respect to the valence band states by an energy Δ is also used to calculate the gap. This is a commonly adopted approximation to adjust the band gaps obtained at the LDA or GGA level. Δ is the difference between the bulk experimental band gap and the LDA (or AEP, since they yield the same results) band gap. The results are shown

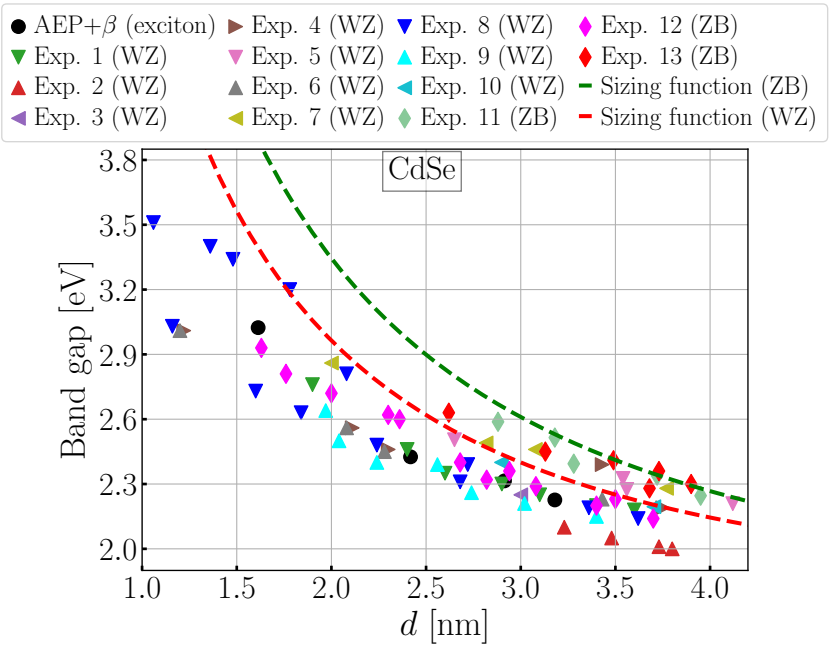

Figure 5.5: similar to Fig. 5.4 but for ZB CdSe QDs. The references corresponding to the experiment number in the figure label are as follows: 1 [204], 2 [205], 3 [206], 4 [207], 5 [201], 6 [208], 7 [209], 8 [210], 9 [211], 10 [212], 11 [201], 12 [213], and 13 [201]. Sizing function: [201]. Reprinted from ref. [112].

in magenta-filled circles. It is noticeable that the scissor operator method tends to strongly overestimate the band gap, specifically for smaller sizes. The results from the infinite square well model are shown as the solid blue line. As expected, this model significantly overestimates the band gap. On the other hand, the finite square well model (solid green line) can be made to approximately fit the experimental results by using a well depth of 0.7 eV. In the dashed line, the results for an empirical "sizing function" [201] are shown which slightly overestimates the gap as well.

In Fig. 5.5 results are presented for CdSe QDs using similar terminology. The QDs can be either in ZB or WZ structure while our theoretical results are performed for ZB structures. The theoretically calculated band gap of ZB and WZ QDs for a given diameter are usually similar [208]. However, we notice a relatively large spread of the experimental results in general, which can be attributed, e.g., to the intrinsic difficulty to asses the QD size, the crystal structure, and the organic capping environment. Our theoretical results are found within the mean value of the experimental data. The "sizing function" [201] for ZB yields larger band gap values for this size range (while it fits the results more accurately for larger QD sizes).

5.5.2 Splitting of the lowest two-electron states ("S-P"-splitting)

As our simple β-correction leads to an accurate band gap description, we anticipate an improved description of the intraband energy splittings (compared to LDA) as well. In LDA, the effective masses are significantly smaller than the experimental values. Since

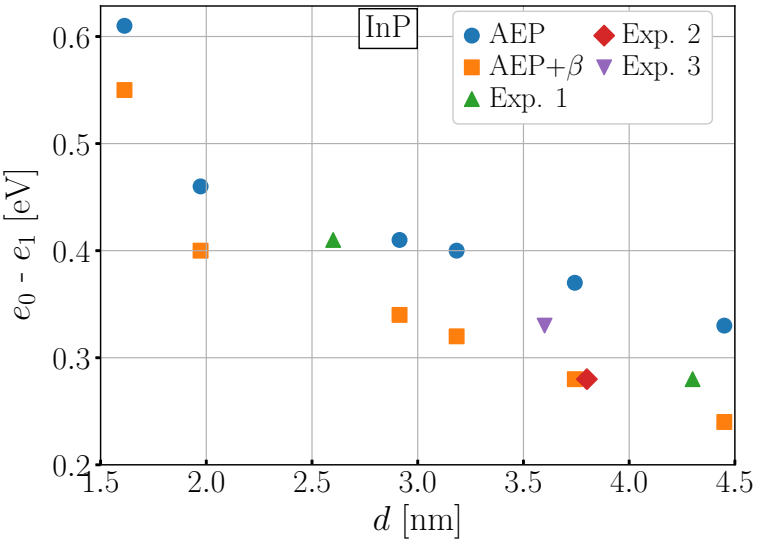

Figure 5.6: Comparison of the energy splitting between the e_0 and e_1 states for InP QDs as a function of diameter d. Experimental results Exp. 1 and Exp. 3 are from ref. [214] while Exp.2 are from ref. [215]. Reprinted from ref. [112].

the intraband S-P splitting is roughly inversely proportional to the effective mass, the S-P splitting is too large in AEP (and LDA).

In Fig. 5.6 we present the splitting of the lowest two unoccupied (e_0 and e_1) SP states (S-P splitting) for InP QDs calculated before (blue) and after (orange) β-correction along with the experimental results (red, green, violet).

The results after the β-correction (orange squares) are significantly lower and in better agreement with the experimental data. As we mentioned earlier, when we correct the gap, the effective mass tends to overshoot (become larger than the experimental value), hence lowering the S-P splitting.

5.5.3 Excitonic Fine structure splitting

As discussed in Chapter 4, the excitonic fine structure splitting (FSS) describes the small splitting of the "ground state" exciton. These small splittings are of great importance, influencing the absorption and emission properties [63, 62, 68, 20]. These

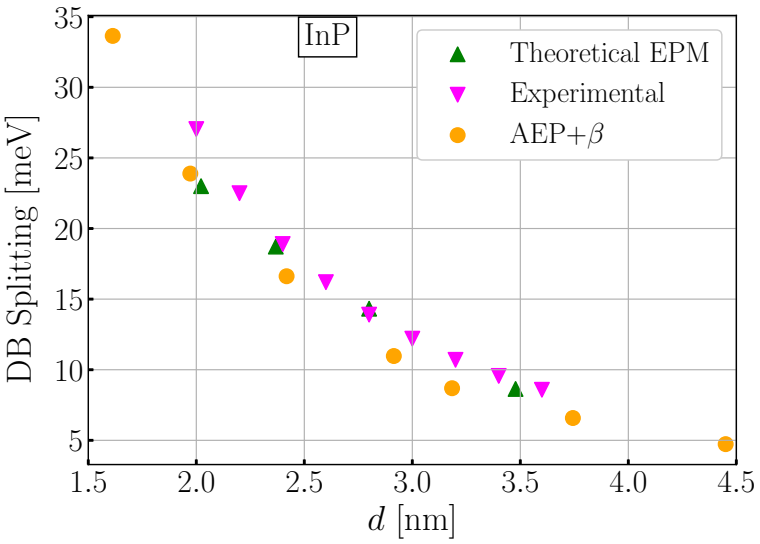

Figure 5.7: Calculated dark-bright (DB) splitting of the lowest excitonic states of InP QDs as a function of diameter. Experimental [203] and theoretical EPM [63] results are shown in magenta and green, respectively. Reprinted from ref. [112].

splittings have an atomistic origin and dependence on the symmetry of the crystal lattice (or the wavefunction). Therefore, symmetry preservation after the pseudopotential modification is crucial to ensure the correct physical picture of the system. For high-quality ZB QDs with spherical shape and T_d-symmetry, 5-fold spin-forbidden dark states and a 3-fold spin-allowed bright states both with degeneracy (see Fig. 4.4) are expected [63, 68]. As anticipated, our calculations yield 5-fold spin-forbidden dark states and threefold spin-allowed bright states and strongly indicate that our correction preserves symmetry in the system.

Experimentally, the FS of InP dots have been measured by O. Mićić *et al.* [203]. In their work, high-quality, defect-free InP QDs were synthesized that are well-suited for a direct comparison with our calculated results. This early experimental work is exceptional since ligands and atomic details of the QD surface can significantly affect the FSS [20]. Theoretically, Franceschetti *et al.* [63] have computed the FSS of InP QDs assuming an ideal surface passivation and used a high-quality atomistic EPM method. In Fig. 5.7 we show both results along with our calculations and observe a very good agreement in general.

5.6 Suggested empirical correction to DFT (LDA/GGA) results

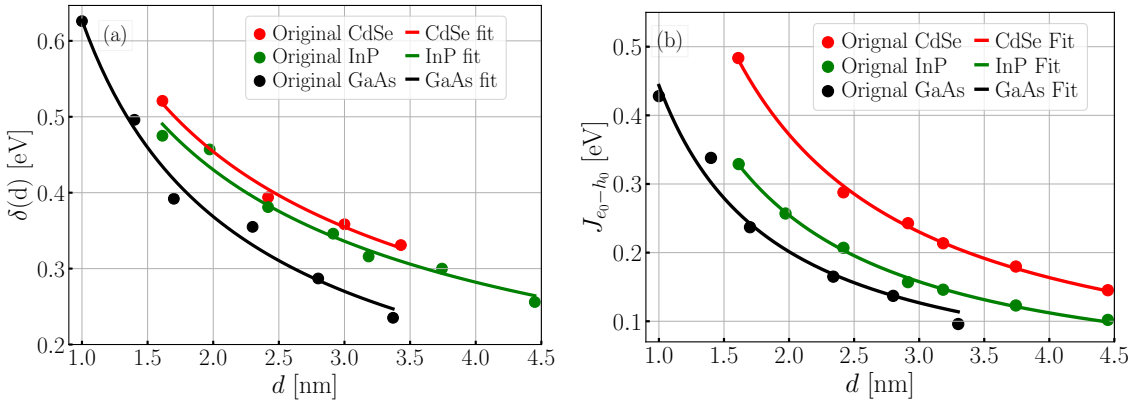

Figure 5.8: Fitted plot for (a) the empirical band gap fit $\delta(d) = \mathrm{A}/d^x$ (Eq. (7) in the main text) (b) the empirical Coulomb integrals fit $\delta J(d) = \mathrm{B}/d^y$ (Eq. (8) in the main text) for InP, CdSe and GaAs. Reprinted from ref. [112].

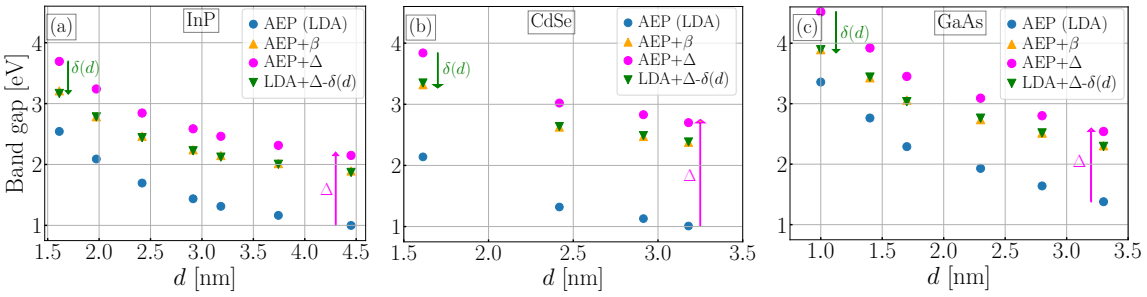

Figure 5.9: SP band gap calculated with AEP (blue dots), "β-correction" (orange triangles), using bulk scissor (magenta dots) and with the empirical fit (green triangles) for (a) InP (b) CdSe and (c) GaAs QDs. Reprinted from ref. [112].

5.6.1 QP Band Gap

Our correction method is of significant value to the LDA/GGA QDs community as we can provide a simple way to obtain the correct QP and optical gaps. As we have accurate QP and optical band gaps, as well as the LDA results, we proceed by generating a simple correcting term that can be used directly with the LDA results. In Fig. 5.8 we show the QP band gaps of InP, CdSe and GaAs QDs calculated using AEPs, AEPs+β, scissor δ and correction to be used for LDA. Our corrected gaps are

given by the AEP $+\beta$ results in orange triangles. The AEP (LDA) results in blue solid circles are significantly underestimated gaps, as commonly known. For the scissor Δ correction (magenta) we have added the bulk band gap LDA error of 1.16 eV for GaAs, 1.15 eV for InP, and 1.70 eV for CdSe to the calculated AEPs (LDA) QD band gaps.

The scissor Δ correction procedure leads to an overestimated band gap, especially for smaller QDs, which can be understood from the underestimated effective masses at the LDA level. The latter leads to an overestimation of the confinement potential and consequently overestimated band gap. To improve the LDA results, we suggest starting from the scissor-corrected LDA results and adding a size-dependent correction $\delta(d)$ with fitting parameters A and x:

$$E_{\mathrm{QPgap}}^{\mathrm{exact}} = E_{\mathrm{gap}}^{\mathrm{LDA}}(d) + \Delta - \delta(d), \quad \delta(d) = \frac{\mathrm{A}}{d^{\mathrm{x}}}, \tag{5.27}$$

where $E_{\mathrm{QPgap}}^{\mathrm{exact}}$ represents the exact QP band gap and $E_{\mathrm{gap}}^{\mathrm{LDA}}$ represents the SP band gap calculated using LDA for a QD with diameter d given in nm. We have utilized our AEP (LDA) and AEP+β results to fit $\delta(d)$, shown in Fig. 5.8, and give the parameters in Table 5.4. The empirical fit (green triangles in Fig. 5.8) and the exact results (yellow triangles) are in very good agreement for all the structures and materials.

Materials	A	x	B	y
InP	0.656	0.609	0.577	1.181
CdSe	0.692	0.608	0.846	1.185
GaAs	0.627	0.767	0.443	1.139

Table 5.4: Fitting parameters used for the empirical QP band gap correction (Eq. 5.27) and for the optical band gap correction (Eq. 5.28) for InP, CdSe and GaAs.

5.6.2 Optical Band Gap

While the QP band gap is relevant for electron affinities, work functions, and charging effect, the optical properties require to take excitonic effects into account. By using our accurate optical band gaps, calculated at the screened CI level, we can derive an empirical correction for Coulomb integrals ($\delta J(d)$), shown in Fig. 5.9, to the QP band gap obtained in the previous section.

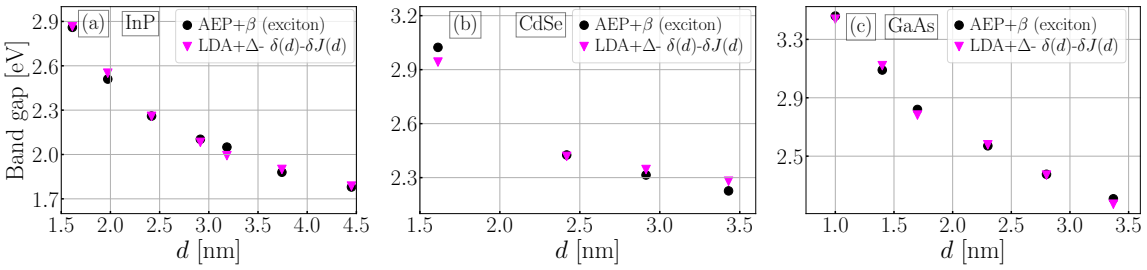

Figure 5.10: Comparison of optical band gap calculated with our β-correction, obtained with fitted results from Eq. (5.28) for (a) InP (b) CdSe and (c) GaAs QDs. Reprinted from ref. [112].

We use the simple fitting function:

$$E_{\text{gap}}^{\text{optical}}(d) = E_{\text{QPgap}}^{\text{exact}} - \delta J(d), \qquad \delta J(d) = \frac{\text{B}}{d^{\text{y}}}, \tag{5.28}$$

where B and y are fitting parameters reported in Tab. 5.4. In Fig. 5.10 we show the QD optical band gap calculated using our correction and obtained from Eq. 5.28. The exact results (black circles) and the result of the empirical fit (magenta triangles) are generally in very good agreement.

5.6.3 Size Determination of Nanocrystals

Recently, Klemeyer et al. [216] have conducted in situ experiments to investigate the development of electronic properties during the reaction leading to ZnS NC in the wurtzite phase and their subsequent transition into ZnS nanorods in the sphalerite phase. Their study revealed an electronic band gap of 4.3 eV when spherical WZ ZnS NCs are formed, with a predicted size distribution ranging from 1.8 nm to 2.2 nm. We have supplemented their work by predicting the NC size using our β-corrected band gap calculations [112]. We calculated different-sized quantum dots (QDs) that are passivated with fractional charge non-spherical pseudo-hydrogen atoms [148]. Since our SP calculations are performed at zero temperature, we include temperature effects *a posteriori* via an analytical expression for the temperature dependence of the experimental band gap presented in Ref. [217] given as:

$$E(T) = E(0) - k\left\{\frac{\rho}{2}\left[\sqrt[4]{1+\frac{\pi^2}{6}\left(\frac{4T}{\Theta_\rho}\right)^2+\left(\frac{4T}{\Theta_\rho}\right)^4}-1\right]+(1-\rho)\left[\coth\left(\frac{\Theta_\rho}{2T}\right)-1\right]\right\} \tag{5.29}$$

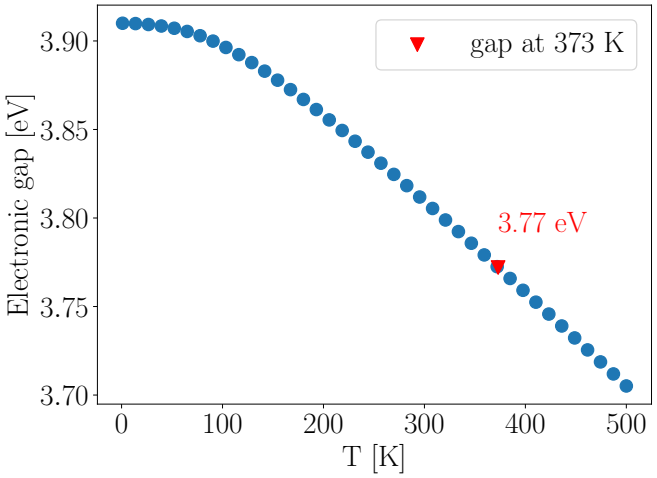

Figure 5.11: Temperature dependence of electronic band gap of bulk wurtzite ZnS calculated using an analytical expression presented by Pässler *et al.* [217] (see text for more details).

where $k = \frac{\alpha\Theta_\rho}{2}$ with $E(0) = 3.91$ eV, $\alpha = 0.548$ meV/K, $\Theta_\rho = 350$ K, $\rho = 0.389$ taken from reference [217]. This approach leads to a 138 meV red shift of the band gap from zero to room temperature (373 K), as shown in Fig. 5.11. This value has been subtracted from our calculated band gap. The results are presented in Fig. 5.12 for both T=0 K (red circles) and T=373 K (black circle). We have derived a diameter

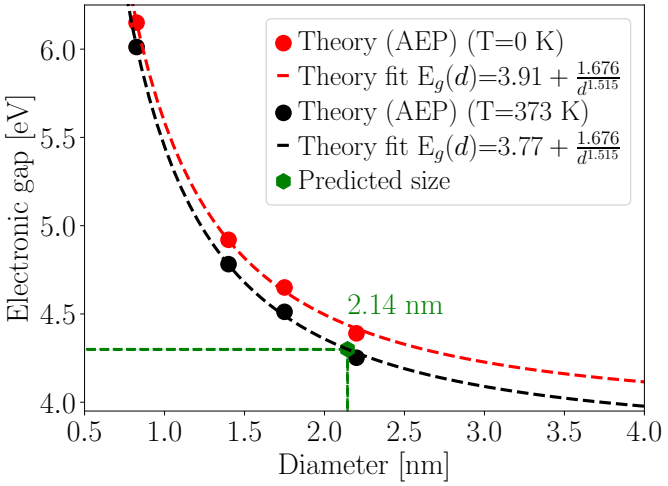

Figure 5.12: Electronic band gap of WZ ZnS QDs as a function of diameter. The filled red (black) circles are the electronic gaps at T=0 K (373 K) and the red (black) solid line is a diameter-dependent fit. The green dot shows our measured electronic gap and the ensuing dot diameter. Reprinted from ref. [216].

(d) dependent fit (black line) of the electronic gap and obtained a diameter of 2.14 nm corresponding to their measured electronic gap of 4.3 eV, which is consistent with their

dot size distribution.

In summary, we have derived an empirical correction to improve key properties of LDA-derived AEPs. This correction can improve band gaps at different high-symmetry points of the Brillouin zone and effective masses. We modify the non-local part of the pseudopotential within the atomic core region. To show the accuracy of the correction, we compare optical band gaps, intraband (e_0-e_1) splitting, Coulomb integrals, and excitonic fine structure of QDs with different diameters with the available experimental and theoretical results. Based on our correction, we drive a straightforward analytic expression to determine accurate QP and optical band gaps for InP, CdSe, and GaAs QDs from standard LDA calculation. Furthermore, we demonstrate, using wurtzite ZnS QDs as an example, how this correction can aid in accurately determining the size of nanocrystals in experiments. This is achievable when the electronic, quasiparticle, or optical gaps are measured.

Chapter 6

Electronic structure of Mn impurity in ZnS from Defect Atomic Effective Pseudopotentials

The idea and derivation of 'Atomic Effective Pseudopotentials for Large Scale Defect Calculations' were developed by W. Pfäffle et al. and remain unpublished at the time of this thesis submission. The author, **S. Kumar**, acknowledges their permission to use this methodology. All calculations and data analysis presented in this chapter were conducted by **S. Kumar**, applying the approach developed by Pfäffle et al.'s to a new material, namely Mn-doped ZnS.

In semiconductor materials, introducing transition metal (TM) atoms dopants or impurities can have both desirable and undesirable properties. While they might negatively affect some properties, they offer spin-dependent optical transitions for spintronic or spin-based quantum information [218, 219, 71, 30]. These defects are prominent for high luminescent efficiencies, and lifetime shortening [220]. One such example is Mn^{2+} defect in tetrahedrally coordinated (both ZB and WZ crystal structures) wide gap ZnS [221, 222, 223, 220]. Mn^{2+} is a charge-neutral defect in ZnS with $3d^5$ configuration. Experimentalists have observed room temperature PL transition with a strong broadening (with full width at half maximum (FWHM) of about 230 meV) around 2.12 eV, 2.10 eV, and 2.06 eV in ZnS-bulk, nanocrystals, and nanoplatelets respectively [221, 222, 223, 220]. This long-lived luminescence, lasting in the milliseconds range, results from spin flip intra Mn d-d* ($^6\mathbf{A}_1 \rightarrow {}^4\mathbf{T}_1$) transition [221, 222, 223]

(outlined in Fig. 6.1).

To understand the origin of $^6\mathbf{A}_1 \rightarrow {}^4\mathbf{T}_1$ transition and other similar transitions, spectroscopic notation for the many-body multiplets is most commonly used [224, 225, 226]. In spectroscopic notation, each multiplet term is denoted as $^{2\mathbf{S}+1}\mathbf{L_J}$ in angular momentum **L-S** coupling scheme for a multi electron system [226]. Here **L** is the total orbital angular momentum and takes on all possible values of angular momentum $\sum l_i$. **S** is the absolute value of the total electron spin $\sum s_i$. **J** is vector sum of **S** and **L**, representing the total angular momentum. 2**S**+1 is the spin multiplicity and 2**L**+1 gives the orbital degeneracy. In atoms/ions, an enormous number of possible transitions can happen but not all of these possible transitions are observed. Certain selection rules define whether the transition will be a permitted transition or a forbidden transition. For a certain transition to be allowed (in strict **L-S** coupling limits), it is necessary that $\Delta\mathbf{S}=0$, $\Delta\mathbf{L}=0, \pm1$ and $\Delta\mathbf{J}=0, \pm1$ (except **J**=0 -> **J**=0 transition). Since **J** can be readily determined from **S** and **L**, we omit **J** explicitly by using $^{2S+1}\mathbf{L}$ notation as it specifies the spin multiplicity (2**S**+1) and **L**.

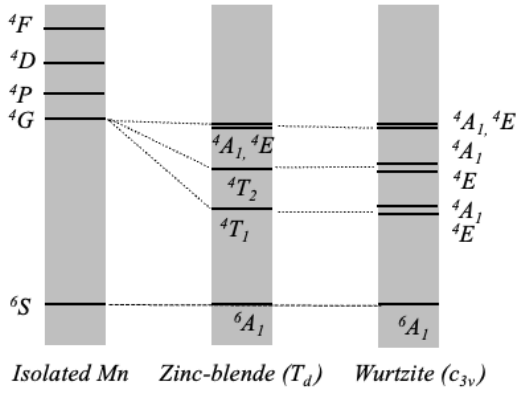

Figure 6.1: Multiplet scheme for Mn in different ZnS crystal field environments.

Fig.6.1 illustrates different many-body multiples in spectroscopic notation for free Mn^{2+} in different crystal field environments [227, 228]. As a free atom, Mn has highly degenerate valence d-orbitals due to the spherical symmetry. With five unpaired electrons, the ground state of Mn can be determined according to Hund's rule which states that:

1. Term with highest spin multiplicity (or maximum $|\mathbf{S}|$) is lowest in energy.

2. From different terms with the same spin multiplicity, the term with maximum **L** is lower in energy.

In case of 5 unpaired electron, possible $|\mathbf{S}|$ values are:

- $|\mathbf{S}|= \frac{5}{2}$: All five electron spins are aligned parallel (↑↑↑↑↑).
- $|\mathbf{S}|= \frac{3}{2}$: Four electron spins are aligned parallel and one is anti-parallel (↑↑↑↑↓).
- $|\mathbf{S}|= \frac{1}{2}$: Three electron spins are aligned parallel and two are anti-parallel (↑↑↑↓↓).

Following Hund's rule, all five electron spins align parallel (↑↑↑↑↑), resulting in a maximum spin value of $\mathbf{S} = \frac{5}{2}$. **L** is determined by summing the magnetic quantum numbers (m_l) of the occupied d-orbitals. However, for Mn in the $\mathbf{S} = \frac{5}{2}$ term with all electrons having parallel spins, each d-orbital holds one electron, and their individual m_l values cancel out (m_l= +2, +1, 0, -1, -2). Therefore, the total L for this configuration is indeed 0. As a result, the ground state of Mn is $^6\mathbf{S}$ with spin multiplicity $(2\mathbf{S}+1)$=6 and zero total orbital angular momentum ($\mathbf{L} = 0$).

The first excited state of Mn arises from a single electron spin-flip relative to the ground state ($\mathbf{S} = \frac{5}{2}$). This spin flip can occur in various d-orbitals, leading to multiple possible excited states with a total spin $\mathbf{S} = \frac{3}{2}$. For each spin-flip scenario, **L** will change depending on the initial and final m_l values of the flipped electron. For instance, flipping a spin from m_l = -2 to m_l = 0 in a d-orbital would result in a total **L** of 2. Conversely, a spin flip from m_l = -1 to m_l = +2 would lead to a total **L** of 3. The maximum L achievable with $\mathbf{S} = \frac{3}{2}$ will correspond to flipping a spin from m_l = -2 to m_l = +2 with **L** of 4. Therefore, the first excited state will be $^4\mathbf{G}$ with ninefold orbital degeneracy.

The transition from $^4\mathbf{G}$ to $^6\mathbf{S}$ is both spin and orbital forbidden i.e. $\Delta\mathbf{S} \neq 0$ and $\Delta\mathbf{L} \neq 0, \pm 1$. The states (or terms) with **L**=3,2,1,$\cdots$ will be higher in energy and have a complex energy order as Hund's rule sometimes fails [229, 230].

After doping Mn in ZnS by substituting a Zn atom, Mn is no longer in a spherical field due to the host crystal field. The Stark effect of the crystal field lifts the degeneracy of d-orbitals [227, 228, 224], as shown in Fig. 6.2. The splitting pattern of d-orbitals depends on the local environment of the host and the crystal field would affect the wavefunctions and energy structure of the impurity to form "crystal-field states" of the impurity ions [225]. As shown in Fig. 6.2, the tetrahedral crystal-field of ZnS splits Mn

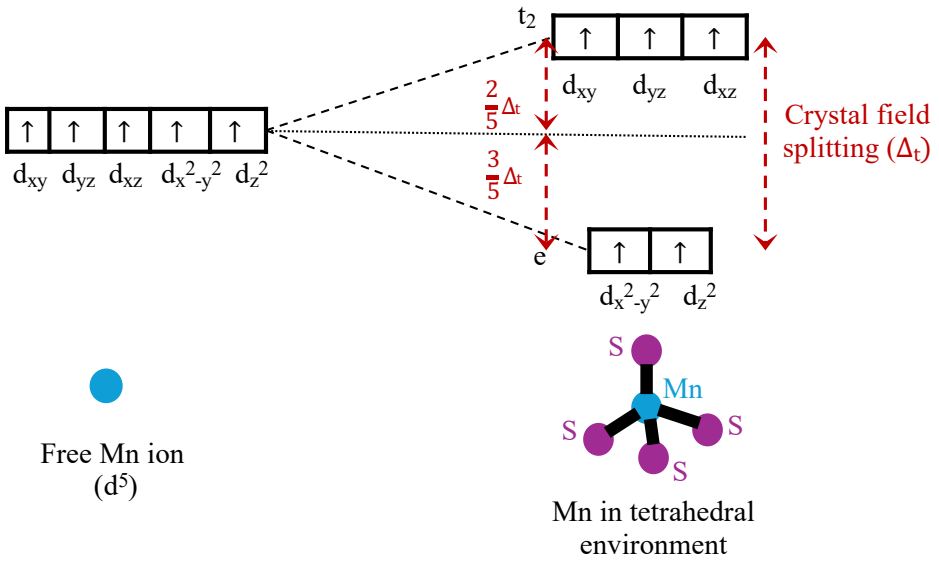

Figure 6.2: Illustration of the effect of a tetrahedral crystal field of ZnS on the energy levels of the Mn^{2+} ion. The resulting energy splitting is Δ_t.

d-orbitals into higher-energy triply degenerate t_2 consisting of d_{xy}, d_{yz}, d_{xz} and lower-energy doubly degenerate e consisting of $d_{x^2-y^2}$ and d_{z^2} orbitals. The subscript 2 in t_2 indicates that these states are symmetric with respect to the C_2 axis perpendicular to the principal C_n axis. Now, each state can be represented in terms of occupation configuration of t_2 and e levels as $t_2^m e^n$ where $n + m$ is total number of d-electrons ($n + m$=5 for Mn^{2+}). The crystal field many-body states are denoted as $^{2\mathbf{S}+1}\mathbf{D}_p$. **D** indicates the orbital degeneracy of the state with **A**: singly degenerate, **E**: doubly degenerate and **T** triply degenerate. The symbol p denotes the symmetry of the state with respect to a C_2 axis perpendicular to the principal C_n axis. A value of p = 1 indicates a symmetric state relative to the C_2 axis, while p = 2 corresponds to an unsymmetrical state. Therefore, the spin sextet $^6\mathbf{S}$ ground state of Mn, which remains unaffected by the crystal field, transforms to $^6\mathbf{A}_1$ maintaining its orbital single degeneracy character [231, 224] with configuration $t_2^3e^2$. However, the first excited state $^4\mathbf{G}$ from isolated Mn undergoes significant splitting due to the crystal field, resulting in various energy levels depending on the specific field strength (as illustrated in Fig. 6.1). In T_d symmetry, the excited state $^4\mathbf{G}$ of Mn splits in lower energy $^4\mathbf{T}_1$, and $^4\mathbf{T}_2$, $^4\mathbf{E}$ and $^4\mathbf{A}_1$ states. For c_{3v} symmetry, the lower symmetry compared to T_d further splits the originally degenerate $^4\mathbf{T}_1$ and $^4\mathbf{T}_2$ states into $^4\mathbf{A}_1$ and $^4\mathbf{E}$, respectively [232]. Any of the transitions from $^4\mathbf{T}_1$, $^4\mathbf{T}_2$, $^4\mathbf{A}_1$ and $^4\mathbf{E}$ to $^6\mathbf{A}_1$ is both spin and orbitally forbidden due to $\Delta\mathbf{S} \neq 0$ and $\Delta\mathbf{L} \neq 0, \pm 1$. As $^6\mathbf{A}_1 \rightarrow {}^4\mathbf{T}_1$ is a spin-flip transition; this is forbidden

by spin and orbital symmetry but weakly allowed due to spin-orbit coupling (SOC), hence long-lived.

Understanding symmetry-breaking effects in excited states ($^4\mathbf{T}_1$, $^4\mathbf{T}_2$, $^4\mathbf{E}_1$) via theoretical calculation could offer a better understanding of PL. *Ab initio* DFT methods are powerful and efficient theoretical approaches for studying such systems. However, they do have several limitations. Poor description of exchange and correlation at the LDA or GGA level delivers an inaccurate description of the band gap. Impurity atoms usually introduce energy levels in the band gap of the host material. An inaccurate gap will have strong consequences for localized defect states positioning them either in the valence or the conduction band instead of the gap. Alternative approaches such as hybrid functionals, self-interaction correction (SIC), LDA+U, and QP methods like *GW* are known to be more accurate compared to LDA(GGA) but are computationally too expensive. DFT also suffers limitations for open shell defects [233] as only a single configuration is used for the approximation of the many-electron wavefunction [234] and electron correlations are included through approximations. For systems where the ground state (as in our case) is well described only by more than one (nearly-)degenerate determinant, static correlation becomes important which is missing in DFT. Therefore it requires a multi-reference approach [235, 236, 71] to include all correlations and provide an accurate description of systems. Another constraint on DFT calculations might arise from system size for several defects as they require bigger supercells [237].

In the present work, we use defect AEPs derived within the group which can effectively deal with different geometries and significantly larger systems avoiding self-consistent cycles. Self-consistent cycle relaxation in defect AEPs offers a choice of calculating a desired part of the eigenvalue spectrum i.e. only calculating states around the gap including defect states. As discussed in Chapter 5, AEPs are derived using LDA (or GGA) and inherit the band gap underestimation from these functionals. To address this issue and achieve accurate experimental gaps and energy level positions, we apply β-correction, as detailed in Chapter 5. The problem of the multi-reference approach or many-body (MB) can be tackled with a screened configuration interaction approach adapted for open-shell situations [71]. In this work, we focus on the results obtained from SP calculations. Investigations into many-body effects are planned for future studies.

6.1 Analytic derivation of the impurity AEP

The derivation of the impurity/dopant AEP relies on the use of bulk AEPs which were discussed previously in Chapter 5. As derived in Eq. 5.10, the local **G**-space potential is:

$$V_{loc}(\mathbf{G}) = \frac{1}{\Omega_c} \sum_{\alpha}^{N_{species}} \sum_{n}^{N_\alpha} v_\alpha(\mathbf{G}) e^{-i\mathbf{G}.\boldsymbol{\tau}^{\alpha n}}, \tag{6.1}$$

where $v_\alpha(\mathbf{G})$ are the AEPs. To introduce the impurity (imp), we rewrite the potential explicitly for a binary cation (cat)-anion (ani) system:

$$\begin{aligned}\Omega_c V_{\rm loc}(\mathbf{G}) &= \left(\sum_n^{N_{\rm cat}} e^{-i\mathbf{G}.\boldsymbol{\tau}_{{\rm cat},n}}\right) v_{\rm cat}(\mathbf{G}) + \left(\sum_n^{N_{\rm ani}} e^{-i\mathbf{G}.\boldsymbol{\tau}_{{\rm ani},n}}\right) v_{\rm ani}(\mathbf{G}) + e^{-i\mathbf{G}.\boldsymbol{\tau}_{\rm imp}} v_{\rm imp}(\mathbf{G}), \\ &= S_c v_{\rm cat}(\mathbf{G}) + S_a v_{\rm ani}(\mathbf{G}) + S_i v_{\rm imp}(\mathbf{G}),\end{aligned} \tag{6.2}$$

where $S_{c,a,i}$ are the structure factors of the cations, anions, and of the impurity which depends only on the atomic positions. We can get the impurity AEPs, reordering the previous equation, as:

$$v_{\rm imp}(\mathbf{G}) = \frac{1}{S_i}\left[\Omega_c V_{\rm loc}(\mathbf{G}) - S_c v_{\rm cat}(\mathbf{G}) - S_a v_{\rm ani}(\mathbf{G})\right] \tag{6.3}$$

where all terms on the right-hand side are known. The impurity AEP derived this way is a complex quantity from which we keep only the real part; which corresponds to an inversion symmetric potential [148]. Similar to the bulk AEPs [67], a spherical approximation of the impurity potential i.e. $v_{\rm imp}(\mathbf{G}) = v_{\rm imp}(|\mathbf{G}|)$ is considered.

Impurity AEPs are derived by taking advantage of the centrally short-ranged nature of impurity-induced potential changes. Though these AEPs are derived from self-consistent calculations of small supercells, they can be applied non-self consistent way to bigger supercells with several thousand atoms. For spin-polarized systems, such as Mn in ZnS, the AEPs are derived based on the total potential $V^{\rm loc\uparrow}$ and $V^{\rm loc\downarrow}$ obtained via spin-polarized calculations for a bulk ZnS supercell with 256 atoms with one substitutional Mn impurity replacing one Zn atom. Therefore, $V^{loc}(\mathbf{G})$ is obtained from ABINIT package [238] with the SLDA [102] exchange-correlation functional (Troullier-Martins NCPP [155]) and a supercell with 256 atoms. The supercell dimensions were based on the experimental lattice constant, with a c/a ratio of 1.637 (where c = 0.626 nm is the lattice constant along the c-axis and a is the lattice constant in the plane

perpendicular to c). For Zn, we choose a maximum angular momentum cutoff l_{max}=2 and a local channel angular momentum l_{loc}=1 in NCPP. For S atoms, l_{max}=1 and l_{loc}=0 were set. For Mn, we set l_{loc}=0 and l_{max}=2 with 3p, 4s and 3d electrons as valence electrons. The inclusion of 3p as valance electrons was necessary to obtain correct 3d energy levels. Here we use gamma-only k-point sampling. With gamma-point sampling, though neighboring defects wavefunctions hybridization still exists, but the k-dependent occupation of the defect states is prevented. As the supercell size used in the generation of the potential increases, the effect of gamma-point sampling diminishes.

The case of SLDA self-consistent DFT solution, obtained without spin-orbit interaction, gives total potentials for spin-up and spin-down states independently, and we obtain two individual Mn impurity potentials. Although the average potential in a periodic crystal ($\mathbf{G} = \mathbf{0}$ component) is undefined, the difference between the average potentials between spin-up and spin-down is significant and defines the average spin splitting:

$$V_{\mathrm{loc}\uparrow}(\mathbf{G} = 0) - V_{\mathrm{loc}\downarrow}(\mathbf{G} = 0) = \Delta. \tag{6.4}$$

The difference Δ obtained from the DFT calculation is considered while constructing the AEPs. For the value of $v_{\mathrm{imp}}(\mathbf{G} = 0)$, we consider the value $v_{\mathrm{ani}}(\mathbf{G} = 0)$ or $v_{\mathrm{ani}}(\mathbf{G} = 0)$ depending on impurity replaces a cation or an anion (See Ref. [67] on choice of $\mathbf{G}$=0 point in binary materials). This is done not to change the bulk deformation potential taken from the host material [67]. From DFT calculations, we obtained Δ=-9.52327 Hartree which was divided evenly between the two (spin-up, spin-down) AEP potentials.

In Fig. 6.3 we show the derived Mn defect spin-up AEP. In the figure, circles are raw data points and the lines are cubic spline interpolations through these data points. The initial raw data (blue circle) and AEPs (blue line) obtained form $V_{\mathrm{loc}}(\mathbf{G} = 0)$ suffers from the error which is intrinsically carried over from the bulk AEPs [239, 240] in the region of $|\mathbf{G}|$=n$\cdot\ 2\pi\sqrt{3}/\mathrm{a}_0$ data point extraction, where n is an integer and a_0 the bulk lattice constant. As our goal for passivant AEP is not to correct the deviations existing within the bulk AEPs, we omit the data points in the vicinity of these $|\mathbf{G}|$ values, as shown in orange color. One may indeed obtain a better agreement by using these data points instead of ignoring them for a specific structure, but the transferability to the structures with other dimensions and configurations would be less accurate. Fig. 6.4 shows the final AEPs of Mn defect for the spin-up and down obtained after removal of

data points in the region of $|\mathbf{G}|$=n$\cdot$ $2\pi\sqrt{3}/a_0$ and interpolated through the raw data. The quality of obtained Mn AEPs is discussed in the next section.

6.2 Results and discussion

As a first step, we compare the SP results obtained with our derived Mn defect AEPs with with DFT (LDA) results. Fig. 6.5 shows the SP energies obtained with defect AEPs and DFT. The AEPs are derived for spin up and down channels individually as discussed in Sec. 6.1. We compare the results for both spin-up and spin-down channels separately. In Fig. 6.5, circles represent the electronic levels for the spin-up channel: red circles for DFT and black circles for the defect AEPs. Similarly, squares depict the spin-down channel states: green squares for DFT and violet squares for the defect AEPs. For a better comparison, the CBM are aligned and indicated by a dotted red line. In LDA, the energy difference between the CBM and first occupied spin-up states is 1.714 eV. This energy difference is slightly increased to 1.754 eV in AEP. The

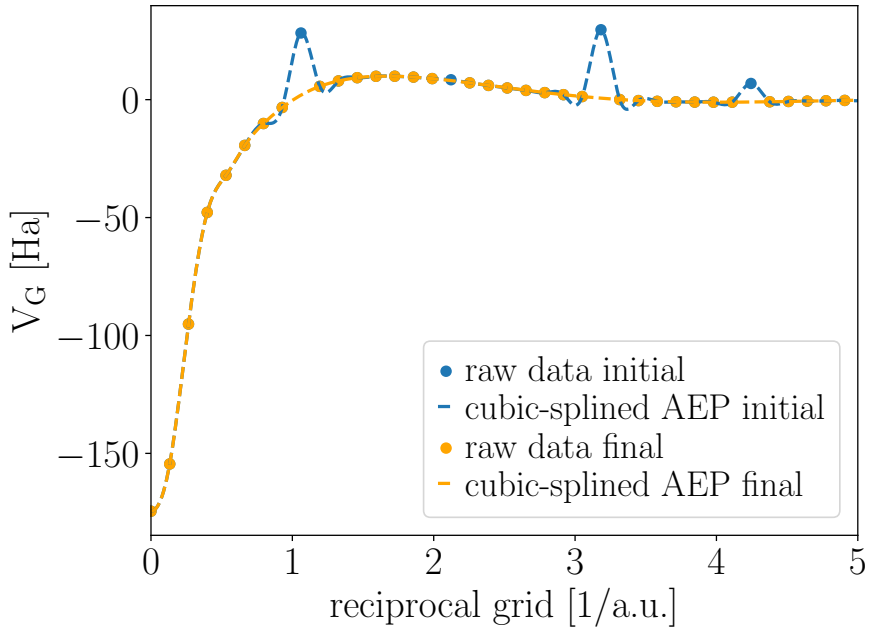

Figure 6.3: Spin-up AEP for the Mn in ZnS as a function of $|\mathbf{G}|$ in a 256 atom supercell. The initial AEP (blue circles) are with the bad point in the region of $|\mathbf{G}|$=n$\cdot$ $2\pi\sqrt{3}/a_0$, where n is an integer and a_0 the bulk lattice constant (see text). The final AEP (orange circles) is obtained after removing these bad points. The raw data points (both initial and final) are represented by colored circles, while the smoothed AEP is shown by the dashed line, obtained via cubic spline interpolation.

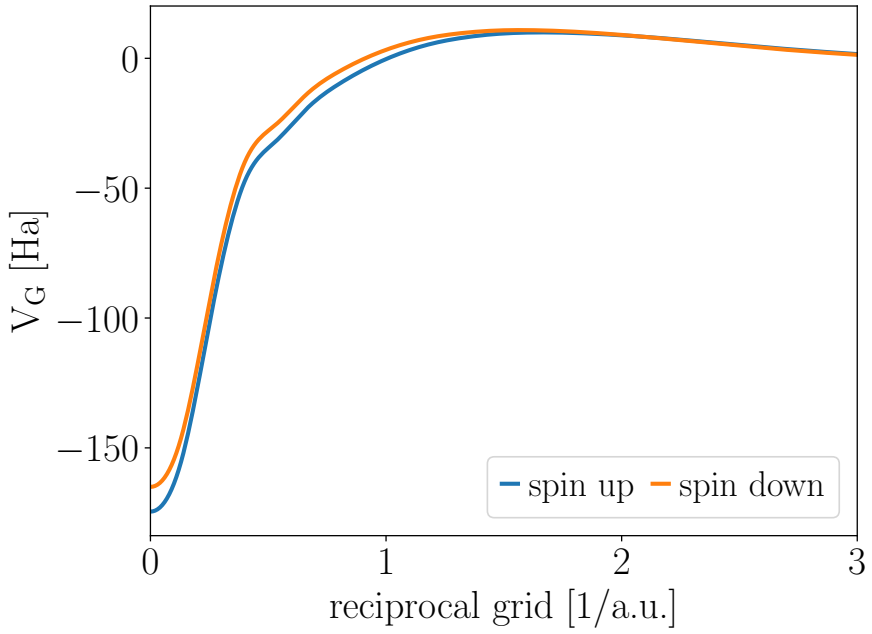

Figure 6.4: Final AEPs obtained for a Mn defect in WZ ZnS in reciprocal space derived from a 256 atom supercell.

energy difference between the CBM and the next higher conduction state shows good agreement between LDA (0.963 eV) and AEP (0.961 eV), with a minimal difference of only 0.2%. The energy difference between the CBM and the highest occupied state in the spin-down channel also shows a slight increase in AEP (1.889 eV) compared to LDA (1.80 eV). The difference in SP exchange splitting [241, 242] (shown in orange) in LDA (2.03 eV) and AEP (2.056 eV) is small, with a difference of 1.2%. The splitting between the valance states is comparatively complex. The valance states in DFT are more split compared to AEPs. These discrepancies (and overall differences) between AEP and LDA are likely due to the spherical approximation used when constructing the defect AEPs. It's important to note that these energy level splittings and differences, all within the range of 100 meV, are relatively insignificant (relative to the band gap scale). Despite these slight differences, the AEP approach demonstrates reasonable accuracy compared to the more computationally expensive DFT calculations.

Since AEPs are inherent in the LDA gap underestimation, we apply the gap correction on the ZnS levels. Fig. 6.6 shows AEPs SP band structure for bulk WZ ZnS before (blue) and after (red) the with gap correction scheme discussed in Chapter 5. The uncorrected AEP calculation yielded a band gap of 1.94 eV for WZ ZnS, significantly lower than the experimental value. Applying the gap correction with the β_l parameter (as described previously), we increase the band gap to an experimental value of 3.91 eV.

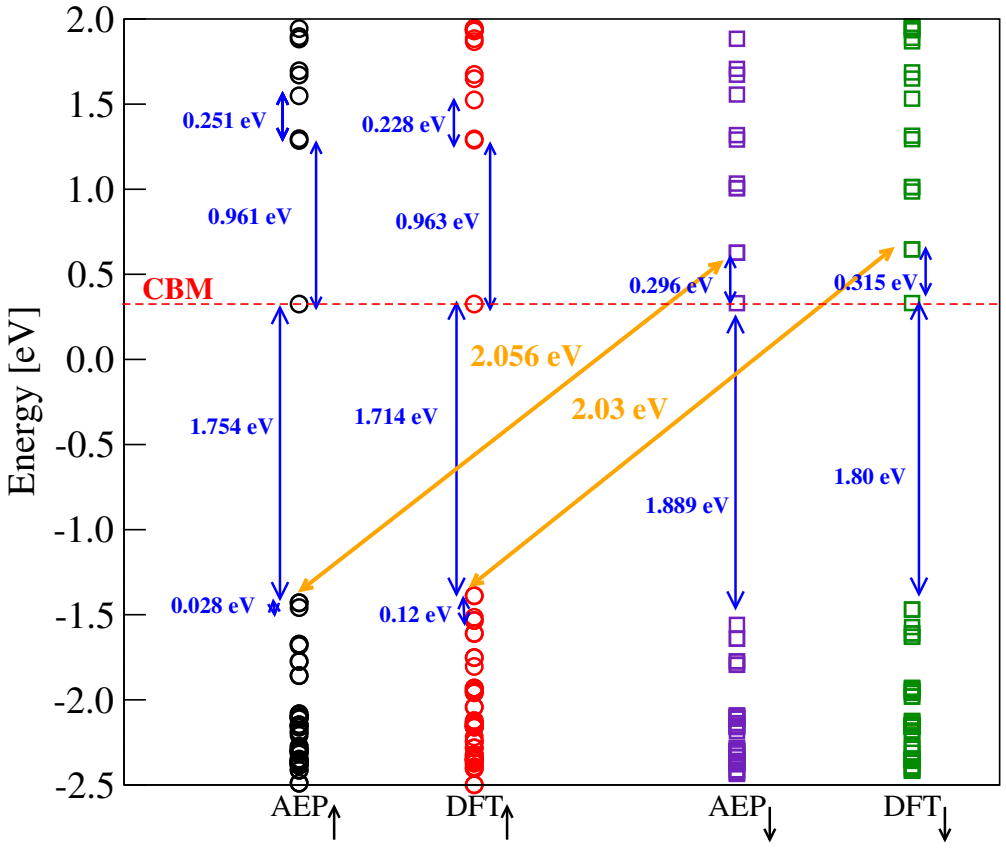

Figure 6.5: Comparison of SP energy levels obtained from derived Mn defect in ZnS AEPs and fully DFT calculations in a WZ supercell with 256 atoms.

Applying a gap correction has a significant impact on both the quantitative values and qualitative features of the energy levels, particularly near the Γ-point. This correction leads to a substantial downward shift of the VBM by over 1 eV. Therefore, correcting the gap is crucial for capturing an accurate physical picture of the electronic structure. With the importance of gap correction understood, we now explore its impact on the electronic structure of Mn in ZnS.

In Fig. 6.7 we show the SP energy levels near the band gap of bulk ZnS (WZ structure) before and after applying our gap correction method for a single Mn defect. The calculations were performed for a 256-atom supercell containing a single Mn impurity. Markers of the same color correspond to the same energy level before and after gap correction. Circles represent the host ZnS levels, while triangles represent the Mn d-levels. We defer the presentation of wavefunction squared plots for identifying the Mn-d levels until later in Fig. 6.12. These plots will be presented after all initial test calculations are complete to ensure a clear distinction between the initial test results and the final analysis of the Mn-d states. The uncorrected band gap, represented by

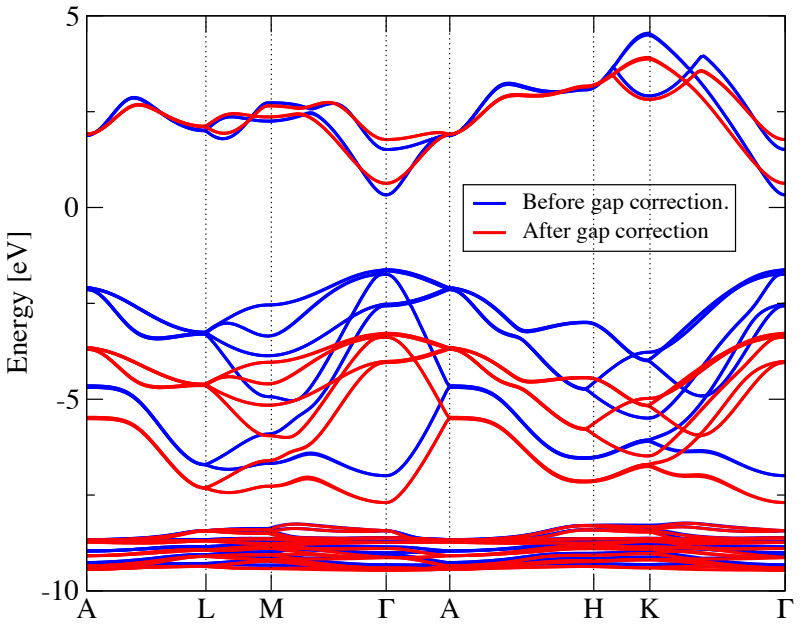

Figure 6.6: SP band structure of bulk WZ ZnS before (blue) and after (red) the gap correction (discussed in Chapter 5) calculated with AEPs.

the energy difference between the circles, is 1.94 eV for both spin states. Prior to the gap correction, the electronic structure shows three spin-up (green triangle) d-states positioned above the VBM (represented by the blue circle) of the host material. Interestingly, two additional spin-up d-states (orange triangle) reside slightly below the VBM. In contrast, for the spin-down channel, no d-states are found within the band gap. However, after applying the gap correction (or level correction), the distribution of d-states is significantly changed. As VBM moves down with correction, all spin-up d-states become positioned within the band gap. In the spin-down channel, the correction moves the CBM higher in energy and brings two d-states (pink triangle) below the CBM (represented by the brown circle). We therefore focus solely on the gap-corrected energy levels as they match with the experimental known transition between d-d levels being well below the host ZnS transition in energy.

We now shift our focus to understanding how Mn substitution affects the structural properties of the material. Due to its larger size compared to Zn, substituting a Zn atom with Mn can distort the surrounding crystal structure, particularly bond lengths and angles around the Mn atom. This distortion can be localized near the dopant or extend outwards, influencing the electronic energy levels. Therefore, quantifying the impact of this structural distortion on the electronic structure is crucial

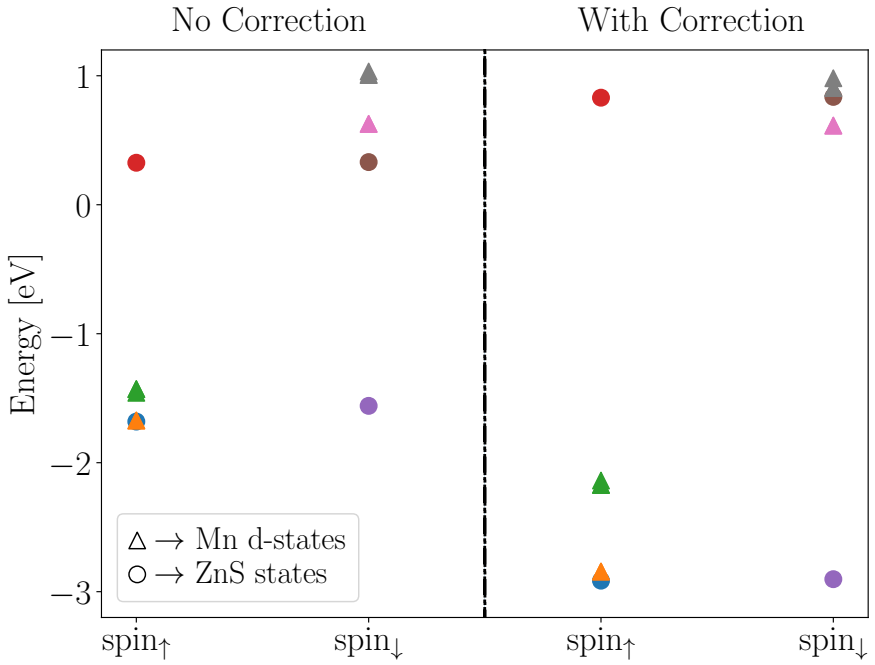

Figure 6.7: SP energy levels near the band gap for spin-polarized calculations of a 256-atom bulk ZnS supercell containing a single Mn impurity. The results are shown with (right) and without (left) gap correction. Triangles represent the Mn 3d levels, while circles represent the ZnS host levels. Markers of the same color correspond to the same energy level before and after gap correction.

for accurate understanding. Since Mn^{2+} has five unpaired d-electrons, it leads to a strong spin-polarized state where the spins of these electrons tend to be aligned in the same direction. Consequently, all calculations presented in this chapter are spin-polarized only unless explicitly stated otherwise. Due to the separation of spin-up and spin-down SP energies obtained from our spin-polarized calculations, we present them separately throughout this work. We use spin-LDA (SLDA) functional in the ABINIT software package [238] to calculate SP energies for a 256-atom supercell. This supercell is obtained by relaxing the atomic positions after introducing the Mn impurity. The calculations are performed only at the Brillouin zone center (Γ-point). Fig. 6.8 illustrates the impact of atomic relaxation on bond lengths within the calculated supercell. The color map represents the percentage change in bond lengths relative to the ideal ZnS. The position of the Mn atom, which replaced a Zn atom, is highlighted in magenta. A closer inspection shows a significant relaxation primarily localized around the Mn substitution. This is apparent with the noticeable change (approximately 6%) in the bond lengths of the Mn-S bond fragment. Conversely, Zn-S bonds further away from the Mn atom have minimal to no change. This suggests that the Mn substitution

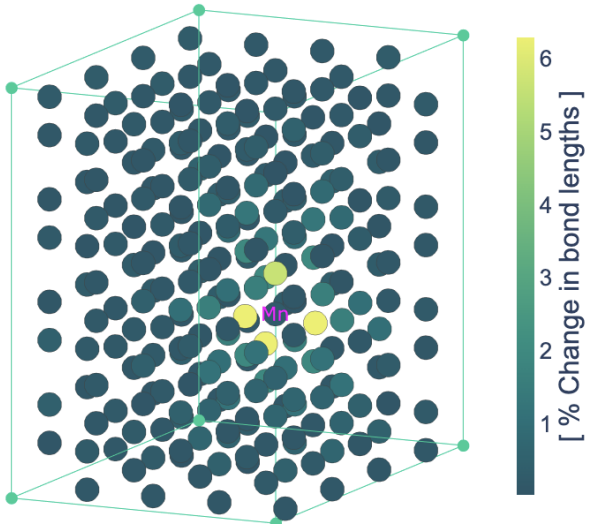

Figure 6.8: Percentage change in bond lengths after full relaxation. The color map shows the percentage change in bond lengths within a 256-atom supercell after full relaxation of ionic positions. The reference structure is ideal ZnS. The position of the Mn atom, which has been substituted for a Zn atom, is highlighted in magenta.

primarily induces localized structural distortions around Mn and its four nearest sulfur neighbors (Mn-4S fragment), with a slight impact on the bulk structure of the host ZnS material.

Since relaxation mainly occurs in the Mn-4S fragment region, we can potentially exploit this localization to simplify the calculations. Relaxing only the Mn-4S fragment offers a computationally efficient alternative to relaxing the entire structure, provided the changes in electronic energies are comparable between both approaches (full relaxation vs. Mn-4S relaxation). We therefore have considered three scenarios to investigate the relaxation effects on SP energies: (a) frozen structure where the atomic positions are fixed, neglecting any relaxation due to Mn substitution. This provides a baseline for the impact of structural changes, (b) full relaxation where all atomic positions are allowed to relax to minimize the system's energy. This allows for the most significant structural changes and reflects the fully distorted configuration and (c) Mn-4S fragment relaxation where relaxation of only the Mn atom and its four nearest-neighbor sulfur (S) atoms is done.

In Fig. 6.9, the calculated SP energies for the 256-atom supercell for different relaxation cases are presented. Black circles indicate the spin-up channel, while red circles represent the spin-down channel for no relaxation (NR) of atomic positions. Squares denote the SP energies obtained after allowing all atoms to fully relax. These results correspond to the configuration for both spin-up (green) and spin-down (magenta)

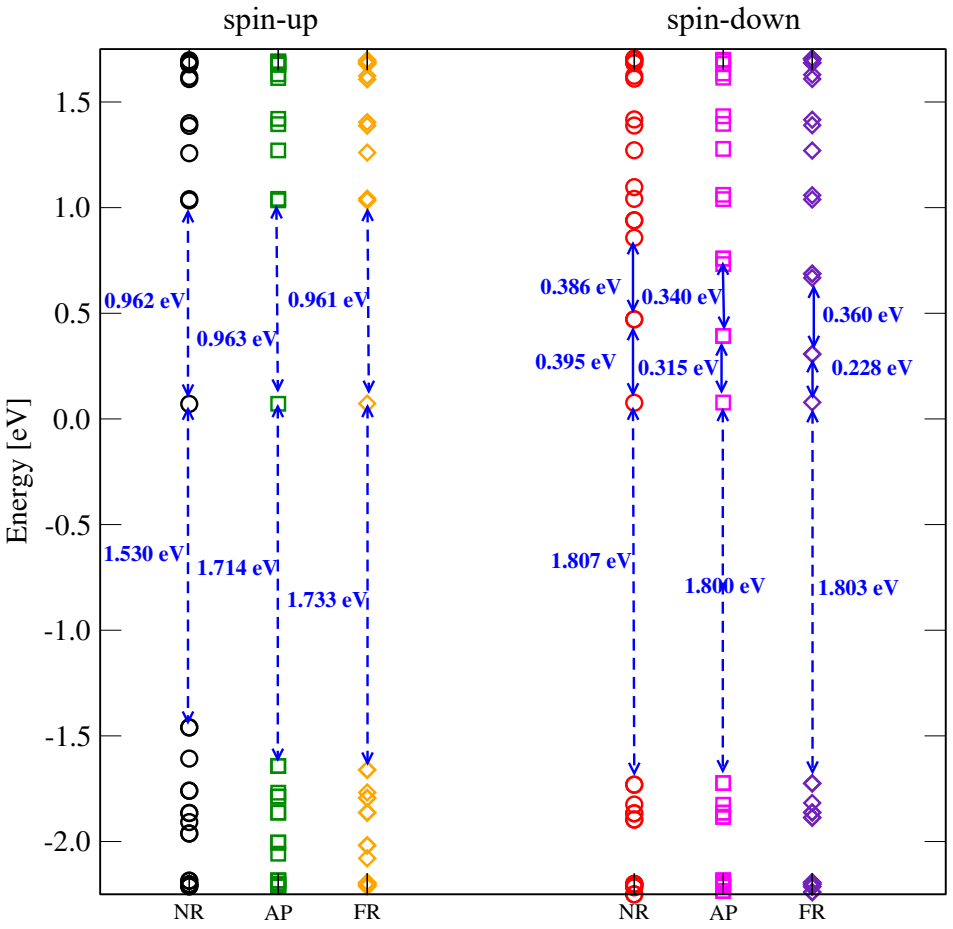

Figure 6.9: Effect of relaxation on energy levels in a WZ structure supercell with 256 atoms. NR: No relaxation; AP: Full atomic position relaxation; FR: Mn-4S fragment relaxation.

channels. Orange diamonds (spin-up) and violet diamonds (spin-down) represent the SP energies when only the Mn atom and its four nearest-neighbor sulfur (S) atoms are allowed to relax.

We begin by analyzing the SP energies for the spin-up channel across all relaxation scenarios: No Relaxation (NR), Full Relaxation (AP), and Mn-4S Fragment Relaxation (FR). The band gap for the NR case is 1.530 eV. Relaxation significantly increases the band gap to 1.714 eV for the AP case and 1.733 eV for the FR case. The difference between AP and FR (19 meV) is negligible, suggesting a minimal impact on the band gap from relaxing atoms beyond the Mn-4S fragment. While the conduction band position shows slight changes, the valence band moves significantly towards the lower energy upon relaxation. Other higher-lying conduction states remain relatively unchanged. Notably, valence states exhibit a clear dependence on relaxation, with both AP and

FR producing similar results. This behavior is due to the presence of Mn up states lying close to the VBM. These Mn states hybridize with the VBM states, leading to a downward shift of the valence band states. For the spin-down channel, the major changes are observed in the states above the CBM. Relaxation alters the splittings between the next five levels, while the VBM states remain largely unaltered. These changes likely arise due to the influence of Mn down states located near the CBM.

The structural relaxation results have a key finding: relaxation primarily occurs in the vicinity of the Mn dopant, significantly influencing the electronic energy levels. Notably, relaxing only the Mn-4S fragment yields sufficiently accurate results, making this a viable approach for computationally efficient calculations involving large structures with thousands of atoms.

We now address the issue of spurious interactions arising from the use of periodic boundary conditions. If the separation between periodically repeated defects is too small, the electronic structure of an isolated defect becomes distorted. This occurs because the deep energy levels within the band gap can interact and form extended energy bands with a finite dispersion. By converging the supercell size in which the Mn defect is placed, we aim to eliminate these interactions and obtain a more accurate description of the defect's behavior. Fig. 6.10 illustrates the convergence behavior of SP energies around the band gap of Mn-doped WZ ZnS with respect to the supercell size. The x-axis represents the supercell size in multiples of the bulk 4-atom unit cell of WZ ZnS. In the figure, the Mn d-states are shown by triangles, while the host ZnS states are shown by circles. The VBM and CBM of the host ZnS are denoted by blue and orange circles, respectively. For clarity, spin-up and spin-down states are presented together for each supercell size. It is important to note that these results are based on unrelaxed supercells. This choice is justified because relaxation effects are expected to be highly localized around the Mn-S bonding region and will have a negligible influence on the overall convergence trends observed with varying supercell sizes. We investigated the convergence of various energy splittings with respect to supercell size. The band gap of ZnS (represented by the energy difference between the orange and blue circles) decreases by 24 meV when increasing the supercell size from 2x2x2 to 6x6x6 for both spin-up and spin-down channels. This decrease becomes considerably smaller (only 4 meV) upon further enlargement to an 8x8x8 supercell. In the spin-up channel, a qualitative change in the ordering of Mn d-energy levels (shown in triangles) is observed as the supercell size increases. In the 2x2x2 supercell, the lowest energy

d-states are doubly degenerate (2x) followed by a singly degenerate state (1x) at a higher energy level. Finally, the highest energy d-states are again doubly degenerate (2x). However, for supercells of 4x4x4 and larger, the lowest and middle energy d-states are both doubly degenerate (2x each), while the highest energy state becomes singly degenerate (1x). The energy level splitting between the two higher energy, doubly degenerate (2x) d-states (represented in magenta) and the singly degenerate (1x) d-state (represented in teal) shows a quick convergence when increasing the supercell size from 4x4x4 to 8x8x8. In contrast, the convergence of the splitting between the two lower energy, doubly degenerate (2x) d-states is somewhat slower. Here, a 9% change in the splitting is observed between 6x6x6 and 8x8x8 supercells. This suggests that a slightly larger supercell size might be necessary for a fully converged description of these specific d-states. In the spin-down channel, the energy levels of the Mn d-states show fast convergence with respect to supercell size. When increasing the supercell size from 4x4x4 to 8x8x8, the maximum change observed in any state's energy is on

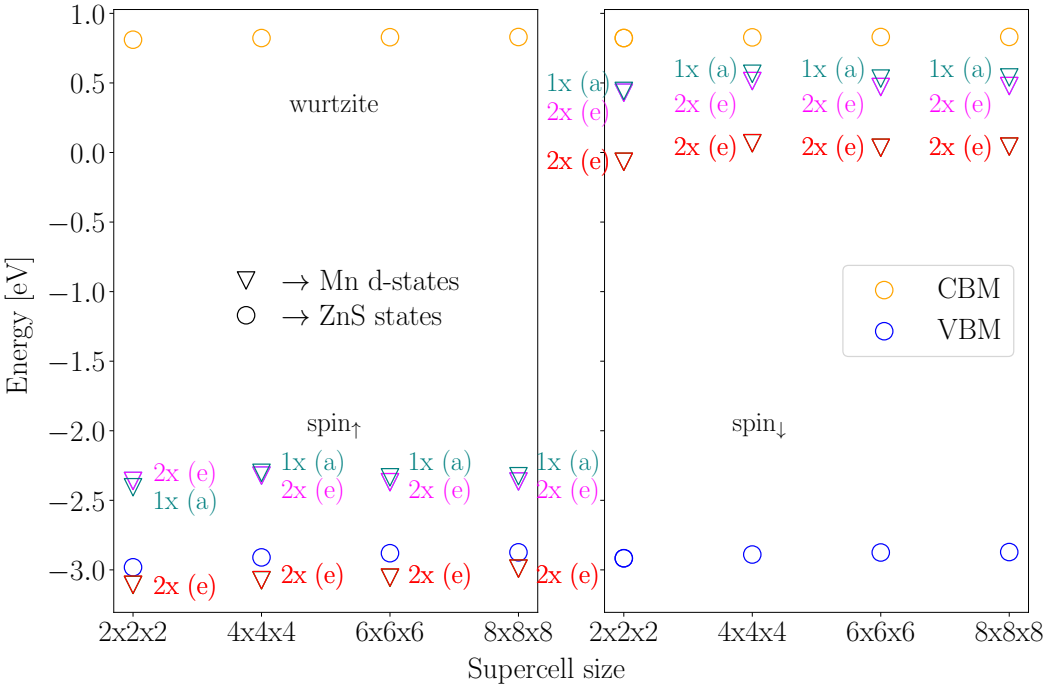

Figure 6.10: SP energy levels with respect to supercell size for a system containing a single Mn impurity embedded in bulk WZ ZnS. The results are presented after applying a gap correction to the host ZnS electronic structure. Circles represent the SP states of ZnS, while triangles represent the Mn d-states. For the Mn d-states, their degeneracy is indicated by both a number (e.g., "2x") and a corresponding symbol (e.g., e for doubly degenerate states).

the order of 5%. The energy difference between spin-up and spin-down Mn d-states (SP exchange splitting), is changed by less than 1 meV when increasing the supercell size from 4x4x4 to 8x8x8. This excellent convergence suggests that a 6x6x6 supercell is sufficient for capturing the essential electronic structure features of our interest for further calculations. The convergence of Mn in bulk ZB ZnS supercell is presented in the appendix.

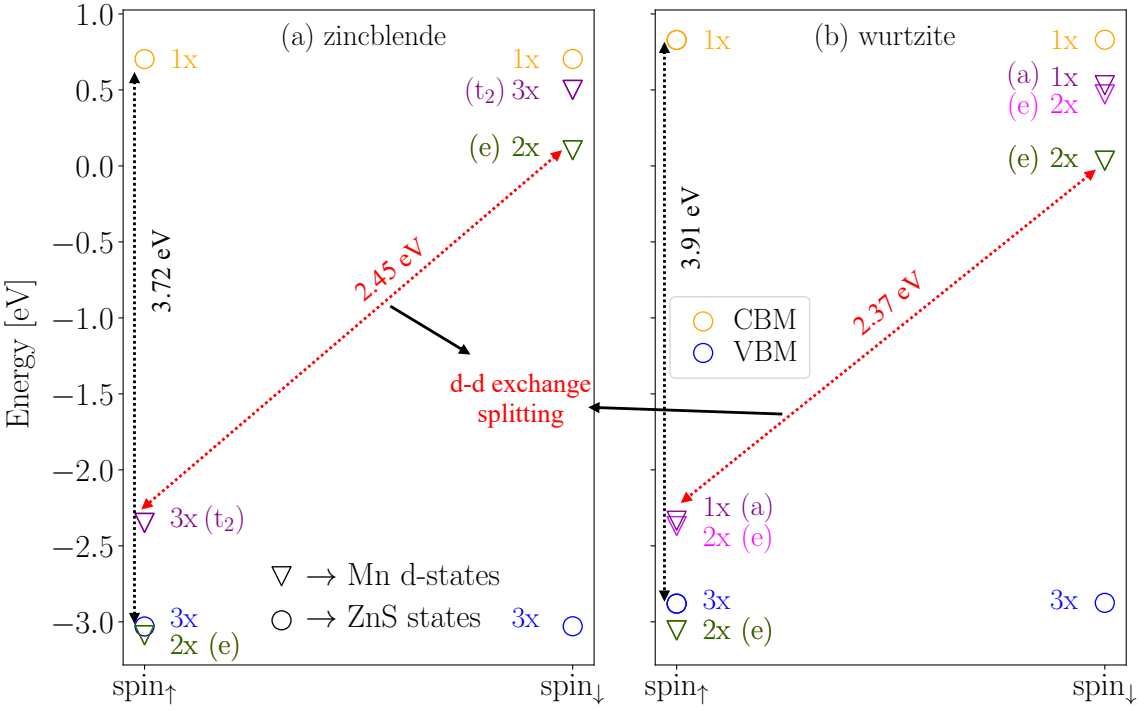

Figure 6.11: SP energy levels around the gap for spin-polarized calculations after gap correction for bulk (a) ZB (b) WZ ZnS with a single Mn impurity. Results are compared with converged supercell size for both structures. For the Mn d-states, their degeneracy is indicated by both a number (e.g., "2x") and a corresponding symbol (e.g., e for doubly degenerate states).

In Fig. 6.11, we present the calculated SP energy levels surrounding the band gap for fully converged supercells of ZnS with Mn impurities in both ZB and WZ crystal structures. In the figure, Mn levels are depicted as triangles, while the host ZnS VBM and CBM states are represented by blue and orange circles, respectively. The dashed black line indicates the host ZnS band gap, while the red dashed line represents the SP exchange splitting [242, 241] between the Mn up and down spin states. The degeneracy of the different states is highlighted in the same color as their origin marker. As the calculations are spin-polarized, we have plotted the energy levels separately for both

up and down spin channels. In the case of ZnS with a ZB crystal structure, the VBM is triply degenerate for both spin-up and spin-down channels. Interestingly, the spin-up VBM sits at a slightly higher energy level (-3.030 eV) compared to the spin-down VBM (-3.028 eV). This small energy difference of only 2 meV arises due to the SP exchange interactions. However, the degeneracy remains largely unaffected because the VBM originates from fully occupied p-orbitals, lacking unpaired electrons that could contribute to a significant spin splitting. Unlike the triply degenerate VBM, the CBM state is singly degenerate for both spin-up and spin-down channels. This difference arises due to the origin of the states. The CBM originates from the Zn s-orbital, which can only accommodate two electrons. A slight energy difference (around 0.7 meV) exists between spin-up and spin-down CBM due to SP exchange. Considering the presence of five unpaired d-electrons in Mn, we observe a significant exchange splitting between the spin-up and spin-down states. The spin-up states of Mn lie closer to the ZnS VBM while the spin-down states lie closer to the ZnS CBM. The SP exchange splitting between the spin-up and spin-down states of Mn in ZnS (marked by the dashed red line) has a splitting of 2.45 eV. This value (2.45 eV) is significantly lower compared to the exchange splitting observed in an isolated Mn atom, which we calculated to be around 5 eV at the LDA level. The tetrahedral crystal field in ZnS splits the Mn d-orbitals. This splitting has a significant energy difference (739 meV) between the triply degenerate t_2 states (located at -2.34 eV) and the doubly degenerate e-states (located at -3.08 eV) for the spin-up channel. These t_2 states reside within the band gap, while the e-states are positioned slightly below the VBM by 57 meV. The spin-down channel shows a similar crystal field splitting pattern between the t_2 and e-states. However, the crucial difference lies in their overall position relative to the band edges. All spin-down states are located within the band gap, with both t_2 (0.50 eV) and e (0.103 eV) levels lying well below the CBM by 203 meV. The spin-down t_2-e splitting (397 meV) is comparatively smaller compared to the spin-up channel. This disparity in t_2-e splitting between spin channels is due to stronger hybridization between the Mn spin-up d-orbitals and the host ZnS states. Similar observations of such spin-dependent hybridization have been reported in other Mn-doped semiconductor systems, such as Mn in GaAs. In the WZ ZnS crystal structure, the presence of Mn introduces some major differences compared to the ZB arrangement. These differences arise from an internal crystal field within ZnS, resulting from slightly elongated bond lengths along the z-axis in the WZ structure. This additional crystal field affects

both the energy levels of ZnS and the d-levels of Mn. In the WZ case, VBM is no

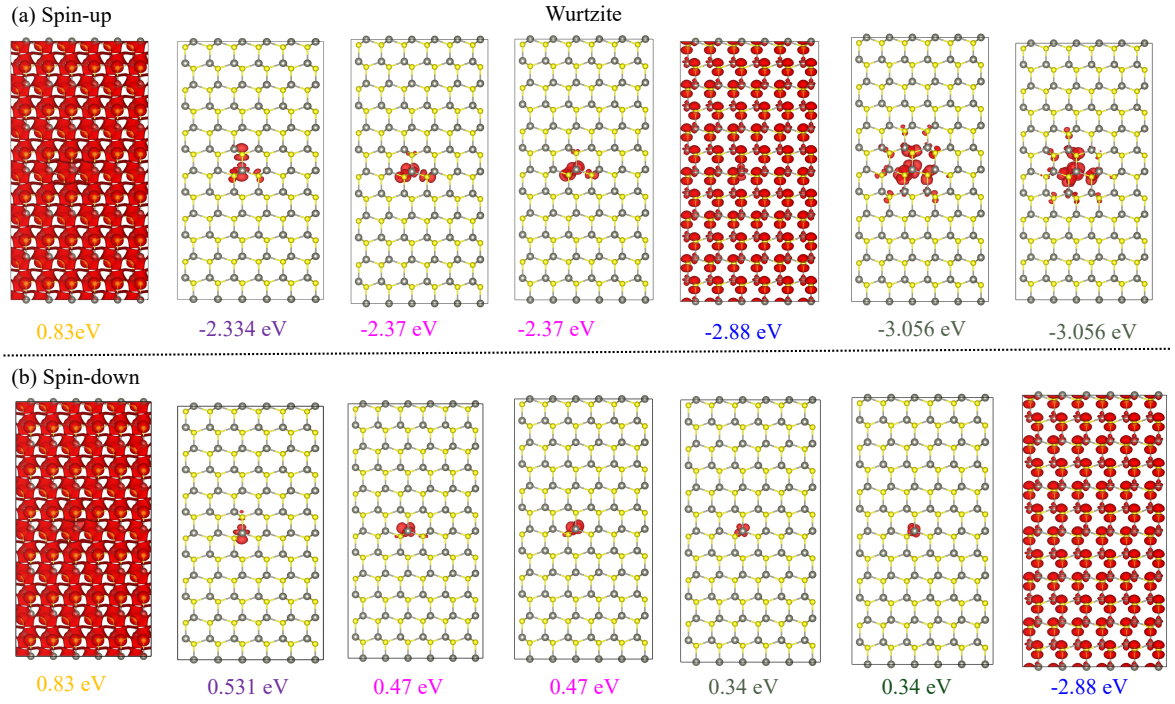

Figure 6.12: Wavefunction squared (in red) plots with 75% state density for SP levels around the gap in bulk WZ ZnS with a single Mn impurity: (a) spin-up and (b) spin-down states. These states correspond to the levels plotted in Fig. 6.11(b) after spin-polarized calculations and gap correction. Each state's corresponding energy value is marked with the same color as its data point in Fig. 6.11(b), indicating the specific state to which the wavefunction plot belongs.

longer triply degenerate for both spin channels due to the internal crystal field of the WZ structure. While the e channel (in green color) remains doubly degenerate, the t2 channel splits into double degenerate states e (magenta circles) and a singly degenerate state (purple circle). The crystal field splitting between both e-states is similar to the ZB counterpart's 739 meV for the spin-up channel. Similarly in the spin-down, the t2 states of ZB split into double degenerate states e and singly degenerate state a in the case of WZ structure. Here, the crystal field splitting between the two e state channel is slightly lower than the ZB's 397 meV likely as a result of stronger hybridization in the ZB structure. Figure 6.12 presents the squared wavefunctions corresponding to the electronic states identified in Figure 6.11(b). Each state's energy value (obtained from Figure 6.11(b)) is matched to its corresponding wavefunction plot by using the same color. This color-coding scheme allows for easy identification of the state associated with each wavefunction. As expected, the host ZnS VBM and CBM) states (labeled

in orange and blue, respectively) are delocalized throughout the entire structure. In contrast, the Mn d-states show strong localization around the Mn atom, highlighting the deep defect nature of Mn in ZnS.

In summary, we have derived a defect/impurity AEPs to calculate the electronic structure of Mn impurity in ZnS using both ZB and WZ crystal structures. Our comparison of single particle results shows that derived defect AEPs provide good agreement with the DFT calculations. Our calculations highlight that the relaxation around the Mn impurity increases the band gap and just relaxing the Mn-4S fragment is a good approximation to reduce the computational cost for larger supercell calculations. Furthermore, applying our gap correction method placed the Mn defect states within the band gap, which was not achievable with the uncorrected AEPs (LDA level). These corrected energy levels make the way for future calculations using windowed screening CI to explore the many-body multiplets associated with the Mn impurity.

Summary and Outlook

This thesis is aimed at the understanding of excitonic and vibrational properties in various nanostructures through *ab initio* and empirical methods. This study has revealed several key findings across different nanostructures, emphasizing the impact of surface effects, alloying, and impurity incorporation on their optical and electronic properties.

Based on state-of-the-art *ab initio* DFT, we have calculated the Raman spectra of CdSe nanoclusters and QDs with various realistic surface passivations. Based on our results, we identify an intense Raman signal at approximately 230 cm^{-1}, corresponding precisely to the frequency where the debated HFS is experimentally measured. This signal corresponds to the stretching vibration of a defective twofold coordinated Se atom. The Se defect atom is bonded to two inequivalent Cd atoms, one being threefold and the other fourfold coordinated. We note that that the inequivalence of the two bonds results in an asymmetric geometry and a highly intense Raman signal. The arrangement and type of L-type ligands (TOPO or MA) affect this inequivalence, thereby affecting the intensity of the signal. However, the signal persists with significant intensity in all scenarios. To compare with experimental observations, which reported the disappearance of the HFS after the growth of a protective shell, we constructed a core/shell structure and observed the same phenomenon. Accordingly, the signal disappears in defect-free (magic size cluster) structures, making it a fingerprint for identifying defective versus non-defective structures. More generally, we observe that the Raman signal in the optical vibrational region is activated when realistic, partly reconstructed, L-type ligand-protected surfaces are considered. In contrast, QDs modeled with idealized passivation, and thus higher symmetry, exhibit comparatively weaker Raman signals in this spectral region.

Using a fully atomistic single-particle EPM in combination with CI, the exciton fine structure of alloyed $Zn_{1-x}Cd_xSe$ QDs and core-shell structures where a CdS rod is grown on top of these QDs is calculated. Our calculations of single-particle results have shown a strong bowing of the band gap of $Zn_{1-x}Cd_xSe$, observed both in bulk and

in various QDs sizes. We have established that the strain induced by lattice mismatch in alloys leads to crystal field splitting of single-particle levels which varies with the concentration of the alloy. In alloyed QDs, the lowest $e-h$ pair (without the Coulomb and exchange interaction) is no longer eightfold degenerate as in pure QDs. This is a consequence of crystal-field splitting in two highest occupied single-particle levels h_0 and h_1. This results in qualitatively different excitonic fine structure for alloyed QDs compared to the pure QDs. In pure dots, the lowest exciton is split in fivefold degenerate dark and threefold degenerate bright state. In contrast, for alloyed QDs, the lowest exciton splits into two crystal-field split manifolds, each containing four states (4x and 4x). These manifolds experience further splitting due to exchange interaction and these splittings vary strongly with alloy concentration. Based on these splittings, we propose an explanation for the multi-exponential PL decay observed in experiments for alloyed QDs and alloyed dot-in-rod structures.

In order to improve the key properties of LDA-derived AEP, which can calculate the electronic structure of up to 50,000 atoms, we have developed an empirical correction. The empirical correction modifies the non-local part of the pseudopotential within the atomic core region and can improve the band gaps, and effective masses. With our correction, a good agreement with experimental and theoretical results for optical band gaps, intraband splitting, Coulomb integrals, and excitonic fine structures in QDs is achieved. We have offered a straightforward way to determine accurate quasiparticle and optical band gaps for InP, CdSe, and GaAs QDs from standard LDA calculations. Based on defect/impurity AEPs and the empirical correction, the electronic structure of Mn impurities in ZnS for both ZB and WZ crystal structures is calculated. We have first shown that the defect/impurity AEPs are in a good agreement with DFT calculations. We have highlighted that the atomic relaxation around the Mn impurity increases the band gap, and can be approximated by relaxation of the Mn-4S fragment to reduce the computational costs.

As an outlook, our fine-structure calculations form the foundation for further investigations into excitonic lifetimes and radiative recombination processes in alloyed dots, with potential research extensions into biexciton and trion dynamics. Additionally, our gap-corrected defect AEP enables future many-body multiplet calculations using windowed screening CI.

Appendix

$Cd_{45}Se_{45}\backslash$CdS-PH core-shell spectra

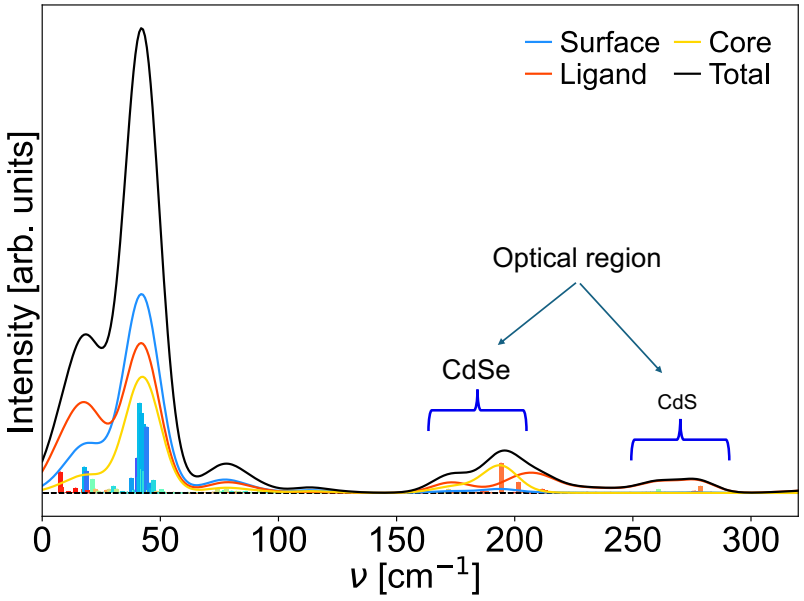

A.1: Calculated Raman spectra of $Cd_{45}Se_{45}\backslash$CdS-PH core-shell showing the optical regions for both CdSe core and CdS shell.

Supercell size convergence for Mn in ZB ZnS

Fig. A. 2 investigates the convergence of SP energies for Mn in ZB ZnS supercell w.r.t. supercell size. We consider supercells with dimensions of 2x2x2, 4x4x4, 6x6x6, and 8x8x8, representing repetitions of the bulk unit cell along all three axes. The Mn atom is positioned near the center of each supercell. For clarity, the figure presents the spin-up energy states for all supercell sizes plotted together. Likewise, the spin-down states are plotted together. States close to band gap are plotted only. Individual energy

levels corresponding to each supercell size are distinguished using the same marker style. Convergence is assessed by analyzing the change in energy levels as the supercell dimensions are expanded. We analyze the states in order of decreasing energy. We begin by analyzing the spin-up energy states for Mn in ZB ZnS supercells of varying sizes. The CBM energy for the 2x2x2 supercell (0.810 eV) exhibits a slight upward shift of 32 meV when the size is increased to 4x4x4. Further increase to 6x6x6 results in a significant decrease of 139 meV, with a further 1 meV decrease observed for the 8x8x8 supercell. This trend suggests a convergence of the CBM energy between 6x6x6 and 8x8x8 supercells. The next state in decreasing order is triply degenerate states (Magenta, Orange, Green) and show a change of 47 meV from 2x2x2 to 4x4x4, followed by a further change of 51 and 55 meV for 6x6x6 and 8x8x8 supercells, respectively. This indicates convergence between 6x6x6 and 8x8x8. Next, we have triply degenerate VBM states which show a larger change of 147 meV from 2x2x2 to 4x4x4. However, they converge between 6x6x6 and 8x8x8 with a change of only 50 meV for both sizes. he further lower doubly degenerate states (Blue, Pink) show a significant energy shift from 2x2x2 to 6x6x6, followed by a smaller change of 20 meV upon further increase to 8x8x8. Similar convergence trends are observed for spin-down states. The CBM energy has a larger shift of 127 meV from 2x2x2 to 6x6x6 and converges at 8x8x8 with a negligible

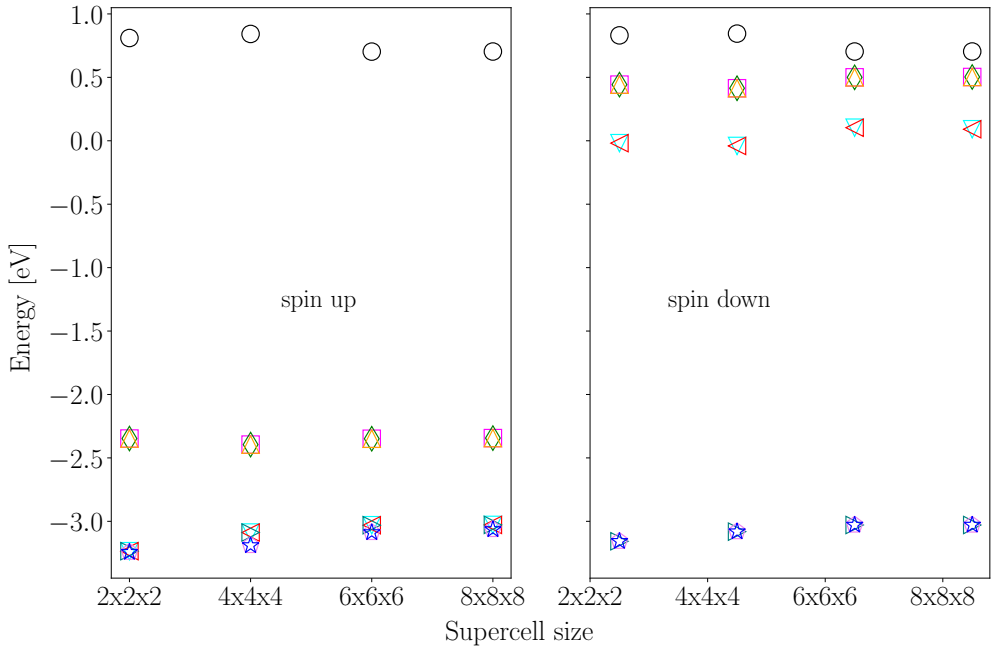

A.2: SP energy levels convergence w.r.t. supercell of bulk ZnS with single Mn impurity. Results are presented after the gap-correction of the ZnS host.

change of less than 1 meV. Likewise, the triply degenerate and doubly degenerate states show larger initial changes from 2x2x2 to 6x6x6 and minimal changes (around 2 meV) for the 8x8x8 supercell. The triply degenerate VBM state also exhibits a significant change from 2x2x2 to 6x6x6 and converges for the 8x8x8 supercell with a change of less than 1 meV. Considering the minimal energy change observed for energy states when increasing the supercell size from 6x6x6 to 8x8x8, a 6x6x6 supercell appears sufficient for obtaining reasonable results.

Bibliography

[1] Louis Brus. Electronic wave functions in semiconductor clusters: experiment and theory. *J. Phys. Chem.*, 90(12):2555–2560, 1986.

[2] Horst Weller. Quantized semiconductor particles: A novel state of matter for materials science. *Adv. Mater.*, 5(2):88–95, 1993.

[3] Benjamin T. Diroll. Colloidal quantum wells for optoelectronic devices. *J. Mater. Chem. C*, 8:10628–10640, 2020.

[4] P. Harrison. *Application to Quantum Wires and Dots*, chapter 13, pages 443–457. John Wiley & Sons, Ltd, 2005.

[5] Alexander N. Beecher, Rachel A. Dziatko, Michael L. Steigerwald, Jonathan S. Owen, and Andrew C. Crowther. Transition from molecular vibrations to phonons in atomically precise cadmium selenide quantum dots. *J. Am. Chem. Soc.*, 138(51):16754–16763, 2016.

[6] Graham H. Carey, Ahmed L. Abdelhady, Zhijun Ning, Susanna M. Thon, Osman M. Bakr, and Edward H. Sargent. Colloidal quantum dot solar cells. *Chem. Rev.*, 115(23):12732–12763, 2015. PMID: 26106908.

[7] Guido Burkard, Hans-Andreas Engel, and Daniel Loss. Spintronics and quantum dots for quantum computing and quantum communication. *Fortschritte der Physik*, 48(9-11):965–986, 2000.

[8] F. Pelayo García de Arquer, Dmitri V. Talapin, Victor I. Klimov, Yasuhiko Arakawa, Manfred Bayer, and Edward H. Sargent. Semiconductor quantum dots: Technological progress and future challenges. *Science*, 373(6555):eaaz8541, 2021.

[9] M.S. Dresselhaus, Y.-M. Lin, S.B. Cronin, O. Rabin, M.R. Black, G. Dresselhaus, and T. Koga. Chapter 1 - quantum wells and quantum wires for potential

thermoelectric applications. In Terry M. Tritt, editor, *Recent Trends in Thermoelectric Materials Research III*, volume 71 of *Semiconductors and Semimetals*, pages 1–121. Elsevier, 2001.

[10] Y. Arakawa. Quantum wires and quantum dots for fully confined semiconductor lasers. In *Nanostructures and Quantum Effects*, pages 199–207, Berlin, Heidelberg, 1994. Springer Berlin Heidelberg.

[11] Fudong Wang, Angang Dong, and William E. Buhro. Solution–liquid–solid synthesis, properties, and applications of one-dimensional colloidal semiconductor nanorods and nanowires. *Chem. Rev.*, 116(18):10888–10933, 2016. PMID: 26974736.

[12] Yi-Hsin Liu, Fudong Wang, Jessica Hoy, Virginia L. Wayman, Lindsey K. Steinberg, Richard A. Loomis, and William E. Buhro. Bright core–shell semiconductor quantum wires. *J. Am. Chem. Soc.*, 134(45):18797–18803, 2012. PMID: 23095017.

[13] Jae Sung Son, Jung Ho Yu, Soon Gu Kwon, Jihwa Lee, Jin Joo, and Taeghwan Hyeon. Colloidal synthesis of ultrathin two-dimensional semiconductor nanocrystals. *Adv. Mater.*, 23(28):3214–3219, 2011.

[14] S. Ithurria, M. D. Tessier, B. Mahler, R. P. S. M. Lobo, B. Dubertret, and Al. L. Efros. Colloidal nanoplatelets with two-dimensional electronic structure. *Nat. Mater.*, 10(12):936–941, 2011.

[15] Cécile Bouet, Mickael D. Tessier, Sandrine Ithurria, Benoit Mahler, Brice Nadal, and Benoit Dubertret. Flat colloidal semiconductor nanoplatelets. *Chem. Mater.*, 25(8):1262–1271, 04 2013.

[16] Hilmi Volkan Demir, Sedat Nizamoglu, Talha Erdem, Evren Mutlugun, Nikolai Gaponik, and Alexander Eychmüller. Quantum dot integrated leds using photonic and excitonic color conversion. *Nano Today*, 6(6):632–647, 2011.

[17] Vasudevanpillai Biju, Tamitake Itoh, Abdulaziz Anas, Athiyanathil Sujith, and Mitsuru Ishikawa. Semiconductor quantum dots and metal nanoparticles: syntheses, optical properties, and biological applications. *Analytical and Bioanalytical Chemistry*, 391(7):2469–2495, 2008.

[18] Igor L. Medintz and Hedi Mattoussi. Quantum dot-based resonance energy transfer and its growing application in biology. *Phys. Chem. Chem. Phys.*, 11:17–45, 2009.

[19] Katherine Bourzac. Quantum dots go on display. *Nature*, 493(7432):283–283, 2013.

[20] Torben Steenbock, Tobias Dittmann, Surender Kumar, and Gabriel Bester. Ligand-induced symmetry breaking as the origin of multiexponential photoluminescence decay in CdSe quantum dots. *J. Phys. Chem. Lett.*, 14(39):8859–8866, 10 2023.

[21] Dibyajyoti Ghosh, Sergei A. Ivanov, and Sergei Tretiak. Structural dynamics and electronic properties of semiconductor quantum dots: Computational insights. *Chem. Mater*, 33(19):7848–7857, 2021.

[22] A. P. Litvin, I. V. Martynenko, F. Purcell-Milton, A. V. Baranov, A. V. Fedorov, and Y. K. Gun'ko. Colloidal quantum dots for optoelectronics. *J. Mater. Chem. A*, 5:13252–13275, 2017.

[23] Yashaswi Nandan and Mohan Singh Mehata. Wavefunction engineering of Type-I/Type-II excitons of CdSe/CdS core-shell quantum dots. *Sci. Rep.*, 9(1):2, 2019.

[24] Youngjin Jang, Arthur Shapiro, Maya Isarov, Anna Rubin-Brusilovski, Aron Safran, Adam K. Budniak, Faris Horani, Joanna Dehnel, Aldona Sashchiuk, and Efrat Lifshitz. Interface control of electronic and optical properties in IV–VI and II-VI core/shell colloidal quantum dots: a review. *Chem. Commun.*, 53:1002–1024, 2017.

[25] Boni Samuel, S Mathew, V R Anand, Adrine Antony Correya, V P N Nampoori, and A Mujeeb. Surface defect assisted broad spectra emission from CdSe quantum dots for white led application. *Mater. Res. Express*, 5(2):025009, feb 2018.

[26] Jin Young Kim, Oleksandr Voznyy, David Zhitomirsky, and Edward H. Sargent. 25th anniversary article: Colloidal quantum dot materials and devices: A quarter-century of advances. *Adv. Mater.*, 25(36):4986–5010, 2013.

[27] Jyotirmayee Sahu, Deeptimayee Prusty, Sriram Mansingh, and Kulamani Parida. A review on alloyed quantum dots and their applications as photocatalysts. *Int. J. Hydrogen Energy*, 48(75):29097–29118, 2023.

[28] Dipanwita Roy, Piyush Kanti Sarkar, Amit Dalui, Uttam Kumar Ghorai, Dharmendra K. Gupta, and Somobrata Acharya. Large stokes shifted quaternary copper cadmium sulfide selenide quantum dot waveguides. *J. Mater. Chem. C*, 9:8066–8075, 2021.

[29] Yuxin Liu, Yudong Guo, Baoheng Lin, Zhenjun Chen, Xiangjing Ying, Menglong Zhang, Chuanglei Wang, Gaotian Zhang, Huaimin Gu, Dongxiang Luo, and Xiao Liu. Gradient alloyed quantum dots for photocatalytic lignin valorization via proton coupled electron transfer. *ACS App. Nano Mater.*, 6(8):6614–6626, 2023.

[30] Joerg Wrachtrup. Defect center room-temperature quantum processors. *PNAS*, 107(21):9479–9480, 2010.

[31] Michael J. Bowers, James R. McBride, and Sandra J. Rosenthal. White-light emission from magic-sized cadmium selenide nanocrystals. *J. Am. Chem. Soc.*, 127(44):15378–15379, 2005.

[32] Svetlana Kilina, Sergei Ivanov, and Sergei Tretiak. Effect of surface ligands on optical and electronic spectra of semiconductor nanoclusters. *J. Am. Chem. Soc.*, 131(22):7717–7726, 06 2009.

[33] Svetlana Kilina, Kirill A. Velizhanin, Sergei Ivanov, Oleg V. Prezhdo, and Sergei Tretiak. Surface ligands increase photoexcitation relaxation rates in CdSe quantum dots. *ACS Nano*, 6(7):6515–6524, 07 2012.

[34] Erik Busby, Nicholas C. Anderson, Jonathan S. Owen, and Matthew Y. Sfeir. Effect of surface stoichiometry on blinking and hole trapping dynamics in CdSe nanocrystals. *J. Phys. Chem. C*, 119(49):27797–27803, 2015.

[35] Tamar Goldzak, Alexandra R. McIsaac, and Troy Van Voorhis. Colloidal CdSe nanocrystals are inherently defective. *Nat. Comm.*, 12(1):890, 2021.

[36] C. de Mello Donegá, M. Bode, and A. Meijerink. Size- and temperature-dependence of exciton lifetimes in CdSe quantum dots. *Phys. Rev. B*, 74:085320, Aug 2006.

[37] V. N. Soloviev, A. Eichhöfer, D. Fenske, and U. Banin. Molecular limit of a bulk semiconductor: Size dependence of the "band gap" in CdSe cluster molecules. *J. Am. Chem. Soc.*, 122(11):2673–2674, 2000.

[38] D. J. Norris, Al. L. Efros, M. Rosen, and M. G. Bawendi. Size dependence of exciton fine structure in CdSe quantum dots. *Phys. Rev. B*, 53:16347–16354, Jun 1996.

[39] Mark J. Fernée, Brad N. Littleton, Steven Cooper, Halina Rubinsztein-Dunlop, Daniel E. Gómez, and Paul Mulvaney. Acoustic phonon contributions to the emission spectrum of single CdSe nanocrystals. *J. Phys. Chem. C*, 112(6):1878–1884, 2008.

[40] Mark J. Fernée, Chiara Sinito, Paul Mulvaney, Philippe Tamarat, and Brahim Lounis. The optical phonon spectrum of CdSe colloidal quantum dots. *Phys. Chem. Chem. Phys.*, 16:16957–16961, 2014.

[41] Peng Han and Gabriel Bester. Determination of the phonon sidebands in the photoluminescence spectrum of semiconductor nanoclusters from ab initio calculations. *Phys. Rev. B*, 106:245404, Dec 2022.

[42] Gerwin Chilla, Tobias Kipp, Torben Menke, Detlef Heitmann, Marija Nikolic, Andreas Frömsdorf, Andreas Kornowski, Stephan Förster, and Horst Weller. Direct observation of confined acoustic phonons in the photoluminescence spectra of a single CdSe-CdS-ZnS core-shell-shell nanocrystal. *Phys. Rev. Lett.*, 100:057403, Feb 2008.

[43] Yujuan Xie, Ning Du, Shengping Yu, Li Zhang, and Mingli Yang. Unraveling the structure-dependent radiative and nonradiative decays in (CdSe)13 clusters through first-principles calculations. *J. Phys. Chem. C*, 123(50):30714–30722, 2019.

[44] Volodymyr M. Dzhagan, Mykhailo Ya. Valakh, Alexander G. Milekhin, Nikolay A. Yeryukov, Dietrich R.T. Zahn, Elsa Cassette, Thomas Pons, and Benoit Dubertret. Raman- and IR-active phonons in CdSe/CdS core/shell nanocrystals in the presence of interface alloying and strain. *J. Phys. Chem. C*, 117(35):18225–18233, 2013.

[45] V M Dzhagan, Yu M Azhniuk, A G Milekhin, and D R T Zahn. Vibrational spectroscopy of compound semiconductor nanocrystals. *J. Phys. D: Appl. Phys.*, 51(50):503001, sep 2018.

[46] Narine Moses Badlyan, Amelie Biermann, Tangi Aubert, Zeger Hens, and Janina Maultzsch. Thermal expansion of colloidal CdSe/CdS core/shell quantum dots. *Phys. Rev. B*, 99:195425, May 2019.

[47] Chen Lin, David F. Kelley, Mikaela Rico, and Anne Myers Kelley. The "surface optical" phonon in CdSe nanocrystals. *ACS Nano*, 8(4):3928–3938, 2014.

[48] Prabuddha Mukherjee, Sung Jun Lim, Tomasz P. Wrobel, Rohit Bhargava, and Andrew M. Smith. Measuring and predicting the internal structure of semiconductor nanocrystals through Raman spectroscopy. *J. Am. Chem. Soc.*, 138(34):10887–10896, 2016.

[49] Patryk Kusch, Holger Lange, Mikhail Artemyev, and Christian Thomsen. Size-dependence of the anharmonicities in the vibrational potential of colloidal CdSe nanocrystals. *Solid State Commun.*, 151(1):67–70, 2011.

[50] Liu Lu, Xiao-Liang Xu, Wen-Tao Liang, and Hai-Fei Lu. Raman analysis of CdSe/CdS core–shell quantum dots with different CdS shell thickness. *J. Condens. Matter Phys.*, 19(40):406221, sep 2007.

[51] Anielle Christine A. Silva, Ernesto S. Freitas Neto, Sebastião W. da Silva, Paulo C. Morais, and Noelio O. Dantas. Modified phonon confinement model and its application to CdSe/CdS core–shell magic-sized quantum dots synthesized in aqueous solution by a new route. *J. Phys. Chem. C*, 117(4):1904–1914, 2013.

[52] Igor Dmitruk, Rodion V. Belosludov, Andriy Dmytruk, Yasuto Noda, Yuri Barnakov, Yeon-Su Park, and Atsuo Kasuya. Experimental and computational studies of the structure of CdSe magic-size clusters. *J. Phys. Chem. A*, 124(17):3398–3406, 2020.

[53] Norman Tschirner, Holger Lange, Andrei Schliwa, Amelie Biermann, Christian Thomsen, Karel Lambert, Raquel Gomes, and Zeger Hens. Interfacial alloying in CdSe/CdS heteronanocrystals: A Raman spectroscopy analysis. *Chem. Mater.*, 24(2):311–318, 2012.

[54] Robert W. Meulenberg, Travis Jennings, and Geoffrey F. Strouse. Compressive and tensile stress in colloidal CdSe semiconductor quantum dots. *Phys. Rev. B*, 70:235311, Dec 2004.

[55] Volodymyr Dzhagan, Mykhailo Valakh, Nikolai Melnik, Olexandra Rayevska, Irina Lokteva, Joanna Kolny-Olesiak, and Dietrich R. T. Zahn. Phonon spectra of small colloidal II-VI semiconductor nanocrystals. *Int. J. Spectrosc.*, 2012(1):532385, 2012.

[56] Mersedeh Saniepay, Chenjia Mi, Zhihui Liu, E. Paige Abel, and Rémi Beaulac. Insights into the structural complexity of colloidal CdSe nanocrystal surfaces: Correlating the efficiency of nonradiative excited-state processes to specific defects. *J. Am. Chem. Soc.*, 140(5):1725–1736, 2018.

[57] Arjan J. Houtepen, Zeger Hens, Jonathan S. Owen, and Ivan Infante. On the origin of surface traps in colloidal II-VI semiconductor nanocrystals. *Chem. Mater.*, 29(2):752–761, 2017.

[58] Torben Steenbock, Emilia Drescher, Tobias Dittmann, and Gabriel Bester. How surface defects shape the excitons and photoluminescence of ultrasmall CdSe quantum dots. *Chem. Mater.*, 36(13):6504–6514, 2024.

[59] Manav Bhati, Sergei A. Ivanov, Thomas P. Senftle, Sergei Tretiak, and Dibyajyoti Ghosh. How structural and vibrational features affect optoelectronic properties of non-stoichiometric quantum dots: computational insights. *Nanoscale*, 15:7176–7185, 2023.

[60] Ahmed M. Abuelela, Tarek A. Mohamed, and Oleg V. Prezhdo. Dft simulation and vibrational analysis of the IR and Raman spectra of a CdSe quantum dot capped by methylamine and trimethylphosphine oxide ligands. *J. Phys. Chem. C*, 116(27):14674–14681, 2012.

[61] Gabriel Bester. Electronic excitations in nanostructures: an empirical pseudopotential based approach. *J. Phys.: Condens. Matter*, 21(2):023202, 2009.

[62] Gabriel Bester, Selvakumar Nair, and Alex Zunger. Pseudopotential calculation of the excitonic fine structure of million-atom self-assembled $In_{1-x}Ga_xAs$/GaAs quantum dots. *Phys. Rev. B*, 67:161306, Apr 2003.

[63] A. Franceschetti, H. Fu, L. W. Wang, and A. Zunger. Many-body pseudopotential theory of excitons in InP and CdSe quantum dots. *Phys. Rev. B*, 60:1819–1829, Jul 1999.

[64] Xiao Jin, Kanlin Xie, Tingting Zhang, Huada Lian, Zhenghe Zhang, Bing Xu, Dongyu Li, and Qinghua Li. Cation exchange assisted synthesis of ZnCdSe/ZnSe quantum dots with narrow emission line widths and near-unity photoluminescence quantum yields. *Chem. Commun.*, 56:6130–6133, 2020.

[65] Ou Chen, Jing Zhao, Vikash P. Chauhan, Jian Cui, Cliff Wong, Daniel K. Harris, He Wei, Hee-Sun Han, Dai Fukumura, Rakesh K. Jain, and Moungi G. Bawendi. Compact high-quality CdSe-CdS core–shell nanocrystals with narrow emission linewidths and suppressed blinking. *Nat. Mater.*, 12(5):445–451, 2013.

[66] Jinke Bai, Linfeng Wang, Tingting Zhang, Tianyi Hou, Meilun Zhang, Bing Xu, Dongyu Li, Xiao Jin, Qinghua Li, Yuxiao Wang, Xueru Zhang, and Yinglin Song. Enabling ultranarrow blue emission linewidths in colloidal alloy quantum dots by decreasing the exciton fine structure splitting and exciton-phonon coupling. *Nano Res.*, 16(1):1576–1585, 2023.

[67] J. R. Cárdenas and G. Bester. Atomic effective pseudopotentials for semiconductors. *Phys. Rev. B*, 86:115332, Sep 2012.

[68] Hanh Bui, Anastasia Karpulevich, and Gabriel Bester. Excitonic fine structure of zinc-blende and wurtzite colloidal CdSe nanocrystals and comparison to effective mass results. *Phys. Rev. B*, 101:115414, Mar 2020.

[69] Stephan Lany and Alex Zunger. Assessment of correction methods for the band-gap problem and for finite-size effects in supercell defect calculations: Case studies for ZnO and GaAs. *Phys. Rev. B*, 78:235104, Dec 2008.

[70] Stephan Lany and Alex Zunger. Accurate prediction of defect properties in density functional supercell calculations. *Modelling Simul. Mater. Sci. Eng.*, 17(8):084002, nov 2009.

[71] W. Pfäffle, D. Antonov, J. Wrachtrup, and G. Bester. Screened configuration interaction method for open-shell excited states applied to nv centers. *Phys. Rev. B*, 104:104105, Sep 2021.

[72] Max Born and J Robert Oppenheimer. On the quantum theory of molecules. *Annalen der Physik (in German)*, 389, 1927.

[73] I. Morgenstern. Quantum-monte-carlo simulations for fermionic systems. *Zeitschrift für Physik B Cond. Matter*, 77(2):267–273, 1989.

[74] Pierre Hohenberg and Walter Kohn. Inhomogeneous electron gas. *Phys. Rev.*, 136(3B):B864, 1964.

[75] W. Kohn and L. J. Sham. Self-consistent equations including exchange and correlation effects. *Phys. Rev.*, 140:A1133–A1138, Nov 1965.

[76] J. C. Slater. A simplification of the hartree-fock method. *Phys. Rev.*, 81:385–390, Feb 1951.

[77] J. P. Perdew and Alex Zunger. Self-interaction correction to density-functional approximations for many-electron systems. *Phys. Rev. B*, 23:5048–5079, May 1981.

[78] John P. Perdew and Yue Wang. Accurate and simple analytic representation of the electron-gas correlation energy. *Phys. Rev. B*, 45:13244–13249, Jun 1992.

[79] Axel D. Becke and Erin R. Johnson. A simple effective potential for exchange. *J. Chem. Phys.*, 124(22):221101, 06 2006.

[80] A. D. Becke. Density-functional exchange-energy approximation with correct asymptotic behavior. *Phys. Rev. A*, 38:3098–3100, Sep 1988.

[81] D. R. Hamann, M. Schlüter, and C. Chiang. Norm-conserving pseudopotentials. *Phys. Rev. Lett.*, 43:1494–1497, Nov 1979.

[82] H Haken. Z. physik 146, 527 (1956). *Nuovo cim*, 10:1230, 1956.

[83] Raffaele Resta. Thomas-fermi dielectric screening in semiconductors. *Phys. Rev. B*, 16:2717–2722, Sep 1977.

[84] David R Penn. Wave-number-dependent dielectric function of semiconductors. *Phys. Rev.*, 128(5):2093, 1962.

[85] P. Y. Yu and M. Cardona. *Fundamentals of semiconductors: physics and materials properties.* Springer, 4th edition, 2010.

[86] Surender Kumar, Torben Steenbock, and Gabriel Bester. Origin of the high-frequency shoulder in the raman spectra of cdse quantum dots. *The Journal of Physical Chemistry Letters*, 15(41):10392–10398, 10 2024.

[87] Peng Han and Gabriel Bester. Heavy strain conditions in colloidal core-shell quantum dots and their consequences on the vibrational properties from *ab initio* calculations. *Phys. Rev. B*, 92:125438, Sep 2015.

[88] A. V. Baranov, Yu. P. Rakovich, J. F. Donegan, T. S. Perova, R. A. Moore, D. V. Talapin, A. L. Rogach, Y. Masumoto, and I. Nabiev. Effect of ZnS shell thickness on the phonon spectra in CdSe quantum dots. *Phys. Rev. B*, 68:165306, Oct 2003.

[89] V M Dzhagan, M Ya Valakh, A E Raevskaya, A L Stroyuk, S Ya Kuchmiy, and D R T Zahn. Size effects on Raman spectra of small CdSe nanoparticles in polymer films. *Nanotechnology*, 19(30):305707, jun 2008.

[90] Young-Nam Hwang, Seung-Han Park, and Dongho Kim. Size-dependent surface phonon mode of CdSe quantum dots. *Phys. Rev. B*, 59:7285–7288, Mar 1999.

[91] Peng Han and Gabriel Bester. Confinement effects on the vibrational properties of III-V and II-VI nanoclusters. *Phys. Rev. B*, 85:041306, Jan 2012.

[92] Yukun Gao and Penggang Yin. Effect of bond dispersion on Raman spectra shift in II-VI semiconductor nanocrystals. *Inorg. Chem.*, 58(8):4859–4868, 2019.

[93] C. V. Raman and K. S. KRISHNAN. A new type of secondary radiation. *Nature*, 121(3048):501–502, 1928.

[94] Raghvender Raghvender. *Ab-initio study of the structure of tellurium-oxide based glasses : a step forward in establishing the structure-properties relationships*. PhD thesis, 2023. Thèse de doctorat dirigée par Masson, Olivier et Bouzid, Assil Matériaux céramiques et traitements de surface Limoges 2023.

[95] Xavier Gonze and Changyol Lee. Dynamical matrices, born effective charges, dielectric permittivity tensors, and interatomic force constants from density-functional perturbation theory. *Phys. Rev. B*, 55:10355–10368, Apr 1997.

[96] Pablo García-Risueño, Peng Han, Surender Kumar, and Gabriel Bester. Frozen-phonon method for state anticrossing situations and its application to zero-point motion effects in diamondoids. *Phys. Rev. B*, 108:125403, Sep 2023.

[97] Johannes Neugebauer, Markus Reiher, Carsten Kind, and Bernd A. Hess. Quantum chemical calculation of vibrational spectra of large molecules—Raman and IRspectra for buckminsterfullerene. *J. Com. Phys.*, 23(9):895–910, 2002.

[98] Dmitrij Rappoport and Filipp Furche. Lagrangian approach to molecular vibrational Raman intensities using time-dependent hybrid density functional theory. *J. Chem. Phys.*, 126(20):201104, 05 2007.

[99] Filipp Furche. On the density matrix based approach to time-dependent density functional response theory. *J. Chem. Phys.*, 114(14):5982–5992, 04 2001.

[100] Filipp Furche and Reinhart Ahlrichs. Adiabatic time-dependent density functional methods for excited state properties. *J. Chem. Phys.*, 117(16):7433–7447, 10 2002.

[101] Reinhart Ahlrichs, Michael Bär, Marco Häser, Hans Horn, and Christoph Kölmel. Electronic structure calculations on workstation computers: The program system turbomole. *Chem. Phys. Lett.*, 162(3):165–169, 1989.

[102] John P. Perdew, Kieron Burke, and Matthias Ernzerhof. Generalized gradient approximation made simple. *Phys. Rev. Lett.*, 77:3865–3868, Oct 1996.

[103] Florian Weigend. Accurate coulomb-fitting basis sets for H to Rn. *Phys. Chem. Chem. Phys.*, 8:1057–1065, 2006.

[104] Stefan Grimme, Jens Antony, Stephan Ehrlich, and Helge Krieg. A consistent and accurate *ab initio* parametrization of density functional dispersion correction (DFT-D) for the 94 elements H-Pu. *J. Chem. Phys.*, 132(15):154104, 04 2010.

[105] Karin Eichkorn, Oliver Treutler, Holger Öhm, Marco Häser, and Reinhart Ahlrichs. Auxiliary basis sets to approximate coulomb potentials. *Chem. Phys. Lett.*, 240(4):283–290, 1995.

[106] Karin Eichkorn, Florian Weigend, Oliver Treutler, and Reinhart Ahlrichs. Auxiliary basis sets for main row atoms and transition metals and their use to approximate coulomb potentials. *Theor. Chem. Acc.*, 97(1):119–124, 1997.

[107] Marek Sierka, Annika Hogekamp, and Reinhart Ahlrichs. Fast evaluation of the Coulomb potential for electron densities using multipole accelerated resolution of identity approximation. *J. Chem. Phys.*, 118(20):9136–9148, 05 2003.

[108] Peter Deglmann, Filipp Furche, and Reinhart Ahlrichs. An efficient implementation of second analytical derivatives for density functional methods. *Chem. Phys. Lett.*, 362(5):511–518, 2002.

[109] Atsuo Kasuya, Rajaratnam Sivamohan, Yurii A. Barnakov, Igor M. Dmitruk, Takashi Nirasawa, Volodymyr R. Romanyuk, Vijay Kumar, Sergiy V. Mamykin, Kazuyuki Tohji, Balachandran Jeyadevan, Kozo Shinoda, Toshiji Kudo, Osamu Terasaki, Zheng Liu, Rodion V. Belosludov, Vijayaraghavan Sundararajan, and Yoshiyuki Kawazoe. Ultra-stable nanoparticles of CdSe revealed from mass spectrometry. *Nat. Mater.*, 3(2):99–102, 2004.

[110] Yeon-Su Park, Andriy Dmytruk, Igor Dmitruk, Atsuo Kasuya, Yukihiro Okamoto, Noritada Kaji, Manabu Tokeshi, and Yoshinobu Baba. Aqueous phase synthesized CdSe nanoparticles with well-defined numbers of constituent atoms. *J. Phys. Chem. C*, 114(44):18834–18840, 11 2010.

[111] Nicholas C. Anderson, Mark P. Hendricks, Joshua J. Choi, and Jonathan S. Owen. Ligand exchange and the stoichiometry of metal chalcogenide nanocrystals: Spectroscopic observation of facile metal-carboxylate displacement and binding. *J. Am. Chem. Soc.*, 135(49):18536–18548, 2013. PMID: 24199846.

[112] Surender Kumar, Hanh Bui, and Gabriel Bester. Empirical band-gap correction for lda-derived atomic effective pseudopotentials. *Comp. Cond. Matter*, 40:e00917, 2024.

[113] J. E. Bowen Katari, V. L. Colvin, and A. P. Alivisatos. X-ray photoelectron spectroscopy of cdse nanocrystals with applications to studies of the nanocrystal surface. *J. Phys. Chem.*, 98(15):4109–4117, 1994.

[114] Adam J. Morris-Cohen, Michał Malicki, Mark D. Peterson, John W. J. Slavin, and Emily A. Weiss. Chemical, structural, and quantitative analysis of the ligand shells of colloidal quantum dots. *Chem. Mater.*, 25(8):1155–1165, 2013.

[115] Salvatore Cosseddu, Roberta Pascazio, Carlo Giansante, Liberato Manna, and Ivan Infante. Ligand dynamics on the surface of cdse nanocrystals. *Nanoscale*, 15:7410–7419, 2023.

[116] M Calixto and E Romera. Inverse participation ratio and localization in topological insulator phase transitions. *J. Stat. Mech. : Theo. & Exp.*, 2015(6):P06029, jun 2015.

[117] Surender Kumar, Torben Steenbock, and Bester Gabriel. Origin of the High-Frequency Shoulder in the Raman Spectra of CdSe Quantum Dots. *ChemRxiv*, 2024.

[118] Michelle D. Regulacio and Ming-Yong Han. Composition-tunable alloyed semiconductor nanocrystals. *Acc. Chem. Res.*, 43(5):621–630, 2010. PMID: 20214405.

[119] Jannik Rebmann, Hans Werners, Florian Johst, Marcel Dohrmann, Yannic U. Staechelin, Christian Strelow, Alf Mews, and Tobias Kipp. Cation exchange during the synthesis of colloidal Type-II ZnSe-dot/CdS-rod nanocrystals. *Chem. Mater.*, 35(3):1238–1248, 2023.

[120] Bing Xu, Haibin Chen, Tingting Zhang, Qing Long, Lishu Huang, Dongyu Li, Zhenghe Zhang, Zhen Huang, Qinghua Li, and Xiao Jin. High quality quarternary-alloyed ZnCdSSe/ZnS quantum dots with single photoluminescence decay channel and high devise stability. *J. Lumin.*, 240:118463, 2021.

[121] B.P Zhang, Y.Q Li, T Yasuda, Y Segawa, K Edamatsu, and T Itoh. Time-resolved photoluminescence of ZnCdSe single quantum dots. *J. Crys. Growth*, 214-215:765–769, 2000.

[122] Negar Gheshlaghi, Hadi Sedaghat Pisheh, and Hilmi Ünlü. Composition and strain effects in Type I and Type II heterostructure ZnSe/Cd(Zn)S and ZnSe/$Cd_{1-x}Zn_xS$ core/shell quantum dots. *Superlattices and Microstructures*, 111:156–165, 2017.

[123] Alessandro Minotto, Francesco Todescato, Ilaria Fortunati, Raffaella Signorini, Jacek J. Jasieniak, and Renato Bozio. Role of core–shell interfaces on exciton recombination in CdSe–$Cd_xZn_{1-x}S$ quantum dots. *J. Phys. Chem. C*, 118(41):24117–24126, 2014.

[124] Wan Ki Bae, Lazaro A. Padilha, Young-Shin Park, Hunter McDaniel, Istvan Robel, Jeffrey M. Pietryga, and Victor I. Klimov. Controlled alloying of the core–shell interface in CdSe/CdSe quantum dots for suppression of auger recombination. *ACS Nano*, 7(4):3411–3419, 2013. PMID: 23521208.

[125] S. A. Crooker, T. Barrick, J. A. Hollingsworth, and V. I. Klimov. Multiple temperature regimes of radiative decay in CdSe nanocrystal quantum dots: Intrinsic limits to the dark-exciton lifetime. *App. Phys. Lett.*, 82(17):2793–2795, 04 2003.

[126] Olivier Labeau, Philippe Tamarat, and Brahim Lounis. Temperature dependence of the luminescence lifetime of single CdSe/ZnS quantum dots. *Phys. Rev. Lett.*, 90(25):257404, 2003.

[127] L. Biadala, Y. Louyer, Ph. Tamarat, and B. Lounis. Direct observation of the two lowest exciton zero-phonon lines in single CdSe/ZnS nanocrystals. *Phys. Rev. Lett.*, 103:037404, Jul 2009.

[128] Elena V. Shornikova, Louis Biadala, Dmitri R. Yakovlev, Victor F. Sapega, Yuri G. Kusrayev, Anatolie A. Mitioglu, Mariana V. Ballottin, Peter C. M. Christianen, Vasilii V. Belykh, Mikhail V. Kochiev, Nikolai N. Sibeldin, Aleksandr A. Golovatenko, Anna V. Rodina, Nikolay A. Gippius, Alexis Kuntzmann, Ye Jiang, Michel Nasilowski, Benoit Dubertret, and Manfred Bayer. Addressing the exciton fine structure in colloidal nanocrystals: the case of CdSe nanoplatelets. *Nanoscale*, 10:646–656, 2018.

[129] A. Muller, P. Bianucci, C. Piermarocchi, M. Fornari, I. C. Robin, R. André, and C. K. Shih. Time-resolved photoluminescence spectroscopy of individual Te impurity centers in ZnSe. *Phys. Rev. B*, 73:081306, Feb 2006.

[130] Louis Biadala, Yann Louyer, Ph Tamarat, and Brahim Lounis. Direct observation of the two lowest exciton zero-phonon lines in single CdSe/ZnS nanocrystals. *Phys. Rev. Lett.*, 103(3):037404, 2009.

[131] Marcel Bruchez, Mario Moronne, Peter Gin, Shimon Weiss, and A Paul Alivisatos. Semiconductor nanocrystals as fluorescent biological labels. *science*, 281(5385):2013–2016, 1998.

[132] Qingjiang Sun, Y Andrew Wang, Lin Song Li, Daoyuan Wang, Ting Zhu, Jian Xu, Chunhe Yang, and Yongfang Li. Bright, multicoloured light-emitting diodes based on quantum dots. *Nat. Photonics*, 1(12):717, 2007.

[133] Katherine Bourzac. Quantum dots go on display. *Nature News*, 493(7432):283, 2013.

[134] Joel Q Grim, Sotirios Christodoulou, Francesco Di Stasio, Roman Krahne, Roberto Cingolani, Liberato Manna, and Iwan Moreels. Continuous-wave biexciton lasing at room temperature using solution-processed quantum wells. *Nature nanotechnology*, 9(11):891, 2014.

[135] Jie Bao and Moungi G Bawendi. A colloidal quantum dot spectrometer. *Nature*, 523(7558):67, 2015.

[136] Monica Lorenzon, Sotirios Christodoulou, Gianfranco Vaccaro, Jacopo Pedrini, Francesco Meinardi, Iwan Moreels, and Sergio Brovelli. Reversed oxygen sensing using colloidal quantum wells towards highly emissive photoresponsive varnishes. *Nat. Comm.*, 6:6434, 2015.

[137] C Delerue, G Allan, and YM Niquet. Collective excitations in charged nanocrystals and in close-packed arrays of charged nanocrystals. *Phys. Rev. B*, 72(19):195316, 2005.

[138] Marek Korkusinski, Oleksandr Voznyy, and Pawel Hawrylak. Fine structure and size dependence of exciton and biexciton optical spectra in CdSe nanocrystals. *Phys. Rev. B*, 82(24):245304, 2010.

[139] Sebastian Steiger, Michael Povolotskyi, Hong-Hyun Park, Tillmann Kubis, and Gerhard Klimeck. NEMO5: A Parallel Multiscale Nanoelectronics Modeling Tool. *IEEE Transactions on Nanotechnology*, 10(6):1464–1474, October 2011.

[140] J G Díaz and G W Bryant. Electronic and optical fine structure of GaAs nanocrystals: The role of d-orbitals in a tight-binding approach. *Phys. Rev. B*, 73(7):929, February 2006.

[141] Otfried Madelung. *Semiconductors: data handbook*. Springer Science & Business Media, 2012.

[142] K. A. Mäder and A. Zunger. Empirical atomic pseudopotentials for AlAs/GaAs superlattices, alloys, and nanostructures. *Phys. Rev. B*, 50:17393, 1994.

[143] Lin-Wang Wang and Alex Zunger. Linear combination of bulk bands method for large-scale electronic structure calculations on strained nanostructures. *Phys. Rev. B*, 59:15806–15818, Jun 1999.

[144] P. N. Keating. Effect of invariance requirements on the elastic strain energy of crystals with application to the diamond structure. *Phys. Rev.*, 145:637–645, May 1966.

[145] A. J. Williamson, L. W. Wang, and Alex Zunger. Theoretical interpretation of the experimental electronic structure of lens-shaped self-assembled InAs/GaAs quantum dots. *Phys. Rev. B*, 62:12963–12977, Nov 2000.

[146] Jun-Wei Luo, Gabriel Bester, and Alex Zunger. *Atomistic Pseudopotential Theory of Droplet Epitaxial GaAs/AlGaAs Quantum Dots*, pages 329–361. Springer New York, New York, NY, 2013.

[147] Sadao Adachi. *Properties of Group-IV, III-V and II-VI Semiconductors*, chapter 3, pages 41–72. John Wiley & Sons, Ltd, 2005.

[148] Anastasia Karpulevich, Hanh Bui, Denis Antonov, Peng Han, and Gabriel Bester. Nonspherical atomic effective pseudopotentials for surface passivation. *Phys. Rev. B*, 94:205417, Nov 2016.

[149] Lin-Wang Wang and Alex Zunger. Pseudopotential calculations of nanoscale CdSe quantum dots. *Phys. Rev. B*, 53:9579–9582, Apr 1996.

[150] Su-Huai Wei and Alex Zunger. Giant and composition-dependent optical bowing coefficient in GaAsN alloys. *Phys. Rev. Lett.*, 76:664–667, Jan 1996.

[151] James E. Bernard and Alex Zunger. Electronic structure of ZnS, Znse, ZnTe, and their pseudobinary alloys. *Phys. Rev. B*, 36:3199–3228, Aug 1987.

[152] Rayapati Venugopal, Ping-I Lin, and Yit-Tsong Chen. Photoluminescence and Raman scattering from catalytically grown $Zn_xCd_{1-x}Se$ alloy nanowires. *J. Phys. Chem. B*, 110(24):11691–11696, 2006. PMID: 16800464.

[153] Daniel Mourad, Gerd Czycholl, Carsten Kruse, Sebastian Klembt, Reiner Retzlaff, Detlef Hommel, Mariuca Gartner, and Mihai Anastasescu. Band gap bowing of binary alloys: Experimental results compared to theoretical tight-binding supercell calculations for $Cd_xZn_{1-x}Se$. *Phys. Rev. B*, 82:165204, Oct 2010.

[154] K Matsuda, SV Nair, HE Ruda, Y Sugimoto, T Saiki, and K Yamaguchi. Two-exciton state in GaSb/ GaAs type II quantum dots studied using near-field photoluminescence spectroscopy. *App. Phys. Lett.*, 90(1), 2007.

[155] N. Troullier and José Luís Martins. Efficient pseudopotentials for plane-wave calculations. *Phys. Rev. B*, 43:1993–2006, Jan 1991.

[156] F Zirkelbach, P-Y Prodhomme, Peng Han, R Cherian, and G Bester. Large-scale atomic effective pseudopotential program including an efficient spin-orbit coupling treatment in real space. *Phys. Rev. B*, 91(7):075119, 2015.

[157] Leonard Kleinman and D. M. Bylander. Efficacious form for model pseudopotentials. *Phys. Rev. Lett.*, 48:1425–1428, May 1982.

[158] Kurt A. Johnson and N. W. Ashcroft. Corrections to density-functional theory band gaps. *Phys. Rev. B*, 58:15548–15556, Dec 1998.

[159] F Aryasetiawan and O Gunnarsson. The GW method. *Reports on Progress in Physics*, 61(3):237, mar 1998.

[160] R. Sakuma, C. Friedrich, T. Miyake, S. Blügel, and F. Aryasetiawan. GW calculations including spin-orbit coupling: Application to Hg chalcogenides. *Phys. Rev. B*, 84:085144, Aug 2011.

[161] A. Fleszar and W. Hanke. Electronic structure of II^B-VI semiconductors in the GW approximation. *Phys. Rev. B*, 71:045207, Jan 2005.

[162] Z. Zanolli, F. Fuchs, J. Furthmüller, U. von Barth, and F. Bechstedt. Model GW band structure of InAs and GaAs in the wurtzite phase. *Phys. Rev. B*, 75:245121, Jun 2007.

[163] F. J. Dyson. The s matrix in quantum electrodynamics. *Phys. Rev.*, 75:1736–1755, 1949.

[164] Lars Hedin. New method for calculating the one-particle green's function with application to the electron-gas problem. *Phys. Rev.*, 139:A796–A823, Aug 1965.

[165] E. E. Salpeter and H. A. Bethe. A relativistic equation for bound-state problems. *Phys. Rev.*, 84:1232–1242, 1951.

[166] G. Onida, L. Reining, and A. Rubio. Electronic excitations: density-functional versus many-body green's-function approaches. *Rev. Mod. Phys.*, 74:601, 2002.

[167] Mark S. Hybertsen and Steven G. Louie. Electron correlation in semiconductors and insulators: Band gaps and quasiparticle energies. *Phys. Rev. B*, 34:5390–5413, 1986.

[168] Michael Rohlfing and Steven G. Louie. Electron-hole excitations and optical spectra from first principles. *Phys. Rev. B*, 62:4927–4944, Aug 2000.

[169] Erich Runge and E. K. U. Gross. Density-functional theory for time-dependent systems. *Phys. Rev. Lett.*, 52:997–1000, Mar 1984.

[170] Jeffrey C. Grossman, Michael Rohlfing, Lubos Mitas, Steven G. Louie, and Marvin L. Cohen. High accuracy many-body calculational approaches for excitations in molecules. *Phys. Rev. Lett.*, 86:472–475, 2001.

[171] Andrew J. Williamson, Jeffrey C. Grossman, Randolph Q. Hood, Aaron Puzder, and Giulia Galli. Quantum monte carlo calculations of nanostructure optical gaps: Application to silicon quantum dots. *Phys. Rev. Lett.*, 89:196803, 2002.

[172] Vladimir I Anisimov, F Aryasetiawan, and A I Lichtenstein. First-principles calculations of the electronic structure and spectra of strongly correlated systems: the LDA+ U method. *J. Phys.: Condens. Matter*, 9(4):767, jan 1997.

[173] Fabien Tran and Peter Blaha. Accurate band gaps of semiconductors and insulators with a semilocal exchange-correlation potential. *Phys. Rev. Lett.*, 102:226401, Jun 2009.

[174] Yoon-Suk Kim, Martijn Marsman, Georg Kresse, Fabien Tran, and Peter Blaha. Towards efficient band structure and effective mass calculations for III − V direct band-gap semiconductors. *Phys. Rev. B*, 82:205212, Nov 2010.

[175] David Segev, Anderson Janotti, and Chris G. Van de Walle. Self-consistent band-gap corrections in density functional theory using modified pseudopotentials. *Phys. Rev. B*, 75:035201, Jan 2007.

[176] Jianwei Wang, Yong Zhang, and Lin-Wang Wang. Systematic approach for simultaneously correcting the band-gap and $p - d$ separation errors of common cation III − V or II − VI binaries in density functional theory calculations within a local density approximation. *Phys. Rev. B*, 92:045211, Jul 2015.

[177] Lin-Wang Wang and Alex Zunger. Local-density-derived semiempirical pseudopotentials. *Phys. Rev. B*, 51:17398–17416, Jun 1995.

[178] Huaxiang Fu and Alex Zunger. Local-density-derived semiempirical nonlocal pseudopotentials for InP with applications to large quantum dots. *Phys. Rev. B*, 55:1642–1653, Jan 1997.

[179] Jingbo Li and Lin-Wang Wang. Band-structure-corrected local density approximation study of semiconductor quantum dots and wires. *Phys. Rev. B*, 72:125325, Sep 2005.

[180] Stephan Lany, Hannes Raebiger, and Alex Zunger. Magnetic interactions of Cr−Cr and Co−Co impurity pairs in ZnO within a band-gap corrected density functional approach. *Phys. Rev. B*, 77:241201, Jun 2008.

[181] G. A. Baraff and M. Schlüter. Calculation of the total energy of charged point defects using the green's-function technique. *Phys. Rev. B*, 30:1853–1866, Aug 1984.

[182] O. Gunnarsson and K. Schönhammer. Density-functional treatment of an exactly solvable semiconductor model. *Phys. Rev. Lett.*, 56:1968–1971, May 1986.

[183] F. Nastos, B. Olejnik, K. Schwarz, and J. E. Sipe. Scissors implementation within length-gauge formulations of the frequency-dependent nonlinear optical response of semiconductors. *Phys. Rev. B*, 72:045223, Jul 2005.

[184] R. W. Godby, M. Schlüter, and L. J. Sham. Self-energy operators and exchange-correlation potentials in semiconductors. *Phys. Rev. B*, 37:10159–10175, Jun 1988.

[185] Menno Bokdam, Tobias Sander, Alessandro Stroppa, Silvia Picozzi, D. D. Sarma, Cesare Franchini, and Georg Kresse. Role of polar phonons in the photo excited state of metal halide perovskites. *Sci. Rep.*, 6(1):28618, 2016.

[186] L C Bannow, P Rosenow, P Springer, E W Fischer, J Hader, J V Moloney, R Tonner, and S W Koch. An *ab initio* based approach to optical properties of semiconductor heterostructures. *Modelling Simul. Mater. Sci. Eng.*, 25(6):065001, jun 2017.

[187] Marina R. Filip and Feliciano Giustino. *GW* quasiparticle band gap of the hybrid organic-inorganic perovskite $CH_3NH_3PbI_3$: Effect of spin-orbit interaction, semicore electrons, and self-consistency. *Phys. Rev. B*, 90:245145, Dec 2014.

[188] Ji ří Klimeš, Merzuk Kaltak, and Georg Kresse. Predictive *GW* calculations using plane waves and pseudopotentials. *Phys. Rev. B*, 90:075125, Aug 2014.

[189] M. Kozhevnikov, B. M. Ashkinadze, E. Cohen, and Arza Ron. Low-temperature electron mobility studied by cyclotron resonance in ultrapure GaAs crystals. *Phys. Rev. B*, 52:17165–17171, Dec 1995.

[190] Detlef Schneider, Detlef Rürup, Bernd Schönfelder, and Andreas Schlachetzki. Effective mass and energy-band parameters in InP by magnetophonon effect. *Zeitschrift für Physik B Cond. Matter*, 100(1):33–38, 1996.

[191] Y. Imanaka and N. Miura. Cyclotron resonance and strong phonon coupling in n-type ZnS at high magnetic fields up to 220 t. *Phys. Rev. B*, 50:14065–14068, Nov 1994.

[192] John C. Miklosz and Robert G. Wheeler. Exciton structure and magneto-optical effects in ZnS. *Phys. Rev.*, 153:913–923, Jan 1967.

[193] Y. Guldner, C. Rigaux, M. Grynberg, and A. Mycielski. Interband $\Gamma_6 \rightarrow \Gamma_8$ magnetoabsorption in HgTe. *Phys. Rev. B*, 8:3875–3883, Oct 1973.

[194] B. V. Shanabrook, O. J. Glembocki, D. A. Broido, and W. I. Wang. Luttinger parameters for gaas determined from the intersubband transitions in $GaAs/Al_xGa_{1-x}As$ multiple quantum wells. *Phys. Rev. B*, 39:3411–3414, Feb 1989.

[195] P. Rochon and E. Fortin. Photovoltaic effect and interband magneto-optical transitions in InP. *Phys. Rev. B*, 12:5803–5810, Dec 1975.

[196] P. Lawaetz. Valence-band parameters in cubic semiconductors. *Phys. Rev. B*, 4:3460–3467, Nov 1971.

[197] S. H. Groves, R. N. Brown, and C. R. Pidgeon. Interband magnetoreflection and band structure of HgTe. *Phys. Rev.*, 161:779–793, Sep 1967.

[198] P. YU and M. Cardona. *Fundamentals of Semiconductors: Physics and Materials Properties*. Graduate Texts in Physics. Springer Berlin Heidelberg, 2010.

[199] Huaxiang Fu and Alex Zunger. Excitons in InP quantum dots. *Phys. Rev. B*, 57:R15064–R15067, Jun 1998.

[200] Huaxiang Fu and Alex Zunger. InP quantum dots: Electronic structure, surface effects, and the redshifted emission. *Phys. Rev. B*, 56:1496–1508, Jul 1997.

[201] Tangi Aubert, Aleksandr A. Golovatenko, Margarita Samoli, Laurent Lermusiaux, Thomas Zinn, Benjamin Abécassis, Anna V. Rodina, and Zeger Hens. General expression for the size-dependent optical properties of quantum dots. *Nano Lett.*, 22(4):1778–1785, 2022.

[202] Eunseog Cho, Hyosook Jang, Junho Lee, and Eunjoo Jang. Modeling on the size dependent properties of InP quantum dots: a hybrid functional study. *Nanotechnology*, 24(21):215201, apr 2013.

[203] OI Mićić, HM Cheong, H Fu, A Zunger, JR Sprague, A Mascarenhas, and AJ Nozik. Size-dependent spectroscopy of InP quantum dots. *J. Phys. Chem. B*, 101(25):4904–4912, 1997.

[204] Shaukatali N. Inamdar, Pravin P. Ingole, and Santosh K. Haram. Determination of band structure parameters and the quasi-particle gap of CdSe quantum dots by cyclic voltammetry. *Chem. Phys. Chem.*, 9(17):2574–2579, 2008.

[205] Erol Kucur, Jürgen Riegler, Gerald A. Urban, and Thomas Nann. Determination of quantum confinement in CdSe nanocrystals by cyclic voltammetry. *J. Chem. Phys.*, 119(4):2333–2337, 07 2003.

[206] Claudia Querner, Peter Reiss, Said Sadki, Malgorzata Zagorska, and Adam Pron. Size and ligand effects on the electrochemical and spectroelectrochemical responses of CdSe nanocrystals. *Phys. Chem. Chem. Phys.*, 7:3204–3209, 2005.

[207] C. B. Murray, D. J. Norris, and M. G. Bawendi. Synthesis and characterization of nearly monodisperse CdE (E = sulfur, selenium, tellurium) semiconductor nanocrystallites. *J. Am. Chem. Soc.*, 115(19):8706–8715, 09 1993.

[208] Anastasia Karpulevich, Hanh Bui, Zhi Wang, Sören Hapke, Cristina Palencia Ramírez, Horst Weller, and Gabriel Bester. Dielectric response function for colloidal semiconductor quantum dots. *J. Chem. Phys.*, 151(22):224103, 12 2019.

[209] Robert W. Meulenberg, Jonathan R.I. Lee, Abraham Wolcott, Jin Z. Zhang, Louis J. Terminello, and Tony van Buuren. Determination of the exciton binding energy in CdSe quantum dots. *ACS Nano*, 3(2):325–330, 2009.

[210] W. William Yu, Lianhua Qu, Wenzhuo Guo, and Xiaogang Peng. Experimental determination of the extinction coefficient of CdTe, CdSe, and CdS nanocrystals. *Chem. Mater*, 15(14):2854–2860, 2003.

[211] Jacek Jasieniak, Lisa Smith, Joel van Embden, Paul Mulvaney, and Marco Califano. Re-examination of the size-dependent absorption properties of CdSe quantum dots. *J. Chem. Phys. C*, 113(45):19468–19474, 2009.

[212] Zhijun Ning, Matyas Molnár, Yun Chen, Peter Friberg, Liming Gan, Hans Ågren, and Ying Fu. Role of surface ligands in optical properties of colloidal CdSe/CdS quantum dots. *Phys. Chem. Chem. Phys.*, 13:5848–5854, 2011.

[213] Richard Karel Čapek, Iwan Moreels, Karel Lambert, David De Muynck, Qiang Zhao, André Van Tomme, Frank Vanhaecke, and Zeger Hens. Optical properties of zincblende cadmium selenide quantum dots. *J. Chem. Phys. C*, 114(14):6371–6376, 2010.

[214] Garry Rumbles, Donald C Selmarten, Randy J Ellingson, Jeffrey L Blackburn, Pingrong Yu, Barton B Smith, Olga I Mićić, and Arthur J Nozik. Anomalies in the linear absorption, transient absorption, photoluminescence and photoluminescence excitation spectroscopies of colloidal InP quantum dots. *J. Photochem. Photobiol. A*, 142(2):187–195, 2001.

[215] J. L. Blackburn, D. C. Selmarten, R. J. Ellingson, M. Jones, O. Micic, and A. J. Nozik. Electron and hole transfer from indium phosphide quantum dots. *J. Phys. Chem. B*, 109(7):2625–2631, 02 2005.

[216] L. Klemeyer, T.L.R. Gröne, C.A. Zito, O. Vasylieva, M. Gumus Akcaalan, S.Y. Harouna-Mayer, et al. Combining high x-ray energy photon-in photon-out spectroscopies and x-ray scattering to experimentally assess the emergence of

electronic- and atomic structure of ZnS nanorods. *ChemRxiv*, 2024. This content is a preprint and has not been peer-reviewed.

[217] R. Pässler, E. Griebl, H. Riepl, G. Lautner, S. Bauer, H. Preis, W. Gebhardt, B. Buda, D. J. As, D. Schikora, K. Lischka, K. Papagelis, and S. Ves. Temperature dependence of exciton peak energies in ZnS, ZnSe, and ZnTe epitaxial films. *J. App. Phys.*, 86(8):4403–4411, 10 1999.

[218] Cheng-Wei Lee, Meenakshi Singh, Adele C. Tamboli, and Vladan Stevanović. Transition metal impurities in silicon: computational search for a semiconductor qubit. *npj Com. Mater.*, 8(1):172, 2022.

[219] Benedikt Tissot, Péter Udvarhelyi, Adam Gali, and Guido Burkard. Strain engineering for transition-metal defects in SiC. *Phys. Rev. B*, 109:054111, Feb 2024.

[220] R. N. Bhargava, D. Gallagher, X. Hong, and A. Nurmikko. Optical properties of manganese-doped nanocrystals of ZnS. *Phys. Rev. Lett.*, 72:416–419, Jan 1994.

[221] Liwei Dai, Christian Strelow, Tobias Kipp, Alf Mews, Iris Benkenstein, Dirk Eifler, Thanh Huyen Vuong, Jabor Rabeah, James McGettrick, Rostyslav Lesyuk, and Christian Klinke. Colloidal manganese-doped ZnS nanoplatelets and their optical properties. *Chem. Mater.*, 33(1):275–284, 2021.

[222] Sameer Sapra, Ankita Prakash, Ajit Ghangrekar, N. Periasamy, and D. D. Sarma. Emission properties of manganese-doped ZnS nanocrystals. *J. Phys. Chem. B*, 109(5):1663–1668, 2005. PMID: 16851141.

[223] A. Fazzio, M. J. Caldas, and Alex Zunger. Many-electron multiplet effects in the spectra of 3d impurities in heteropolar semiconductors. *Phys. Rev. B*, 30:3430–3455, Sep 1984.

[224] John Stanley Griffith. *The theory of transition-metal ions*. Cambridge university press, 1961.

[225] Satoru Sugano. *Multiplets of transition-metal ions in crystals*. Elsevier, 2012.

[226] Henry Norris Russell and Frederick Albert Saunders. New regularities in the spectra of the alkaline earths. *Astrophysical Journal, vol. 61, p. 38*, 61:38, 1925.

[227] Enno Malguth, Axel Hoffmann, and Matthew R. Phillips. Fe in III–V and II–VI semiconductors. *physica status solidi (b)*, 245(3):455–480, 2008.

[228] R. Parrot, C. Naud, and F. Gendron. Structure of a $^4t_2$ level of Mn^{++} in tetrahedral symmetry, dynamical jahn-teller effect and selective intensity transfer. *Phys. Rev. B*, 13:3748–3763, May 1976.

[229] Russell J. Boyd. A quantum mechanical explanation for hund's multiplicity rule. *Nature*, 310(5977):480–481, 1984.

[230] Y Sajeev, M Sindelka, and N Moiseyev. Hund's multiplicity rule: From atoms to quantum dots. *J. Chem. Phys.*, 128(6), 2008.

[231] G.F. Koster. *Properties of the Thirty-two Point Groups*. M.I.T. Press research monographs. M.I.T. Press, 1963.

[232] Lukas Muechler, Danis I Badrtdinov, Alexander Hampel, Jennifer Cano, Malte Rösner, and Cyrus E Dreyer. Quantum embedding methods for correlated excited states of point defects: Case studies and challenges. *Phys. Rev. B*, 105(23):235104, 2022.

[233] Christoph R Jacob and Markus Reiher. Spin in density-functional theory. *Int. J. Quant. Chem.*, 112(23):3661–3684, 2012.

[234] George H. Booth, Andreas Grüneis, Georg Kresse, and Ali Alavi. Towards an exact description of electronic wavefunctions in real solids. *Nature*, 493(7432):365–370, 2013.

[235] Y. Ma, M. Rohlfing, and A. Gali. Excited states of the negatively charged nitrogen-vacancy color center in diamond. *Phys. Rev. B*, 81(4):041204(R), 2010.

[236] S. K. Choi, M. Jain, and S. G. Louie. Mechanism for optical initialization of spin in NV^- center in diamond. *Phys. Rev. B*, 86(4):041202(R), 2012.

[237] Christoph Freysoldt, Blazej Grabowski, Tilmann Hickel, Jörg Neugebauer, Georg Kresse, Anderson Janotti, and Chris G. Van de Walle. First-principles calculations for point defects in solids. *Rev. Mod. Phys.*, 86:253–305, Mar 2014.

[238] X.Gonze, J.-M.Beuken, F.Detraux, M.Fuchs, G.-M.Rignanese, L.Sindic, M.Verstraete, G.Zerah, F.Jollet, M.Torrent, A.Roy, M.Mikami, Ph.Ghosez, J.-Y.Raty, and D.C.Allane. First-principles computation of material properties: the ABINIT software project. *Com. Mater. Science*, 2002.

[239] Anastasia Karpulevich. *Calculation of the electronic and optical properties of colloidal nanostructures using the comprehensive method based on atomic effective pseudopotentials*. PhD thesis, Staats-und Universitätsbibliothek Hamburg Carl von Ossietzky, 2020.

[240] Thi Hanh Bui. *The excitonic fine structure of colloidal nanocrystals*. PhD thesis, Staats-und Universitätsbibliothek Hamburg Carl von Ossietzky, 2020.

[241] Priya Mahadevan and Alex Zunger. Ferromagnetism in Mn-doped GaAs due to substitutional-interstitial complexes. *Phys. Rev. B*, 68(7):075202, 2003.

[242] Priya Mahadevan and Alex Zunger. First-principles investigation of the assumptions underlying model-hamiltonian approaches to ferromagnetism of 3d impurities in III-V semiconductors. *Phys. Rev. B*, 69(11):115211, 2004.

Acknowledgements

First and foremost, I would like to express my sincere gratitude to my supervisor, Prof. Dr. Gabriel Bester, for providing me with the opportunity to pursue challenging and rewarding research projects. His constant guidance and advice throughout my PhD studies have been invaluable.

I would like to extend my special thanks to several colleagues for their invaluable collaboration on specific projects: Dr. Torben Steenbock and Tobias Dittmann for the CdSe Quantum Dots fine-structure project; Dr. Torben Steenbock for the Raman project; Dr. Hanh Bui for the band gap correction project; Anne Nadine for the alloyed dots fine structure project; Dr. Pablo and Dr. Peng Han for the frozen-phonon method project; Prof. Dr. Alf Mews and Hans Werner for the dot-rod nanostructure project; Walter Pfäffle for the defect atomic effective pseudopotential project; Geoffery Pirard for the 2D nanoplatelet project.

I am deeply grateful to Dr. Torben Steenbock, Dr. Marta Prada, Dr. Abdezzrak Torche, Dr. Hanh Bui, Dr. Anastasia Karpulevich, Geoffery Pirard, Carl Emil Morch Nielsen, Franz Fisher, Anne Nadine, Tobias Dittmann, Dr. Yasser Saleem, Dr. Sumanti Patra, Miguel Morals, Shubham Agarwal, Jens Hühnert, Walter Pfäffle, Lawrence Rybakowski, Marie Meins, and Angelina Dell for their support during my PhD journey. Their help, both moral and practical, has been instrumental in my success.

My gratitude also extends to Kshitiz Mahat for his Master's Thesis, and Wendlein Lopez, and Vicktor Kemme for their Bachelor's thesis work with me.

I would like to express my appreciation to all my friends in Hamburg for their companionship and support throughout these years.
Finally, my deepest thanks go to my parents and brother for their unwavering love and support, no matter the distance.

To improve the grammar and wording in sections of this thesis, the author acknowledges the use of ChatGPT, Gemini, and Grammarly as proofreading tools. However, no analysis or conclusions for the scientific work presented in this thesis were generated

using these artificial intelligence tools.

Declaration

I hereby declare and affirm that this doctoral dissertation is my own work and that I have not used any aids and sources other than those indicated.

If electronic resources based on generative artificial intelligence (gAI) were used in the course of writing this dissertation, I confirm that my own work was the main and value-adding contribution and that complete documentation of all resources used is available in accordance with good scientific practice. I am responsible for any erroneous or distorted content, incorrect references, violations of data protection and copyright law, or plagiarism that may have been generated by the gAI.

Date	Surender Kumar